Prediction of Flow and Heat Transfer Inside Turbine Blades Using EARSM, $k-\varepsilon$ and $k-\omega$ Turbulence Models

June, 1999

Jonas Bredberg

bredberg@tfd.chalmers.se

Göteborg, July 1999

PREDICTION OF FLOW AND HEAT TRANSFER INSIDE TURBINE BLADES USING EARSM, $k-\varepsilon$ AND $k-\omega$ TURBULENCE MODELS

Jonas Bredberg

bredberg@tfd.chalmers.se
http://www.tfd.chalmers.se/~bredberg
Department of Thermo and Fluid Dynamics
Chalmers University of Technology
S-412 96 Gothenburg
Sweden

Abstract

Gas turbine blades must be cooled internally to achieve the efficiency demanded by the gas turbine industry. The blades are cooled with pressurized air, flowing in intricate channels on the inside of turbine blades. This thesis focuses on predicting the flowfield and heat transfer in these channels, using a full Naiver-Stokes solver with several different turbulence models.

The turbulence models evaluated are: the two-layer $k-\varepsilon$ of Chen-Patel, two $k-\omega$ models (Abid *et al.* and Peng *et al.*) and the Gatski-Speziale EARSM using two different pressure-strain models. The heat transfer model used is a turbulent Prandtl number model.

The test cases included are: 2D and 3D rotating channels, 2D and 3D ribbed channels, and 3D rotating ribbed channels. The flowfield was generally accurately predicted, although the heat transfer predictions deviate from the experimental data.

The thesis gives a thorough discussion of the rotationally induced forces – Coriolis and centrifugal – including their effects on the Navier-Stokes equation and turbulence. The behavior of the evaluated turbulence models caused by these forces is discussed.

Keywords: Coriolis, centrifugal, Navier-Stokes, finite volume, vorticity, turbulence model, explicit algebraic Reynolds stress model, non-linear, $k-\varepsilon$, $k-\omega$, internal cooling, turbine blade, rotating, ribbed channel

Contents

Acknowledgments

This work was done primarily at the Department of Thermo and Fluid Dynamics at Chalmers University of Technology, Gothenburg, Sweden. Part of the research was also done at the Department of Mechanical Engineering at the University of Manchester Institute of Science & Technology, Manchester, UK. The project was funded by GTC, a national Gas Turbine Center sponsored by Volvo Aero Corporation, ABB STAL and STEM, STatens EnergiMyndighet.

I would like to express my greatest precautions toward Prof. L. Davidson for all his advice, guidance and support to this time. I hope it will continue. You have been a most valuable inspiration in this work. I would also like to thank Dr. H. Iacovides for a very fruitful visit at UMIST, where most of the later computations were made and several of the experimental data were gathered. My thoughts go to him and his colleagues who made my stay so enjoyable.

Finally I would like to thank my colleagues at the Department of Thermo and Fluid Dynamics who all create a pleasant working environment that enables us to work efficiently.

Preface

This thesis is based on the results presented in the following papers:

- Jonas Bredberg, Lars Davidson. "Case 7.2: Two-dimensional flow and heat transfer over a smooth wall roughened with squared ribs", Proceedings from 7th ERCOFTAC/IAHR workshop on refined turbulence modeling, UMIST, Manchester, UK, May 28/29th, 1998

- Jonas Bredberg, Lars Davidson. "Prediction of flow and heat transfer in a stationary 2-D rib roughened passage using low-Re turbulent models", Proceedings of the 3:rd European Conference on Turbomachinery, London, UK, March 2/5th, 1999

Nomenclature

a_{ij}	Anisotropy tensor $[-]$
c_p	Specific heat $[J/kgK]$
D_h	Hydraulic diameter $[m]$
h	Channel half-height $[m]$
H	Channel height $[m]$
k	Turbulent kinetic energy $[m^2/s^2]$
Nu	Nusselt number $[-]$
p	Static pressure $[N/m^2]$
Pr	Prandtl number $[-]$
q_i	Heat flux $[W/m^2]$
Re	Reynolds number $[-]$
Ro	Rotational number $[-]$
s_{ij}, S_{ij}, s'_{ij}	Strain-rate tensor $[s^{-1}]$
t	Time $[s]$
u_i, U_i, u'_i	Velocity $[m/s]$
$\overline{u'_i u'_j}$	Reynolds stresses $[m^2/s^2]$
δ_{ij}	Kronecker's delta function $[-]$
ε	Dissipation rate $[m^2/s^3]$
ϵ_{ijk}	Levi-Cevita's permutation function $[-]$
θ, Θ	Temperature $[K]$
ν	Kinematic viscosity $[m^2/s]$
μ	Dynamic viscosity $[Ns/m^2]$
ρ	Density $[kg/m^3]$
ω	Specific dissipation rate $[s^{-1}]$
ω_i	Vorticity $[s^{-1}]$
Ω_i	Angular rotation velocity $[s^{-1}]$
Ω_{ij}	Rotation tensor $[s^{-1}]$

Subscript:	b	Bulk value
	D	Value based on the hydraulic diameter
	h	Value based on the channel half-height
	H	Value based on the channel height
	m	Mean value
	t	Turbulent part
	tot	Total value
	w	Wall value
Superscript:	*	Non-dimensionalized value

The notation for the decomposable variables (u_i, s_{ij}) is $\phi = \Phi + \phi'$, where $\Phi = \overline{\phi}$ is the time-averaged mean value and ϕ' is the fluctuating value.

1 Introduction

1.1 The Need for Cooling

An increase in working temperature is a suitable solution, for increasing the performance of gas turbine engines. It can be found from laws of physics that an increase of the turbine entry temperature (TET) would rise the net efficiency of the gas turbine. However, an increase in temperature will increase the demands on the structures in the engine. High grade materials, as are found in e.g. the turbine blades, can withstand high loads for infinite times at room temperature. At elevated temperature, however, the materials become weaker and begin to creep, which limits the time span for which the turbine blades can be used. There are generally two different approaches to the problem of increasing the TET, and still achieving a sufficiently long endurance of stressed parts. The materials are either changed to even higher strength materials, or cooling air is used to reduce the working temperature of the structures. While both these solutions are normally employed, only the cooling idea will be addressed here. Fig. 1.1 shows the increase in TET caused by material development, and cooling.

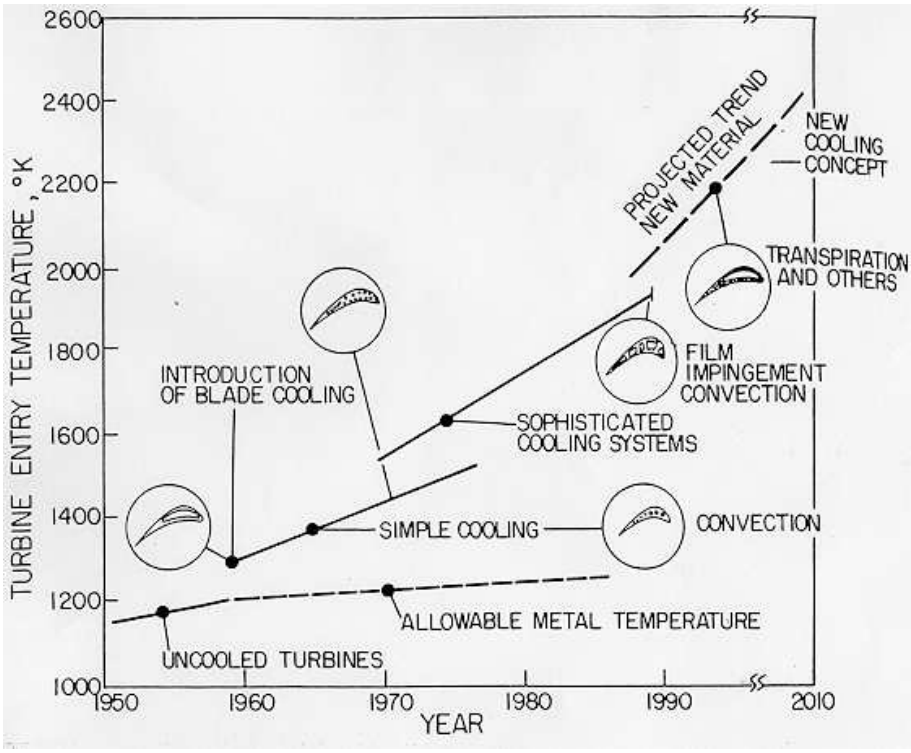

Figure 1.1: Progress in TET Over Recent Years, Lakshminarayana, [32]

There are several areas in a gas turbine which will need cooling owing to the high temperatures encountered. The combuster where the air and fuel is mixed and ignited will naturally have a very high temperature. This mixed air/fuel gas then flows through the turbine before exiting at the back through the nozzle. These parts also work at elevated temperatures of course, even if they are not as high as in the combuster. The focus of this thesis is the cooling of the turbine blade.

1.2 The Gas Turbine

A gas turbine – contrary to the common belief – is a rather simple engine. It consists merely of a rotating structure and some container in which air and fuel can be mixed and ignited. The purpose of the rotating structure is to increase the mass flow of air into this container. The thrust is developed by the increase in the velocity of the air. Still there is more to this in the design of a modern gas turbine engine. The five main parts of the gas turbine are, from the front: the inlet, the compressor, the combuster, the turbine, and the nozzle. The compressor is a set of blades and forms a part of the rotating structure, which increases the pressure of the incoming air. This will also raise the temperature, which however is not the main purpose of the compressor. The highly pressurized air enters the combuster, where it is mixed with the fuel, and ignited. The combuster does not, as the IC engine, have a repeating ignition cycle since, when the engine is lit up, the mixture will self-ignite in the hot combuster. From the combuster, the hot gases are led through the turbine before they exit through the nozzle in the rear. The turbine is connected to the compressor through a center shaft in the engine and has as its sole purpose to drive the compressor. The thrust is developed through the increase in velocity of the air. A main deficiency of the gas turbine is its low ratio of net power to needed power. This makes the engine prone to high efficient compressor and turbine, otherwise the compressor would consume more power than the turbine can produce, and hence the engine would be a no-go machine.

1.3 The Turbine - Cooling Techniques

The turbine stage is composed of an inlet guide vane followed by a turbine blade. The stationary vane and the rotating blade are matched together and are known as a stage. A gas turbine has normally several turbine stages. Due to the high working temperatures of the turbine, it employs several different cooling techniques, both for the vane and the blade. In most cases the cooling media is high-pressure air which is drawn from the compressor through ducts in the center of the engine. This air is then led up, through the inside of the blades and vanes in intricate ducts. There will thus be two distinct gas flows around the turbine, the main gas flow with hot gases from the combuster on the outside and the secondary air flow with cooling air from the compressor on the inside. There are two different cooling techniques: one in which the cooling media is in contact with the hot gases on the outside of the blade and another in which the cooling media is employed only on the inside to cool the blade material. These techniques are known as external and internal cooling. These are then subdivided into several sub-groups such as:

- Internal cooling:
  - Convection cooling
  - Impingement cooling
  - Internally air-cooled thermal barrier
- External cooling
  - Local film cooling
  - Full-coverage film cooling
  - Transpiration cooling

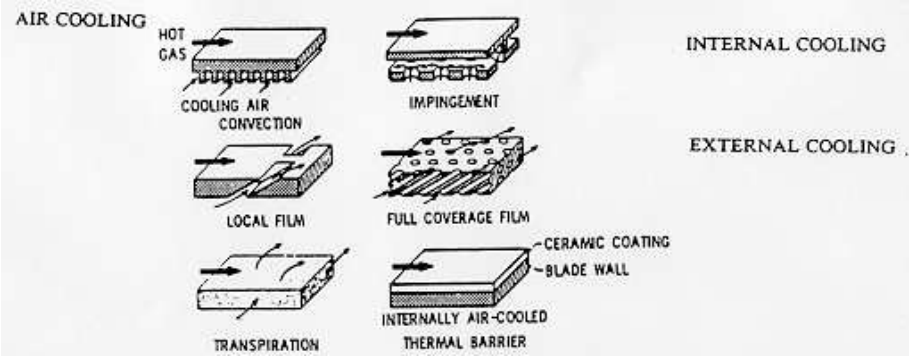

Figure 1.2: Blade and Vane Cooling Techniques, Lakshminarayana [32]

illustrated in Fig. 1.2.
This thesis addresses only the internal cooling of the turbine blade.

1.4 The Inside of the Turbine Blade

Of the above three principles for internal cooling, two are generally employed, convective cooling and impingement cooling. The structure of a typical turbine blade consists mainly of three distinct areas: the front section with impingement cooling, the middle section consisting of serpentine ducts with turbulators, and the rear section of a matrix section or pin-fin system leading to the outlet at the trailing edge of the blade, see Fig. 1.3

The front section is fed by air through the first serpentine duct or directly through a separate inlet in the root. The air is diverted to the front face and is injected onto the surface (impinging) thereby effectively cooling the surface. The air is led out through small slots in the blade, which results in film cooling on the outside of the blade.

The middle section consists of three or more serpentine ducts, connected by 180° bends. To enhance the convective cooling, ribs, or turbulators traverse to the flow are generally constructed in the ducts. Surface enlargers are sometimes also included, as fins extending out from the surface. The air can either be led out through the back end or via slots in the blade to film cooling.

The back section has a number of surface enlargers, pins or ribs, generally employed as a matrix, through which the air is led. The air can enter the back section, either from the serpentine section or via its own entrance in the root. When the air has passed the matrix, it is let out through a slot in the rear of the blade.

The below treats only the middle section with its serpentine ducts. Questions addressed are: how the flowfield will develop and what the heat transfer level will be. Predictions are compared with experiments, which are regrettably not very common owing to the severe complexity of the flow, and some conclusions are made regarding the models used and their validality in these flow conditions.

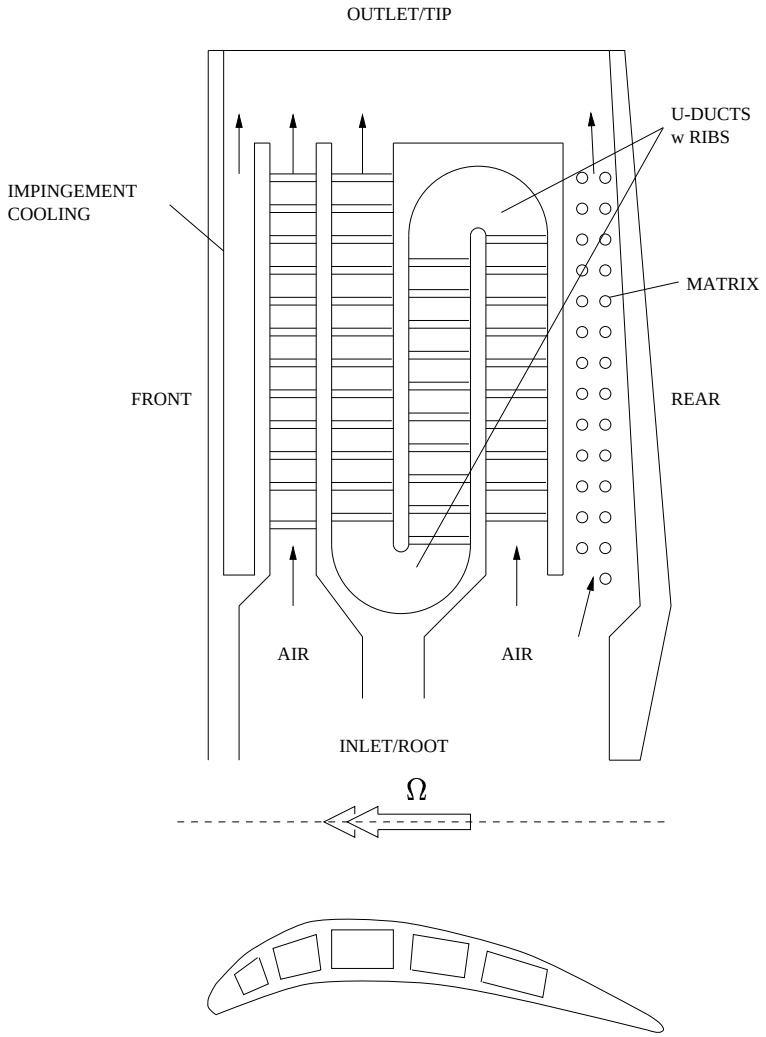

Figure 1.3: Structure of a Turbine Blade

2 Fluid Dynamics Inside The Turbine Blades

The flow inside the turbine blades is affected by the presence of numerous physical forces. These include the rotationally induced forces, curvature forces and buoyant forces, in addition to flow separation, strong acceleration and secondary motion caused by the structure itself. Together, these form a very complex, three-dimensional flowfield which is a challenge for any numerical method. However, before consideration is given to a reasonable numerical method, the physics must be understood.

2.1 Suction-Leading, Pressure-Trailing Side

Papers dealing with cooling of turbomachinery, and especially the inside of turbine blades use several terms which will be used here. There may thus be some benefit in explaining these terms more strictly. The first is the **pressure** and **suction** side, closely connected to the outside of the turbine blade. A turbine blade, like an airfoil, is surrounded by a gas on both sides. As in the case of the airfoil the turbine blades are curved, and posses a convex and concave side. The flow accelerates more strongly on the convex side and, due to the nature of gases, this gives a decrease in pressure. It is from this fact that the terms suction and pressure sides derive. On the low-pressure side, the convex side, the flow tends to suck the blade against it while, on the high-pressure side, the concave side, the gas pushes the blade away. The same terminology is also used for the airfoil, where the upper surface is known as the suction side and the lower the pressure side.

Closely connected to the pressure/suction side, are the **trailing** and **leading** sides. Whereas the pressure and suction sides arise from from the outside flow – the main gas flow – the leading and trailing sides are connected to the rotational direction of the blade. However, there is a strong connection between them. Since the blade is unsymmetric, through its convex and concave sides, the predominant rotational direction is set at the design state. Thus the rotation direction is strongly connected to the outside geometry of the blade. It was said above that the suction side draws the blade towards it, thus leading the blade in the rotational direction, while the pressure side pushes the blade in the same direction, thus trailing the blade. Herein lies the connection, i.e. the leading side will always be the same as the suction side, and the trailing will always be the same as the pressure side, for a turbine blade.

2.2 Stable/Unstable Boundary Layers

A stable flow is a flow which has a decreased level of turbulent kinetic energy and lower Reynolds shear stresses, while an unstable flow has increased levels of turbulent kinetic energy and higher Reynolds shear stresses. This may be understood through the knowledge that unstable conditions promote a transition from laminar to turbulent flow. Thus a stable side is a side along which re-laminarization is promoted, and an unstable side adds turbulent kinetic energy to the flow. The effects on the boundary layer from a system rotation and curvature will be discussed below. [1]

The origin of the stabilizing/unstabilizing process, can be associated with the balancing pressure gradient normal to the wall. If there exists a positive pressure force normal to the wall, a perturbated fluid element will have the tendency to move away from the wall.

[1] The curvature effect is included since there is a strong connection between this and the rotational effect.

This boundary layer will thus have an unstabilizing effect on the flow. On the other hand, if there exists a negative pressure force normal to the wall, a perturbated fluid element will be forced in position in a stabilizing way. This pressure force originates either from the centrifugal force (curvature) or the Coriolis force (rotation), or both as in the case of a U-bend. In the case of a positive rotation (anti-clock wise in Fig. 2.1) the Coriolis acceleration will be directed upwards, and will thus have a destabilizing effect. The same is true for the negative curvature, where the centrifugal acceleration produces a positive pressure force. Reversing the order produces a negative pressure force and a stabilizing boundary layer. The four states are shown in Fig. 2.1

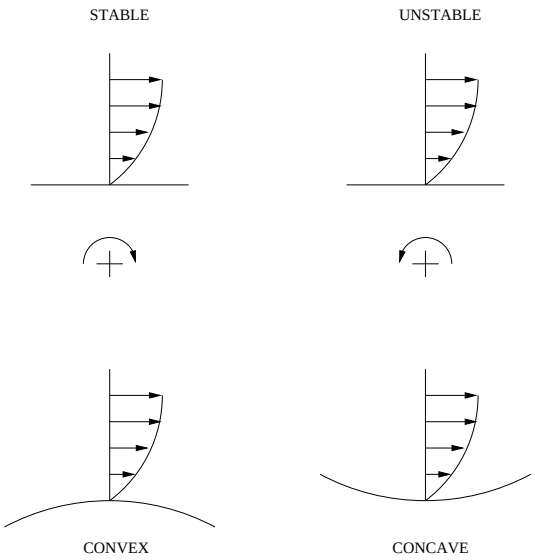

Figure 2.1: Stability of Rotating and Curvature Flows

While the pressure and suction sides above were connected to the structure, the stabilized and unstabilized sides are connected to the flowfield and can thus not be known a priori. However, with a knowledge of the flow and rotating direction, this can also be established. Fixing the rotating direction, which is done through the geometry of the blade, the stable and unstable sides are dependent only on whether the flow is moving from the center, **outward**, or to the center, **inward**. Fig. 2.2 below depicts a simplified internal structure of a turbine blade, with an indication of the leading/trailing surfaces. Comparing this with Fig. 2.1 for stabilizing/unstabilizing sides in the case of rotation, the following applies:

Inward flow	Leading surface	Unstabilized side
	Trailing surface	Stabilized side
Outward flow	Leading surface	Stabilized side
	Trailing surface	Unstabilized side

2.3 Rotationally Induced Forces

A rotating structure gives rise to two additional forces, the centrifugal force and the Coriolis force. These modify the governing equations through their extra acceleration on the fluid elements. The centrifugal term acts as a pressure driven force, modifying the pressure gradient of the flow and thus affecting the mass flow. Since the centrifugal force

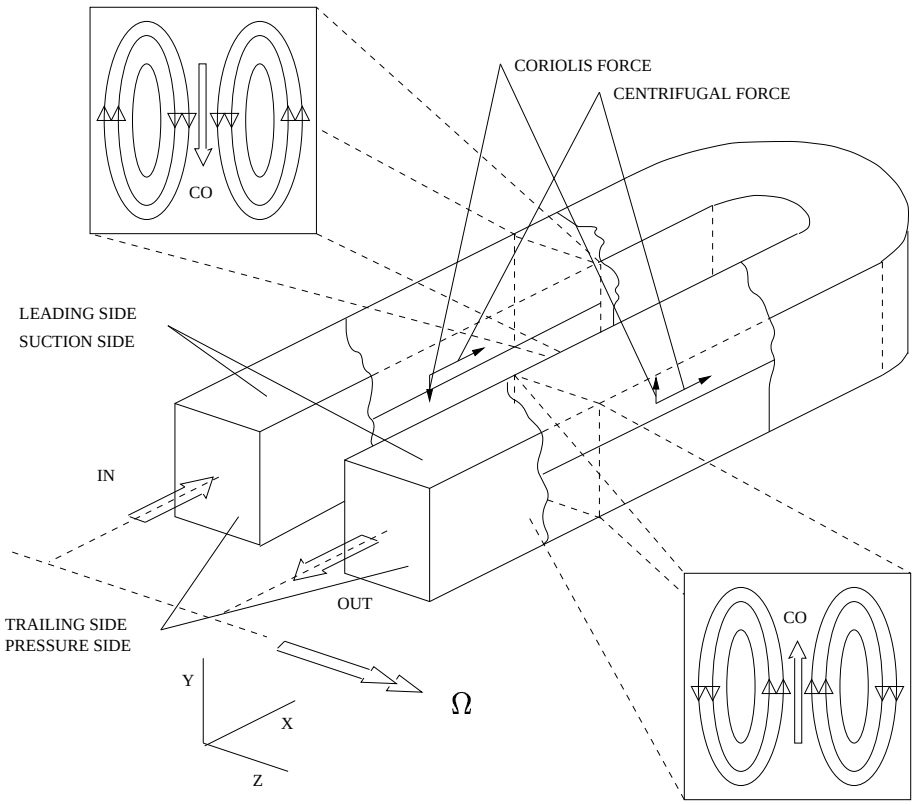

Figure 2.2: Secondary Flow, Caused by Rotation

is dependent on the density, higher density fluid gives a stronger centrifugal force. In a varying density flowfield, this force induces secondary flows in the cross sectional plane – normal to the streamwise direction – although their magnitudes are small. The centrifugal force can also be seen as a gravitational force with a rotating force field, dependent on the distance to the rotating center.

The Coriolis force is a term that depends on both the velocity and the rotational velocity. Due to its origin, the Coriolis force varies in the plane normal to the main flow because the force is zero where the velocity is zero, i.e. close to the walls. This force gives rise to a secondary flow pattern in the cross sectional plane, which is visible in Fig. 2.2

2.4 Curvature Effects

As discussed above, the curvature effect is similar to rotationally induced forces, although in this case there will be no modification to the governing equation. A curved duct produces a centrifugal force normal to the flow which is balanced by a pressure force. This gives rise to either the stabilizing or unstabilizing effect as discussed above and modifies the turbulence level of the flow. In a rotating U-bend, there is both the rotating-induced and the curvature-induced modification to the turbulence level, which can produce a severely complex flowfield.

2.5 Temperature Induced Forces

Inside the duct, there is a complexity of different physical forces that give rise to a temperature variation and thus a buoyant term. There is both a temperature variance in the

plane normal to the flow and along the streamwise direction.

The variation in the streamwise direction is caused by the continuous heating of the coolant. This decreases the density and produce a driving force, similar to that in a natural convection case. This effect is normally denoted as the bulk buoyant term.

In the plane normal to the flow, there are three distinct features which produce temperature gradients. The first is according to work load. Secondly the blades are not optimized according to heat load, which creates a difference in blade temperature. Both these effects give an uneven wall temperature inside the duct. The third feature has to do with the fact that the coolant is heated only at the walls, and thus the core is much colder than the fluid close to the walls. This also produces temperature gradients in the plane normal to the flow. These three effects are commonly denoted as the local buoyant term.

The temperature-induced forces are neglected in this thesis, although the temperature field is predicted, with the associate heat transfer level being the major focus.

2.6 Secondary Flows

Secondary flow is a generic term which denotes flow that lies in the plane normal to the main flow, the cross sectional plane. Generally, the secondary flow velocities are small compared with the main flow, except perhaps close to a solid wall where they may be of equal magnitude.

There are two different types of secondary flows, those of the first kind and those of the second kind. Secondary flows of the first kind, appear owing to either curvature or rotational effects, while those of the second kind are caused by gradients of the Reynolds stresses. It is this latter mechanics that produces secondary flows, in a straight duct, around the corners. Secondary flows of the first kind are produced by a force in the plane normal to the streamwise, produced either by a centrifugal or Coriolis force. The Coriolis force induced secondary flow originates from the variation in the streamwise velocity. The Coriolis force is a product of velocity and the rotating velocity. Thus, where the velocity is small, the Coriolis force is also small. Since the Coriolis force is strongest in the core, due to the higher velocity, the fluid will flow towards the wall in the direction of the Coriolis force, and then return along the wall where the Coriolis force is weak, due to the no-slip condition at the walls. This produces two equal secondary flow patterns, mirrored at the symmetry line, in the plane normal to the rotation vector, as can be observed in Fig. 2.2

2.7 Separation

Inside the serpentine ducts, see Fig. 1.3, ribs are employed to enhance the heat transfer. The ribs, which are positioned normal to the flow at the opposing walls, break up the flow and generate turbulence. This increase in turbulence level increases the heat transfer rate as well. There is a downside however; the ribs also increase the pressure drop in the duct, and thus the driving force needs to be higher.

As the flow encounters the ribs, it diverts and makes a small re-circulation zone upstream of the rib. Around the upstream upper corner, the flow separates and yields another small re-circulation zone before it re-attaches again on the rib top. At the upper downstream corner of the rib, the flow separates again, this time making a larger re-circulation region until the flow re-attaches again somewhere between the ribs[2]. This

[2]Depending on the configuration of the ribs and the Reynolds number, it may happen that the flow

flowfield, with repeated separations and re-attachments, will indeed increase the heat transfer, which could become several times as high as for a smooth channel. This increase in heat transfer is thus the gain paid by the increase in driving force.

does not re-attach again.

3 The Navier-Stokes Equation

After having discussed the physics in a rather general manner above, a discussion of its implementation in the governing equation is found below. The main governing equation for fluid dynamics is the Navier-Stokes equation, which is based on a number of fundamental physical principals with the addition of some sound physical reasoning.
The Navier-Stokes constitutes of two simple principles, that of the conservation of mass and that of the conservation of momentum.

3.1 Continuity Equation

The continuity equation is based on the assumption of mass conservation, i.e. that mass can neither be created nor destroyed. This is essentially correct for non-nuclear cases, which are not addressed here. The differential continuity equation in tensorial form is, see e.g. Panton [41]:

$$\frac{\partial \rho}{\partial t} + \frac{\partial \rho u_i}{\partial x_i} = 0 \tag{3.1}$$

3.2 Momentum Equation

The momentum equation or linear momentum equation, to distinguish it from the angular momentum equation, is based on Newton's second law:

$$\frac{d\mathbf{m}u}{dt} = \mathbf{F} \tag{3.2}$$

This formulation is a more general description than the more common equation, $m\mathbf{a} = \mathbf{F}$. Dividing with volume and re-casting the substantial derivate of the velocity gives the differential tensorial momentum equation:

$$\frac{\partial \rho u_i}{\partial t} + \frac{\partial \rho u_j u_i}{\partial x_j} = \rho f_i^{body} + \frac{\partial f_i^{surf}}{\partial x_j} \tag{3.3}$$

The force, $\mathbf{F}$, has been split into; the body forces, f_i^{body}, and the surface forces, f_i^{surf}, which both need some additional treatment. Note that these forces have been divided by mass, $m = \rho \Delta x \Delta y \Delta z$, i.e. $f_i = \mathbf{F}/m$

3.3 Body Force

The standard body force is the gravitational force, which is an effect of the earth's gravitational field. This force field is directed towards the center of the earth and attracts any mass element within its reach by a force equivalent to:

$$f_i^{grav} = g_i \tag{3.4}$$

Formally, this force depends on the distance from the mass element, i.e. the center of the earth. However, the variation is very slight and can normally be neglected.

Apart from this force, the magnetic and electric body forces can be neglected in fluid mechanics, and thus the gravitational force is the only proper body force which is encountered. However, as will be seen later, the rotationally induced accelerations can contribute to the body forces. These forces, which add extra acceleration terms to the Navier-Stokes equation, can be considered as body force modifiers, with a magnitude equal to the acceleration multiplied by the mass of the fluid element.

3.4 Surface Forces

By adopting the Stokes postulation for a viscous fluid, the surface forces can be written as the sum of pressure and viscous stresses. These are normally added together into a stress tensor, T_{ij}. The surface force is then the normal vectors of this stress tensor, according to:

$$f_i^{surf} = n_j T_{ij} \tag{3.5}$$

where the stress tensor is:

$$T_{ij} = -p_t \delta_{ij} + \tau_{ij} \tag{3.6}$$

The viscous stress tensor (τ_{ij}) is decomposed into a volumetric dilatation term, and a strain-rate dependent term, see e.g. Schlichting, [50]:

$$\tau_{ij} = \lambda \frac{\partial u_k}{\partial x_k} \delta_{ij} + 2\mu s_{ij} \tag{3.7}$$

With the Stokes relation between the bulk viscosity, λ, and the molecular viscosity, μ, i.e. $\lambda = -2\mu/3$ [3], the surface forces can be written as:

$$f_i^{surf} = n_j \left(-p\delta_{ij} - \frac{2}{3}\mu \frac{\partial u_k}{\partial x_k} \delta_{ij} + 2\mu s_{ij} \right) \tag{3.8}$$

In an incompressible case, the middle term can be dropped due to the continuity equation[4].

3.5 Navier-Stokes Equation

The Navier-Stokes equation is found by adding the body forces, Eq. 3.4, and surface forces, Eq. 3.8, to the momentum equation above, Eq. 3.3:

$$\frac{\partial \rho u_i}{\partial t} + \frac{\partial \rho u_j u_i}{\partial x_j} = \rho g_i - \frac{\partial p}{\partial x_j} \delta_{ij} + \frac{\partial}{\partial x_j} \left(-\frac{2}{3}\mu \frac{\partial u_k}{\partial x_k} \delta_{ij} + 2\mu s_{ij} \right) \tag{3.9}$$

The above equation is valid for incompressible and compressible flows, with variating properties (viscosity), i.e. a general purpose Navier-Stokes equation. The pressure term, $\partial p/\partial x_j \delta_{ij}$, can – by the use of the Kronecker delta, δ_{ij} – be rewritten as: $\partial p/\partial x_i$ which, will be used hereafter.

3.6 Temperature Equation

The continuity and momentum equation governs the flow for isothermal conditions. However, when heat transfer and differential temperatures are involved, the energy equation must be used to form a rigid set of equations. The energy equation can be changed into a temperature, θ, dependent relation, which under the assumption of incompressible flow with constant properties is:

$$\rho c_p \frac{\partial \theta}{\partial t} + \rho c_p \frac{\partial u_i \theta}{\partial x_i} = -\frac{\partial q_i}{\partial x_i} \tag{3.10}$$

[3] This relation is rather controversial but generally accepted. There is little physics behind this relation.

[4] This can be done because $\partial u_k/\partial x_k \equiv 0$.

The heat flux can be rewritten by the use of the Fourier's law of conduction: *the heat flux due to conduction in a point is proportional to the temperature gradient from that point*:

$$q_i = -k\frac{\partial \theta}{\partial x_i} \tag{3.11}$$

The proportional constant, k, is denoted *the thermal conductivity*. Using this relation for the heat-flux and making a rearrangement gives the temperature equation:

$$\frac{\partial \theta}{\partial t} + \frac{\partial u_i \theta}{\partial x_i} = \frac{\partial}{\partial x_i}\left(\frac{\nu}{Pr}\frac{\partial \theta}{\partial x_i}\right) \tag{3.12}$$

where $Pr = c_p \mu / k$ is the Prandtl number.

4 The Rotationally Modified Navier-Stokes Equation

4.1 Rotating Coordinate Systems

In an analysis of fluids for a rotating structure such as are found in turbomachinery, the use of an intermediate frame is not only advantageous – it is almost necessary. Consider a region of fluid in Fig. 4.1 with P as the point of interest. If an Eulerian grid were fixed in the inertial coordinate system (Newtonian frame, N), the Navier-Stokes equation would be valid. P (in the intermediate frame, I) would move in and out of the grid however, and this would make the analysis difficult. If the grid is shifted to the region outlined in Fig. 4.1, the coordinate system would not be an inertial coordinate system, and thus the Navier-Stokes equations are no longer valid. This complication is solved by adopting a non-inertial coordinate system and adding terms in the Navier-Stokes equations to compensate for this. Consider once again point P in Fig. 4.1. The position of point P

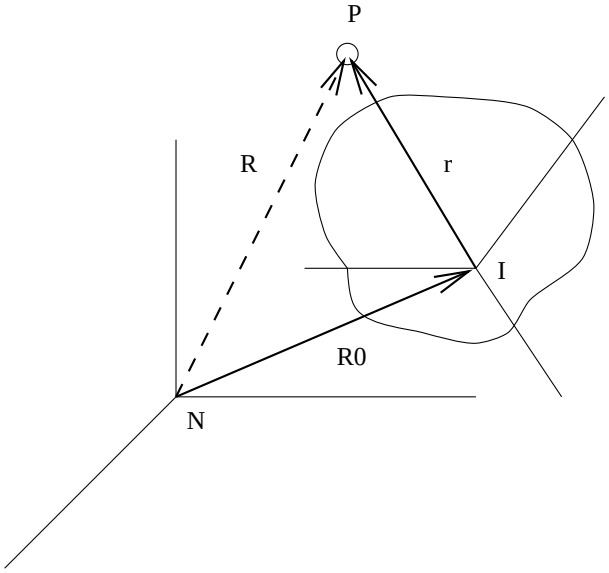

Figure 4.1: Rotating Coordinate System

relative to the Newtonian frame, N, is:

$$\mathbf{R} = \mathbf{r} + \mathbf{R}_0 \tag{4.1}$$

where $\mathbf{R}_0$ is the position of the origin of the intermediate frame relative to the Newtonian frame and $\mathbf{r}$ is the position of point P in the intermediate frame. If the positional vector of the N-frame is derived with time, the velocity vector in the N-frame is found:

$$\mathbf{V} = \frac{{}^N d\mathbf{R}}{dt} = \frac{{}^N d\mathbf{r}}{dt} + \frac{{}^N d\mathbf{R}_0}{dt} \tag{4.2}$$

Here, the derivate is denoted with an N to explicitly state that the derivation is made in the N-frame. The connection between the Newtonian, N-frame derivation and the rotating intermediate, I-frame derivation is:

$$\frac{{}^N d()}{dt} = \frac{{}^I d()}{dt} + \Omega \times () \tag{4.3}$$

Applying this to the relative I-frame position, $\mathbf{r}$, of the above yields:

$$\frac{{}^N d\mathbf{r}}{dt} = \frac{{}^I d\mathbf{r}}{dt} + \Omega \times \mathbf{r} = \mathbf{v} + \Omega \times \mathbf{r} \tag{4.4}$$

and the derivation of the positional vector, $\mathbf{R}_0$, of the intermediate frame is:

$$\frac{{}^N d\mathbf{R}_0}{dt} = \mathbf{V}_0 \tag{4.5}$$

where $\mathbf{v}$ is the velocity of P relative to I, $\mathbf{V}_0$ is the velocity of the origin of I relative to N, and the cross product, $\Omega \times \mathbf{r}$, is the tangential velocity of P in I owing to the rotation of I relative to N.
The velocity in the N-frame can now be written:

$$\underbrace{\mathbf{V}}_{\text{inertial}} = \underbrace{\mathbf{v}}_{\text{local}} + \underbrace{\mathbf{V}_0}_{\text{origin}} + \underbrace{\Omega \times \mathbf{r}}_{\text{tangential}} \tag{4.6}$$

where $\mathbf{V}$ is the velocity of point P relative to the Newtonian frame, N.
The time derivation of velocity yields the acceleration:

$$\mathbf{A} = \frac{{}^N d\mathbf{V}}{dt} = \frac{{}^N d\mathbf{v}}{dt} + \frac{{}^N d\mathbf{V}_0}{dt} + \frac{{}^N d(\Omega \times \mathbf{r})}{dt} \tag{4.7}$$

Using the identity between the Newtonian frame, N, and the intermediate frame, I, Eq. 4.3 on the three acceleration terms of the above equation yields:

$$\begin{aligned} \frac{{}^N d\mathbf{v}}{dt} &= \frac{{}^I d\mathbf{v}}{dt} + \Omega \times \mathbf{v} \\ \frac{{}^N d\mathbf{V}_0}{dt} &= \mathbf{A}_0 \\ \frac{{}^N d(\Omega \times \mathbf{r})}{dt} &= \frac{{}^I d(\Omega \times \mathbf{r})}{dt} + \Omega \times (\Omega \times \mathbf{r}) \end{aligned} \tag{4.8}$$

The last relation includes the term ${}^I d(\Omega \times \mathbf{r})/dt$, which can be changed to read:

$$\frac{{}^I d(\Omega \times \mathbf{r})}{dt} = \Omega \times \frac{{}^I d\mathbf{r}}{dt} + \mathbf{r} \times \frac{{}^I d\Omega}{dt} = \Omega \times \mathbf{v} + \mathbf{r} \times \alpha \tag{4.9}$$

The time derivate of the rotational velocity, α, the tangential acceleration, is defined as: $\alpha = {}^I d\Omega/dt \equiv {}^N d\Omega/dt$. The derivates are equivalent since $\Omega \times \Omega = 0$, see Eq. 4.3. The accelerations terms are summed up below:

$$\underbrace{\mathbf{A}}_{\text{inertial}} = \underbrace{\mathbf{a}}_{\text{local}} + \underbrace{\mathbf{A}_0}_{\text{origin}} + \underbrace{\Omega \times (\Omega \times \mathbf{r})}_{\text{centripetal}} + \underbrace{2\Omega \times \mathbf{v}}_{\text{Coriolis}} + \underbrace{\alpha \times \mathbf{r}}_{\text{tangential}} \tag{4.10}$$

As stated above, we are looking for the Navier-Stokes equation in the intermediate frame, I. The acceleration properties of P in the Newtonian frame, N, expressed in the intermediate frame, I, can now be written with the aid of equation 4.10:

$${}^N\mathbf{A}^P = {}^I\mathbf{a}^P + \mathbf{A}_0 + \Omega \times (\Omega \times {}^I\mathbf{r}^P) + 2\Omega \times {}^I\mathbf{v}^P + \alpha \times {}^I\mathbf{r}^P \tag{4.11}$$

where ${}^I\mathbf{r}$, ${}^I\mathbf{v}^P$ and ${}^I\mathbf{a}^P$ are the positional vector, velocity vector and acceleration vector, respectively, for point P in the rotating intermediate frame, I.
The local acceleration in I frame is simply the substantial derivate of the velocity taken in the I frame:

$$ {}^I\mathbf{a}^P = \frac{{}^I D\mathbf{v}^P}{Dt} \tag{4.12} $$

Now the acceleration of the point P, in the intermediate frame I, with compensation for its non-inertiality is – drops all superscripts since all variables and derivates are taken in the local frame, I, apart from $\mathbf{A}_0$:

$$ \mathbf{A} = \frac{D\mathbf{v}}{Dt} + \mathbf{A}_0 + \Omega \times (\Omega \times \mathbf{r}) + 2\Omega \times \mathbf{v} + \alpha \times \mathbf{r} \tag{4.13} $$

4.2 Newton's Second Law of Motion in a Rotating Frame

In a non-inertial frame undergoing rotation, extra acceleration terms develop as is seen above. These are known as the Coriolis and centripetal acceleration terms.
Consider the fundamental governing equation, Newton's second law of motion:

$$ m\mathbf{A} = \mathbf{F} \tag{4.14} $$

The right-hand side (RHS) shows the forces from the outside, which generate an acceleration on the fluid element, the left-hand side (LHS). Note in this formulation that the acceleration is the acceleration in an inertial coordinate system. If this acceleration is changed to be the acceleration in a non-inertial frame, and assuming that the solid body rotation is constant (i.e. non-accelerating) ($\rightarrow \alpha = 0$) and that the intermediate (non-inertial) frame I in Fig. 4.1 is not accelerating relative to the Newtonian (inertial) frame N ($\rightarrow \mathbf{A}_0 = 0$), the Newton law is:

$$ m\left[\frac{D\mathbf{v}}{Dt} + \Omega \times (\Omega \times \mathbf{r}) + 2\Omega \times \mathbf{v}\right] = \mathbf{F} \tag{4.15} $$

The second term on the LHS of Eq. 4.15 is denoted the centripetal acceleration, and the third term is the Coriolis acceleration.

4.3 Rotationally Induced Body Forces

How will the above reformulation of the acceleration change the Navier-Stokes equation? The RHS of the Navier-Stokes equation, the forces, are unchanged and thus still consist of body forces and surfaces forces, but the LHS, the acceleration terms, have been divided into a relative acceleration term (the first term of the LHS) and two rotationally induced acceleration terms (the centripetal, the second term on the LHS, and Coriolis accelerations, the third term on the LHS of Eq. 4.15). If the Navier-Stokes formulation were written with the absolute acceleration, this rewriting would not be necessary. However, the problems involved in such a task far surpass the problems concerning the additional acceleration terms from a formulation in a relative coordinate system. This rewriting also benefits from the fact that the standard Navier-Stokes equation, written in the observed coordinate system, i.e. the relative coordinate system, will be unchanged by the rotation. In the case of a imposed solid body rotation the centrifugal force is:

$$ F_i^{co} = \Omega \times \Omega \times \mathbf{r} \cdot \text{mass} \tag{4.16} $$

Changing to tensorial formulation and dividing with mass gives:

$$f_i^{co} = \epsilon_{ijk}\epsilon_{klm}\Omega_j\Omega_l x_m \tag{4.17}$$

In a similar fashion, the Coriolis force is:

$$f_i^{ce} = 2\epsilon_{ijk}\Omega_j u_k \tag{4.18}$$

These terms should be included on the LHS of the Navier-Stokes equation, since they originate from the acceleration modification and not from any force from outside. However, as these are formally treated as body forces, they are moved to the RHS, and thus a negative sign is added:

$$f_i^{ce} = -\epsilon_{ijk}\epsilon_{klm}\Omega_j\Omega_l x_m \tag{4.19}$$

$$f_i^{co} = -2\epsilon_{ijk}\Omega_j u_k \tag{4.20}$$

Note that these 'forces' are not actually forces, since they originates as acceleration-modifiers due to the imposed solid body rotation. The total body force is the sum of all acceleration forces, the gravitational, centrifugal and Coriolis-induced forces:

$$f_i^{body} = f_i^{grav} + f_i^{ce} + f_i^{co} \tag{4.21}$$

Where the gravitional force is unaffected by the rotation.

4.4 Rotationally Induced Surface Forces

As indicated above, the rotationally induced body forces are not really forces but rather a modification to the acceleration term, owing to the non-inertial coordinate system. With this in mind, it is not difficult to understand that the surface forces – similar to the gravitional force – are not affected by any solid body rotation.

4.5 Rotational Navier-Stokes Equation

Summing up the results from the above sections, the Navier Stokes equation, Eq. 3.9, for a rotating incompressible case is:

$$\frac{\partial \rho u_i}{\partial t} + \frac{\partial \rho u_j u_i}{\partial x_j} = \rho g_i - \frac{\partial p}{\partial x_i} - \rho\epsilon_{ijk}\epsilon_{klm}\Omega_j\Omega_l x_m - 2\varepsilon_{ijk}\Omega_j u_k + \frac{\partial}{\partial x_j}\left(2\mu s_{ij}\right) \tag{4.22}$$

The above formulation is usually called the *conservative* form of the Navier-Stokes equation. With the help of the continuity equation this can be changed into the *non-conservative* equation. Take the LHS of the above equation and change it according to:

$$\begin{aligned}\frac{\partial \rho u_i}{\partial t} + \frac{\partial \rho u_j u_i}{\partial x_j} &= \rho\frac{\partial u_i}{\partial t} + u_i\frac{\partial \rho}{\partial t} + \rho u_j\frac{\partial u_i}{\partial x_j} + u_i\frac{\partial \rho u_j}{\partial u_j} = \\ \rho\frac{\partial u_i}{\partial t} + \rho u_j\frac{\partial u_i}{\partial x_j} + u_i\underbrace{\left(\frac{\partial \rho}{\partial t} + \frac{\partial \rho u_j}{\partial u_j}\right)}_{=0} &= \rho\frac{\partial u_i}{\partial t} + \rho u_j\frac{\partial u_i}{\partial x_j}\end{aligned} \tag{4.23}$$

where the continuity equation gives the zero on the second line.
The non-conservative Navier-Stokes equation can then be written in short-hand as:

$$\mathcal{N}(u_i) = \rho\frac{\partial u_i}{\partial t} + \rho u_j\frac{\partial u_i}{\partial x_j} - \rho g_i + \rho\epsilon_{ijk}\epsilon_{klm}\Omega_j\Omega_l x_m + 2\rho\epsilon_{ijk}\Omega_j u_k + \frac{\partial p}{\partial x_i} - \frac{\partial}{\partial x_j}(2\mu s_{ij}) = 0 \tag{4.24}$$

In the case of a incompressible flow with constant viscosity, the viscous term can be re-written according to:

$$\frac{\partial}{\partial x_j}(2\mu s_{ij}) = \frac{\partial}{\partial x_j}\left[\mu\left(\frac{\partial u_i}{\partial x_j} + \frac{\partial u_j}{\partial x_i}\right)\right] = \mu\left(\frac{\partial^2 u_i}{\partial x_j^2} + \frac{\partial^2 u_j}{\partial x_i x_j}\right) = \mu\frac{\partial^2 u_i}{\partial x_j^2} \tag{4.25}$$

where the continuity equation cancels the second term.

4.6 The Modified Pressure Equation

If the particular flow of interest can be considered incompressible with constant material properties, the Navier-Stokes equation can be simplified. The similarity of: the pressure, centrifugal force and the gravitational force, allows them to be lumped together. The pressure field is naturally a potential function and forms the basis of the concept, in which the other two are included. If the structure is rotating with a constant angular velocity around a fixed rotational axis, the centrifugal force can also be written as a potential function, since the force is dependent only on the distance to the center of revolution:

$$f_i^{ce} = -\epsilon_{ijk}\epsilon_{klm}\Omega_j\Omega_l x_m \tag{4.26}$$

By assuming a negligible variation in gravitational acceleration, the gravitional force is a conservative force and is thus also a potential function:

$$f_i^{grav} = g_i \tag{4.27}$$

Adding them together with the pressure gradient yields:

$$-\frac{\partial p^*}{\partial x_i} = -\frac{\partial p}{\partial x_i} + \rho g_i - \rho\epsilon_{ijk}\epsilon_{klm}\Omega_j\Omega_l x_m \tag{4.28}$$

where p is the thermodynamic pressure. By integrating the above equation, the relation for the *reduced pressure* [15], p^*, is found as:

$$-p^* = -p + \rho g z - \frac{1}{2}\rho\epsilon_{ijk}\epsilon_{klm}x_i\Omega_j\Omega_l x_m \tag{4.29}$$

4.7 Rotational Vorticity Equation

In both rotating and non-rotating flows, the vorticity can be used to interpret the effect of the viscous forces. Vorticity is equal to the angular velocity of a fluid element except for a factor of 0.5, and hence it is an indicator of the solid body rotation of a fluid element. Because neither the pressure nor the gravitional forces contribute to any solid body rotation, the vorticity equation is well suited for studying the viscous forces. The vorticity is defined as the curl of the velocity field:

$$\omega_i = \epsilon_{ijk}\frac{\partial u_k}{\partial x_j} \tag{4.30}$$

With the use of the momentum equation in the non-conservative form, Eq. 4.24, and by rewriting the convective term, the dynamic equation for vorticity can be written. The second term on the RHS of the momentum equation can be changed into a kinetic energy and a rotation term with the following vector identity:

$$\rho u_j \frac{\partial u_i}{\partial x_j} = \rho \frac{\partial}{\partial x_i}\left(\frac{1}{2}u_j u_j\right) + \rho \epsilon_{ijk}\omega_j u_k \tag{4.31}$$

Substituting this into Eq. 4.24 yields:

$$\begin{aligned} \rho\frac{\partial u_i}{\partial t} + \rho\frac{\partial}{\partial x_i}\left(\frac{1}{2}u_j u_j\right) + \rho\epsilon_{ijk}\omega_j u_k = \\ \rho g_i - \rho\epsilon_{ijk}\epsilon_{klm}\Omega_j\Omega_l x_m - 2\rho\epsilon_{ijk}\Omega_j u_k - \frac{\partial p}{\partial x_i} + \frac{\partial}{\partial x_j}\left(2\mu s_{ij}\right) \end{aligned} \tag{4.32}$$

To simplify the mathematical treatment, the pressure, gravitional force and centrifugal force are substituted into a reduced pressure term:

$$-\frac{\partial p^*}{\partial x_i} = \rho g_i - \rho\epsilon_{ijk}\epsilon_{klm}\Omega_j\Omega_l x_m - \frac{\partial p}{\partial x_i} \tag{4.33}$$

where p^* is the reduced pressure.
This equation is differentiated with $\partial/\partial x_q$ and multiplied with ϵ_{pqi}:

$$\begin{aligned} \rho\epsilon_{pqi}\frac{\partial^2 u_i}{\partial t \partial x_q} + \rho\epsilon_{pqi}\frac{\partial^2}{\partial x_i \partial x_q}\left(\frac{1}{2}u_j u_j\right) + \rho\epsilon_{pqi}\frac{\partial}{\partial x_q}\left(\epsilon_{ijk}\omega_j u_k\right) = \\ -2\rho\epsilon_{pqi}\epsilon_{ijk}\frac{\partial}{\partial x_q}\left(\Omega_j u_k\right) - \epsilon_{pqi}\frac{\partial^2 p^*}{\partial x_i \partial x_q} + \epsilon_{pqi}\frac{\partial^2}{\partial x_j \partial x_q}\left(2\mu s_{ij}\right) \end{aligned} \tag{4.34}$$

The second term on the LHS above is zero because ϵ_{pqi} is antisymmetric and $\partial^2/\partial x_i \partial x_q$ is symmetric – the curl of a gradient equals zero. The reduced pressure term disappears for the same reason. These identities reduce the equation to:

$$\rho\epsilon_{pqi}\frac{\partial^2 u_i}{\partial t \partial x_q} + \rho\epsilon_{pqi}\frac{\partial}{\partial x_q}\left(\epsilon_{ijk}\omega_j u_k\right) = -2\rho\epsilon_{pqi}\epsilon_{ijk}\frac{\partial}{\partial x_q}\left(\Omega_j u_k\right) + \epsilon_{pqi}\frac{\partial^2}{\partial x_j \partial x_q}\left(2\mu s_{ij}\right) \tag{4.35}$$

The second term on the LHS can be rewritten as:

$$\rho\epsilon_{pqi}\frac{\partial}{\partial x_q}\left(\epsilon_{ijk}\omega_j u_k\right) = \rho\frac{\partial}{\partial x_k}\left(\omega_p u_k\right) - \rho\frac{\partial}{\partial x_j}\left(\omega_j u_p\right) = \rho u_k\frac{\partial \omega_p}{\partial x_k} - \rho\omega_j\frac{\partial u_p}{\partial x_j} \tag{4.36}$$

The second identity arises from the incompressibility assumption, where $\partial u_k/\partial x_k$ and $\partial \omega_j/\partial x_j$ are always equal to zero. The Coriolis force can be rewritten in a similar fashion:

$$2\rho\epsilon_{pqi}\epsilon_{ijk}\frac{\partial}{\partial x_q}\left(\Omega_j u_k\right) = 2\rho u_k\frac{\partial \Omega_p}{\partial x_k} - 2\rho\Omega_j\frac{\partial u_p}{\partial x_j} \tag{4.37}$$

Inserting these into the vorticity equation yields:

$$\rho\epsilon_{pqi}\frac{\partial^2 u_i}{\partial t \partial x_q} + \rho u_k\frac{\partial \omega_p}{\partial x_k} - \rho\omega_j\frac{\partial u_p}{\partial x_j} = -2\rho u_k\frac{\partial \Omega_p}{\partial x_k} + 2\rho\Omega_j\frac{\partial u_p}{\partial x_j} + \epsilon_{pqi}\frac{\partial^2}{\partial x_j \partial x_q}\left(2\mu s_{ij}\right) \tag{4.38}$$

With the assumption of constant viscosity, the viscous term can be changed to:

$$\epsilon_{pqi}\frac{\partial^2}{\partial x_j \partial x_q}\left(2\mu s_{ij}\right) = \mu\epsilon_{pqi}\frac{\partial^3 u_i}{\partial x_j^2 \partial x_q} \tag{4.39}$$

With the definition of the vorticity, see Eq. 4.30, this can be written as:

$$= \mu\frac{\partial^2 \omega_i}{\partial x_j^2} \tag{4.40}$$

and hence the final result for the vorticity equation is:

$$\rho\frac{\partial \omega_i}{\partial t} + \rho u_j\frac{\partial \omega_i}{\partial x_j} + 2\rho u_j\frac{\partial \Omega_i}{\partial x_j} = \rho\omega_j\frac{\partial u_i}{\partial x_j} + 2\rho\Omega_j\frac{\partial u_i}{\partial x_j} + \mu\frac{\partial^2 \omega_i}{\partial x_j^2} \tag{4.41}$$

5 Turbulence

5.1 Reynolds Averaging

The Reynolds averaging procedure is well known in fluid mechanics and is the procedure that results in the Reynolds stresses. The Reynolds stresses (six different) are the unknown in the governing equation and represent the reason for there being a discipline called turbulence *modeling*. The Reynolds decomposition splits each quantity into its mean and fluctuating part:

$$\psi = \overline{\psi} + \psi' \tag{5.1}$$

Applying the Reynolds averaging, the mean part is time-averaged according to[5]:

$$\overline{\psi}_T(x) = \frac{1}{T}\int_t^{t+T} \psi(x,t)dt \tag{5.2}$$

Note that the mean part is written with either an overbar $\overline{\psi}$, or in uppercase letters, Ψ. If $\phi = \Phi + \phi'$ and $\psi = \Psi + \psi'$ are flow variables obeying the Reynolds-averaging rules, the following applies:

$$\begin{aligned} \overline{\Psi} = \Psi, \qquad \overline{\Phi} &= \Phi \\ \overline{\psi\phi} &= \Psi\Phi + \overline{\psi'\phi'} \\ \overline{\psi'} = \overline{\phi'} &= 0 \\ \overline{\Psi\phi'} = \overline{\Phi\psi'} &= 0 \end{aligned} \tag{5.3}$$

5.2 RANS, Reynolds Average Navier-Stokes Equation

Applying the Reynolds decomposition to the incompressible conservative Navier-Stokes equation, Eq. 4.22, with constant viscosity, Eq. 4.25, yields:

$$\begin{aligned} \frac{\partial \rho(U_i + u_i')}{\partial t} + \frac{\partial \rho(U_j + u_j')(U_i + u_i')}{\partial x_j} = \\ \rho g_i - \rho\epsilon_{ijk}\epsilon_{klm}\Omega_j\Omega_l x_m - 2\rho\epsilon_{ijk}\Omega_j(U_k + u_k') - \frac{\partial(P+p')}{\partial x_i} + \frac{\partial}{\partial x_j}\left(\mu\frac{\partial(U_i+u_i')}{\partial x_j}\right) \end{aligned} \tag{5.4}$$

where incompressible flow and constant solid body rotation are assumed.
The above equation is split into its mean and fluctuating terms and is time-averaged:

$$\begin{aligned} \overline{\frac{\partial \rho U_i}{\partial t}} + \overline{\frac{\partial \rho u_i'}{\partial t}} + \overline{\frac{\partial \rho U_j U_i}{\partial x_j}} + \overline{\frac{\partial \rho U_j u_i'}{\partial x_j}} + \overline{\frac{\partial \rho U_i u_j'}{\partial x_j}} + \overline{\frac{\partial \rho u_j' u_i'}{\partial x_j}} = \overline{\rho g_i} - \overline{\frac{\partial P}{\partial x_i}} - \overline{\frac{\partial p'}{\partial x_i}} - \\ \overline{\epsilon_{ijk}\epsilon_{klm}\Omega_j\Omega_l x_m} - \overline{2\epsilon_{ijk}\Omega_j U_k} - \overline{2\epsilon_{ijk}\Omega_j u_k'} + \overline{\frac{\partial}{\partial x_j}\left(\mu\frac{\partial U_i}{\partial x_j}\right)} + \overline{\frac{\partial}{\partial x_j}\left(\mu\frac{\partial u_i'}{\partial x_j}\right)} \end{aligned} \tag{5.5}$$

[5]Here only time-average will be used. However, there also exists space-, ensemble-, mass, and conditional-averaging procedures, see e.g. Hinze [19].

Applying the Reynolds averaging rules, Eq. 5.3, to this equation yields the Reynolds-averaged Navier-Stokes (RANS) equation in a constant rotating frame:

$$\begin{aligned} \frac{\partial \rho U_i}{\partial t} + \frac{\partial \rho U_j U_i}{\partial x_j} + \frac{\partial \rho \overline{u_j' u_i'}}{\partial x_j} = \\ \rho g_i - \rho \epsilon_{ijk} \epsilon_{klm} \Omega_j \Omega_l x_m - 2\rho \epsilon_{ijk} \Omega_j U_k - \frac{\partial P}{\partial x_i} + \frac{\partial}{\partial x_j} \left(\mu \frac{\partial U_i}{\partial x_j} \right) \end{aligned} \tag{5.6}$$

This equation can be rewritten to the non-conservative form in a similar manner as for the Navier-Stokes equation, Eq. 4.24, with its short-hand notation equal to:

$$\overline{\mathcal{N}(u_i)} = \rho \frac{\partial U_i}{\partial t} + \rho U_j \frac{\partial U_i}{\partial x_j} + \frac{\partial \rho \overline{u_j' u_i'}}{\partial x_j} - \rho g_i + \rho \epsilon_{ijk} \epsilon_{klm} \Omega_j \Omega_l x_m + 2\rho \epsilon_{ijk} \Omega_j U_k + \frac{\partial P}{\partial x_i} - \frac{\partial}{\partial x_j} \left(\mu \frac{\partial U_i}{\partial x_j} \right) = 0 \tag{5.7}$$

5.3 Reynolds Stresses

To produce an equation for the Reynolds stresses, the Navier-Stokes equation is used according to the following:

$$\overline{u_i' \mathcal{N}(u_j) + u_j' \mathcal{N}(u_i)} = 0 \tag{5.8}$$

where $\mathcal{N}(u_i)$ is the Navier-Stokes equation according to Eq. 4.24.
Writing out the terms yields:

$$\begin{aligned} \overline{u_i' \mathcal{N}(u_j) + u_j' \mathcal{N}(u_i)} = 0 = \\ \overline{u_i' \rho \frac{\partial u_j}{\partial t} + u_i' \rho u_k \frac{\partial u_j}{\partial x_k} - u_i' \rho g_j + u_i' \rho \epsilon_{jkl} \epsilon_{lmn} \Omega_k \Omega_m x_n} + \\ \overline{u_i' 2\rho \epsilon_{jkl} \Omega_k u_l + u_i' \frac{\partial p}{\partial x_k} \delta_{jk} - u_i' \frac{\partial}{\partial x_k} \left(\mu \frac{\partial u_j}{\partial x_k} \right)} + \\ \overline{u_j' \rho \frac{\partial u_i}{\partial t} + u_j' \rho u_k \frac{\partial u_i}{\partial x_k} - u_j' \rho g_i + u_j' \rho \epsilon_{ikl} \epsilon_{lmn} \Omega_k \Omega_m x_n} + \\ \overline{u_j' 2\rho \epsilon_{ikl} \Omega_k u_l + u_j' \frac{\partial p}{\partial x_k} \delta_{ik} - u_j' \frac{\partial}{\partial x_k} \left(\mu \frac{\partial u_i}{\partial x_k} \right)} \end{aligned} \tag{5.9}$$

where constant viscosity is assumed.
In order to make the mathematical treatment easier, the above equation is split into its different terms.

5.3.1 Unsteady Term

Starting with the unsteady terms:

$$\overline{u_i' \rho \frac{\partial u_j}{\partial t} + u_j' \rho \frac{\partial u_i}{\partial t}} \tag{5.10}$$

Inserting the mean and fluctuating parts, and splitting the terms yields:

$$= \overline{u_i' \rho \frac{\partial U_j}{\partial t}} + \overline{u_i' \rho \frac{\partial u_j'}{\partial t}} + \overline{u_j' \rho \frac{\partial U_i}{\partial t}} + \overline{u_j' \rho \frac{\partial u_i'}{\partial t}} \tag{5.11}$$

According to the Reynolds averaging rules, Eq. 5.3 the two terms including the mean velocity are zero:

$$= \overline{u_i \rho \frac{\partial u_j'}{\partial t}} + \overline{u_j' \rho \frac{\partial u_i'}{\partial t}} \tag{5.12}$$

Using the product rule for derivatives in the two remaining terms yields[6]:

$$= \rho \frac{\partial \overline{u_i' u_j'}}{\partial t} \tag{5.14}$$

5.3.2 Convective Term

The convective terms are:

$$\overline{u_i' \rho u_k \frac{\partial u_j}{\partial x_k} + u_j' \rho u_k \frac{\partial u_i}{\partial x_k}} \tag{5.15}$$

Inserting the mean and fluctuating part, and splitting the terms:

$$\begin{aligned} = \overline{u_i' \rho U_k \frac{\partial U_j}{\partial x_k}} + \overline{u_i' \rho U_k \frac{\partial u_j'}{\partial x_k}} + \overline{u_j' \rho U_k \frac{\partial U_i}{\partial x_k}} + \overline{u_j' \rho U_k \frac{\partial u_i'}{\partial x_k}} + \\ \overline{u_i' \rho u_k' \frac{\partial U_j}{\partial x_k}} + \overline{u_i' \rho u_k' \frac{\partial u_j'}{\partial x_k}} + \overline{u_j' \rho u_k' \frac{\partial U_i}{\partial x_k}} + \overline{u_j' \rho u_k' \frac{\partial u_i'}{\partial x_k}} \end{aligned} \tag{5.16}$$

Terms with only one fluctuating velocity are zero:

$$\begin{aligned} = \overline{u_i' \rho u_k' \frac{\partial U_j}{\partial x_k}} + \overline{u_j' \rho u_k' \frac{\partial U_i}{\partial x_k}} + \\ \overline{u_i' \rho U_k \frac{\partial u_j'}{\partial x_k}} + \overline{u_j' \rho U_k \frac{\partial u_i'}{\partial x_k}} + \overline{u_i' \rho u_k' \frac{\partial u_j'}{\partial x_k}} + \overline{u_j' \rho u_k' \frac{\partial u_i'}{\partial x_k}} \end{aligned} \tag{5.17}$$

The first two terms above are not changed. The next two sets of terms (2×2) can be combined with the help of the product rule for derivatives in reverse:

$$\overline{u_i' \rho U_k \frac{\partial u_j'}{\partial x_k}} + \overline{u_j' \rho U_k \frac{\partial u_i'}{\partial x_k}} + \overline{u_i' \rho u_k' \frac{\partial u_j'}{\partial x_k}} + \overline{u_j' \rho u_k' \frac{\partial u_i'}{\partial x_k}} = \rho U_k \frac{\partial \overline{u_i' u_j'}}{\partial x_k} + \overline{\rho u_k' \frac{\partial u_i' u_j'}{\partial x_k}} \tag{5.18}$$

Incompressible[7] flow is assumed for the final version, and thus the last term above can be rewritten as:

$$\overline{\rho u_k' \frac{\partial u_i' u_j'}{\partial x_k}} + \underbrace{\overline{\rho u_i' u_j' \frac{\partial u_k'}{\partial x_k}}}_{=0} = \rho \frac{\partial \overline{u_k' u_i' u_j'}}{\partial x_k} \tag{5.19}$$

Adding this together, the convective terms gives:

$$\rho \overline{u_i' u_k'} \frac{\partial U_j}{\partial x_k} + \rho \overline{u_j' u_k'} \frac{\partial U_i}{\partial x_k} + \rho U_k \frac{\partial \overline{u_i' u_j'}}{\partial x_k} + \rho \frac{\partial \overline{u_k' u_i' u_j'}}{\partial x_k} \tag{5.20}$$

[6]The product rule for derivatives is used in the reversed order. However, it is usually easier to operate it on the results and see whether the two terms are recovered:

$$\rho \frac{\partial \overline{u_i' u_j'}}{\partial t} = \rho \overline{u_i' \frac{\partial u_j'}{\partial t}} + \rho \overline{u_j' \frac{\partial u_i'}{\partial t}} \tag{5.13}$$

Later, this check is not made, and the reader is assumed to be familiar with the product rule, especially its operation in reverse.

[7]If ρ is constant, the continuity equation gives $\partial u_i / \partial x_i \equiv 0$

5.3.3 Body Force

The body forces are the gravitational, centrifugal and Coriolis forces:

$$\begin{array}{l} -\overline{u_i'\rho g_j + u_i'\rho\epsilon_{jkl}\epsilon_{lmn}\Omega_k\Omega_m x_n + 2u_i'\rho\epsilon_{jkl}\Omega_k u_l} \\ -\overline{u_j'\rho g_i + u_j'\rho\epsilon_{ikl}\epsilon_{lmn}\Omega_k\Omega_m x_n + 2u_j'\rho\epsilon_{ikl}\Omega_k u_l} \end{array} \tag{5.21}$$

Without further treatment, the gravitational and centrifugal terms are zero owing to the fact that they simply represent a fluctuating velocity multiplied by a constant amplitude[8]. The Coriolis term is split into its fluctuating and mean part:

$$= \overline{2u_i'\rho\epsilon_{jkl}\Omega_k U_l} + \overline{2u_i'\rho\epsilon_{jkl}\Omega_k u_l'} + \overline{2u_j'\rho\epsilon_{ikl}\Omega_k U_l} + \overline{2u_j'\rho\epsilon_{ikl}\Omega_k u_l'} \tag{5.22}$$

The time-average of a fluctuating velocity multiplied by a constant amplitude will be zero, and thus the only non-zero terms of the body forces are :

$$= \overline{2u_i'\rho\epsilon_{jkl}\Omega_k u_l'} + \overline{2u_j'\rho\epsilon_{ikl}\Omega_k u_l'} \tag{5.23}$$

5.3.4 Pressure term

The pressure terms are:

$$\overline{u_i'\frac{\partial p}{\partial x_j} + u_j'\frac{\partial p}{\partial x_i}} \tag{5.24}$$

Taking the mean and fluctuating part of the pressure:

$$= \overline{u_i'\frac{\partial P}{\partial x_j}} + \overline{u_i'\frac{\partial p'}{\partial x_j}} + \overline{u_j'\frac{\partial P}{\partial x_i}} + \overline{u_j'\frac{\partial p'}{\partial x_i}} \tag{5.25}$$

the mean pressure terms are zero:

$$= \overline{u_i'\frac{\partial p'}{\partial x_j}} + \overline{u_j'\frac{\partial p'}{\partial x_i}} \tag{5.26}$$

The remaining terms are reformulated with the product rule for derivatives to yield:

$$= \overline{\frac{\partial u_i'p'}{\partial x_j}} - \overline{p'\frac{\partial u_i'}{\partial x_j}} + \overline{\frac{\partial u_j'p'}{\partial x_i}} - \overline{p'\frac{\partial u_j'}{\partial x_i}} \tag{5.27}$$

Collecting terms gives the commonly recognizable terms:

$$= \overline{\frac{\partial u_i'p'}{\partial x_j}} + \overline{\frac{\partial u_j'p'}{\partial x_i}} - \overline{p'\left(\frac{\partial u_j'}{\partial x_i} + \frac{\partial u_i'}{\partial x_j}\right)} \tag{5.28}$$

The last term is the so called pressure-strain term, while the two first are the pressure-diffusion terms.

[8]Note that with a fluctuating density this can not be done.

5.3.5 Viscous Term

The last two terms to be dealt with are the viscous terms:

$$-\overline{u_j' \frac{\partial}{\partial x_k}\left(\mu \frac{\partial u_i}{\partial x_k}\right) - u_i' \frac{\partial}{\partial x_k}\left(\mu \frac{\partial u_j}{\partial x_k}\right)} \tag{5.29}$$

Splitting into its mean and fluctuating part:

$$= -\overline{u_j' \frac{\partial}{\partial x_k}\left(\mu \frac{\partial U_i}{\partial x_k}\right)} - \overline{u_j' \frac{\partial}{\partial x_k}\left(\mu \frac{\partial u_i'}{\partial x_k}\right)} - \overline{u_i' \frac{\partial}{\partial x_k}\left(\mu \frac{\partial U_j}{\partial x_k}\right)} - \overline{u_i' \frac{\partial}{\partial x_k}\left(\mu \frac{\partial u_j'}{\partial x_k}\right)} \tag{5.30}$$

Terms with only one fluctuating velocity are zero:

$$= -\overline{u_j' \frac{\partial}{\partial x_k}\left(\mu \frac{\partial u_i'}{\partial x_k}\right)} - \overline{u_i' \frac{\partial}{\partial x_k}\left(\mu \frac{\partial u_j'}{\partial x_k}\right)} \tag{5.31}$$

Using the product rule for derivatives in reverse gives [9]:

$$= -\mu \frac{\partial}{\partial x_k}\left(\overline{u_j' \frac{\partial u_i'}{\partial x_k}}\right) - \mu \frac{\partial}{\partial x_k}\left(\overline{u_i' \frac{\partial u_j'}{\partial x_k}}\right) + 2\mu \overline{\frac{\partial u_j'}{\partial x_k}\frac{\partial u_i'}{\partial x_k}} \tag{5.32}$$

Applying the product rule in reverse on the two first terms of above gives:

$$-\mu \frac{\partial}{\partial x_k}\left(\overline{u_j' \frac{\partial u_i'}{\partial x_k}}\right) - \mu \frac{\partial}{\partial x_k}\left(\overline{u_i' \frac{\partial u_j'}{\partial x_k}}\right) = -\mu \frac{\partial^2 \overline{u_i' u_j'}}{\partial x_k x_k} \tag{5.33}$$

The final result is:

$$2\mu \overline{\frac{\partial u_j'}{\partial x_k}\frac{\partial u_i'}{\partial x_k}} - \mu \frac{\partial^2 \overline{u_i' u_j'}}{\partial x_k x_k} \tag{5.34}$$

where the first term is the viscous dissipation and the second is the viscous diffusion.

5.3.6 Reynolds Stress Equation

Collecting the terms from above gives the differential equation for the Reynolds stresses:

$$\begin{aligned} \rho \frac{\partial \overline{u_i' u_j'}}{\partial t} + \rho U_k \frac{\partial \overline{u_i' u_j'}}{\partial x_k} &= -\rho \overline{u_i' u_k'} \frac{\partial U_j}{\partial x_k} - \rho \overline{u_j' u_k'} \frac{\partial U_i}{\partial x_k} \\ -2\Omega_k \rho \left(\epsilon_{jkl} \overline{u_i' u_l'} + \epsilon_{ikl} \overline{u_j' u_l'}\right) + \overline{p'\left(\frac{\partial u_j'}{\partial x_i} + \frac{\partial u_i'}{\partial x_j}\right)} &+ \mu \frac{\partial^2 \overline{u_i' u_j'}}{\partial x_k x_k} - 2\mu \overline{\frac{\partial u_j'}{\partial x_k}\frac{\partial u_i'}{\partial x_k}} \\ -\overline{\frac{\partial u_i' p'}{\partial x_j}} - \overline{\frac{\partial u_j' p'}{\partial x_i}} &- \rho \frac{\partial \overline{u_k' u_i' u_j'}}{\partial x_k} \end{aligned} \tag{5.35}$$

This equation is usually written in short-hand with the following symbols:

$$\frac{DR_{ij}}{Dt} = P_{ij} + G_{ij} + \Pi_{ij} - \varepsilon_{ij} + \frac{\partial D_{ij}}{\partial x_k} + \frac{\partial D_{ij}^{\nu}}{\partial x_k} \tag{5.36}$$

[9] Assuming constant viscosity.

where the different terms denote:

$$\frac{DR_{ij}}{Dt} = \frac{\partial \overline{u_i' u_j'}}{\partial t} + U_k \frac{\partial \overline{u_i' u_j'}}{\partial x_k} \qquad \text{Convection}$$

$$P_{ij} = -\left(\overline{u_i' u_k'} \frac{\partial U_j}{\partial x_k} + \overline{u_j' u_k'} \frac{\partial U_i}{\partial x_k} \right) \qquad \text{Production}$$

$$G_{ij} = -2\Omega_k \left(\epsilon_{jkl} \overline{u_i' u_l'} + \epsilon_{ikl} \overline{u_j' u_l'} \right) \qquad \text{Generation}$$

$$\Pi_{ij} = \overline{\frac{p'}{\rho} \left(\frac{\partial u_j'}{\partial x_i} + \frac{\partial u_i'}{\partial x_j} \right)} \qquad \text{Pressure-strain}$$

$$\varepsilon_{ij} = 2\nu \overline{\frac{\partial u_j'}{\partial x_k} \frac{\partial u_i'}{\partial x_k}} \qquad \text{Dissipation}$$

$$D_{ij} = -\left(\overline{\frac{u_i' p'}{\rho}} \delta_{jk} + \overline{\frac{u_j' p'}{\rho}} \delta_{ik} + \overline{u_k' u_i' u_j'} \right) \qquad \text{Diffusion}$$

$$D_{ij}^{\nu} = -\nu \frac{\partial \overline{u_i' u_j'}}{\partial x_k} \qquad \text{Viscous diffusion}$$

5.4 Turbulent Kinetic Energy Equation

The differential equation for the turbulent kinetic energy is easily derived from the above Reynolds stress equation by simply taking the trace of the Reynolds stresses:

$$k = \frac{1}{2} \overline{u_i' u_i'} \tag{5.37}$$

Applying this to the last form of the equation yields:

$$\frac{DR_{ii}}{Dt} = P_{ii} + G_{ii} + \Pi_{ii} - \varepsilon_{ii} + \frac{\partial D_{ii}}{\partial x_j} + \frac{\partial D_{ii}^{\nu}}{\partial x_j} \tag{5.38}$$

with

$$\frac{DR_{ii}}{Dt} = \frac{\partial \overline{u_i' u_i'}}{\partial t} + U_j \frac{\partial \overline{u_i' u_i'}}{\partial x_j} = \frac{D2k}{Dt}$$

$$P_{ii} = -\left(\overline{u_i' u_k'} \frac{\partial U_i}{\partial x_k} + \overline{u_i' u_k'} \frac{\partial U_i}{\partial x_k} \right) = -2 \overline{u_i' u_j'} \frac{\partial U_i}{\partial x_j}$$

$$G_{ii} = -2\Omega_k \left(\epsilon_{ikl} \overline{u_i' u_l'} + \epsilon_{ikl} \overline{u_i' u_l'} \right) = -4\Omega_j \epsilon_{ijk} \overline{u_i' u_k'} = 0$$

$$\Pi_{ii} = \overline{\frac{p'}{\rho} \left(\frac{\partial u_i'}{\partial x_i} + \frac{\partial u_i'}{\partial x_i} \right)} = 0$$

$$\varepsilon_{ii} = 2\nu \overline{\frac{\partial u_i'}{\partial x_k} \frac{\partial u_i'}{\partial x_k}} = 2\nu \overline{\left(\frac{\partial u_i'}{\partial x_j} \right)^2}$$

$$D_{ii} = -\left(\overline{\frac{u_i' p'}{\rho}} \delta_{ii} + \overline{\frac{u_i' p'}{\rho}} \delta_{ii} + \overline{u_k' u_i' u_i'} \right) = -\left(2 \overline{\frac{u_i' p'}{\rho}} + \overline{u_j' u_i' u_i'} \right)$$

$$D_{ii}^{\nu} = -\nu \frac{\partial \overline{u_i' u_i'}}{x_k} = -\nu \frac{\partial 2k}{\partial x_j}$$

Writing the $k-$equation explicitly gives:

$$\frac{Dk}{Dt} = P_k - \varepsilon + \frac{\partial}{\partial x_j}\left(D_j + D_j^{\nu}\right) \tag{5.39}$$

with

$$\begin{aligned} P_k &= -\overline{u_i' u_j'}\frac{\partial U_i}{\partial x_j} \\ \varepsilon &= \nu\overline{\left(\frac{\partial u_i'}{\partial x_j}\right)^2} \\ D_j &= -\left(\frac{\overline{u_j' p'}}{\rho} + \frac{1}{2}\overline{u_j' u_i' u_i'}\right) \\ D_j^{\nu} &= -\nu\frac{\partial k}{\partial x_j} \end{aligned}$$

5.5 Equation for the Fluctuating Velocity

Below the exact dissipation rate equation will be derived. However, in that derivation, the equation for the fluctuating velocity is needed. An equation for the fluctuating velocities can be obtained by using the following operation with the Navier-Stokes equation:

$$\mathcal{N}(u_i) - \overline{\mathcal{N}(u_i)} \rightarrow \text{Equation for } u_i' \tag{5.40}$$

thus taking the Navier-Stokes equation, Eq. 4.24 and subtracting the averaged Navier-Stokes equation, Eq. 5.7.
This is done below term by term, starting with the LHS[10]:

$$\begin{aligned} \rho\frac{\partial(U_i + u_i')}{\partial t} - \rho\frac{\partial U_i}{\partial t} &= \rho\frac{\partial u_i'}{\partial t} \\ \rho(U_j + u_j')\frac{\partial(U_i + u_i')}{\partial x_j} - \rho U_j\frac{\partial U_i}{\partial x_j} &= \rho u_j'\frac{\partial U_i}{\partial x_j} + \rho u_j'\frac{\partial u_i'}{\partial x_j} + \rho U_j\frac{\partial u_i'}{\partial x_j} \\ 0 - \frac{\partial\rho\overline{u_j' u_i'}}{\partial x_j} &= -\frac{\partial\rho\overline{u_j' u_i'}}{\partial x_j} \end{aligned}$$

and then the RHS[11]:

$$\begin{aligned} \rho g_i - \rho g_i &= 0 \\ -\rho\epsilon_{ijk}\epsilon_{klm}\Omega_j\Omega_l x_m - (-\rho\epsilon_{ijk}\epsilon_{klm}\Omega_j\Omega_l x_m) &= 0 \\ -2\rho\epsilon_{ijk}\Omega_j(U_k + u_k') - (-2\rho\epsilon_{ijk}\Omega_j U_k) &= -2\rho\epsilon_{ijk}\Omega_j u_k' \\ -\frac{\partial(P + p')}{\partial x_i} - \left(-\frac{\partial P}{\partial x_i}\right) &= -\frac{\partial p'}{\partial x_i} \\ \frac{\partial}{\partial x_j}\left(\mu\frac{\partial(U_i + u_i')}{\partial x_j}\right) - \frac{\partial}{\partial x_j}\left(\mu\frac{\partial U_i}{\partial x_j}\right) &= \frac{\partial}{\partial x_j}\left(\mu\frac{\partial u_i'}{\partial x_j}\right) \end{aligned}$$

[10] The time-dependent term, the convective term and the Reynolds-stresses.
[11] The gravitational, centrifugal, Coriolis and viscous terms.

The resulting equation, which is written as $\mathcal{N}(u_i')$, is:

$$\mathcal{N}(u_i') = \rho\frac{\partial u_i'}{\partial t} + \rho u_j'\frac{\partial U_i}{\partial x_j} + \rho u_j'\frac{\partial u_i'}{\partial x_j} + \rho U_j\frac{\partial u_i'}{\partial x_j} - \frac{\partial\rho\overline{u_j'u_i'}}{\partial x_j} + 2\rho\epsilon_{ijk}\Omega_j u_k' + \frac{\partial p'}{\partial x_i} - \frac{\partial}{\partial x_j}\left(\mu\frac{\partial u_i'}{\partial x_j}\right) = 0 \tag{5.41}$$

5.6 Dissipation Rate Equation

The dissipation rate, ε, which appeared above in the turbulent kinetic energy equation, is defined as

$$\varepsilon = \overline{\nu\frac{\partial u_i'}{\partial x_j}\frac{\partial u_i'}{\partial x_j}} \tag{5.42}$$

To arrive at a transport equation for the dissipation rate, the following operation is made with the Navier-Stokes equation:

$$2\nu\frac{\partial u_i'}{\partial x_k}\frac{\partial}{\partial x_k}\mathcal{N}(u_i') = 0 \tag{5.43}$$

where $\mathcal{N}(u_i')$ denotes the fluctuating Navier-Stokes equation, as given in Eq. 5.41. Writing this explicitly gives:

$$0 = \overline{2\nu\frac{\partial u_i'}{\partial x_k}\frac{\partial}{\partial x_k}\left[\rho\frac{\partial u_i'}{\partial t} + \rho U_j\frac{\partial u_i'}{\partial x_j} + \rho u_j'\frac{\partial U_i}{\partial x_j} + \rho u_j'\frac{\partial u_i'}{\partial x_j} - \frac{\partial\rho\overline{u_j'u_i'}}{\partial x_j} + 2\rho\epsilon_{ijk}\Omega_j u_k' + \frac{\partial p'}{\partial x_i} - \frac{\partial}{\partial x_j}\left(\mu\frac{\partial u_i'}{\partial x_j}\right)\right]} \tag{5.44}$$

Below the terms divided by density are treated separately.

5.6.1 Unsteady Term

Performing the above manipulation on the unsteady term produces:

$$2\nu\overline{\frac{\partial u_i'}{\partial x_k}\frac{\partial}{\partial x_k}\frac{\partial u_i'}{\partial t}} \tag{5.45}$$

Applying the spatial-derivative to the time-derivative, rearranging the derivation order and then substituting backwards through the product-rule, with two equal terms, yields:

$$= 2\nu\overline{\frac{\partial u_i'}{\partial x_k}\frac{\partial^2 u_i'}{\partial t\partial x_k}} = \nu\overline{\frac{\partial}{\partial t}\left(\frac{\partial u_i'}{\partial x_k}\frac{\partial u_i'}{\partial x_k}\right)} = \frac{\partial\varepsilon}{\partial t} \tag{5.46}$$

5.6.2 Convective Terms

It was seen above that the convective term in the Navier-Stokes equation actually becomes three different terms in the equation for the fluctuating velocity. These three convective terms are treated separately below.

1:st convective term Starting with the first term, which includes the velocities U_j and u_i':

$$2\nu\overline{\frac{\partial u_i'}{\partial x_k}\frac{\partial}{\partial x_k}\left(U_j\frac{\partial u_i'}{\partial x_j}\right)} \tag{5.47}$$

This term produces two terms in the transport equation, the convective term and a turbulent production term. Derivation of the above term yields:

$$= 2\nu\overline{\frac{\partial u_i'}{\partial x_k}\frac{\partial U_j}{\partial x_k}\frac{\partial u_i'}{\partial x_j}} + \nu\overline{\frac{\partial u_i'}{\partial x_k}U_j\frac{\partial^2 u_i'}{\partial x_j\partial x_k}} \tag{5.48}$$

The first term has already arrived at its final version, while the second term needs to be rewritten.

$$2\nu U_j\overline{\frac{\partial u_i'}{\partial x_k}\frac{\partial}{\partial x_j}\left(\frac{\partial u_i'}{\partial x_k}\right)} = U_j\frac{\partial}{\partial x_j}\overline{\left(\nu\frac{\partial u_i'}{\partial x_k}\frac{\partial u_i'}{\partial x_k}\right)} = U_j\frac{\partial \varepsilon}{\partial x_j} \tag{5.49}$$

where the first operation is a recognition of the product rule for derivatives. Summing up the first convective term gives:

$$2\nu\overline{\frac{\partial u_i'}{\partial x_k}\frac{\partial}{\partial x_k}\left(U_j\frac{\partial u_i'}{\partial x_j}\right)} = U_j\frac{\partial \varepsilon}{\partial x_j} + 2\nu\frac{\partial U_j}{\partial x_k}\overline{\frac{\partial u_i'}{\partial x_k}\frac{\partial u_i'}{\partial x_j}} \tag{5.50}$$

where the first term is the convective term and the second term is the turbulent production term.

2:nd convective term The second convective term is the term involving u_j' and U_i:

$$2\nu\overline{\frac{\partial u_i'}{\partial x_k}\frac{\partial}{\partial x_k}\left(u_j'\frac{\partial U_i}{\partial x_j}\right)} \tag{5.51}$$

Performing the derivation yields the two production terms:

$$= 2\nu\overline{\frac{\partial u_i'}{\partial x_k}\frac{\partial u_j'}{\partial x_k}}\frac{\partial U_i}{\partial x_j} + 2\nu\overline{\frac{\partial u_i'}{\partial x_k}u_j'}\frac{\partial^2 U_i}{\partial x_j\partial x_k} \tag{5.52}$$

3:rd convective term The third term is the term that includes the velocities u_j' and u_i':

$$2\nu\overline{\frac{\partial u_i'}{\partial x_k}\frac{\partial}{\partial x_k}\left(u_j'\frac{\partial u_i'}{\partial x_j}\right)} \tag{5.53}$$

This is somewhat more complicated. Start by performing the spatial-derivative on the last term:

$$= 2\nu\overline{\frac{\partial u_i'}{\partial x_k}\frac{\partial u_j'}{\partial x_k}\frac{\partial u_i'}{\partial x_j}} + 2\nu\overline{\frac{\partial u_i'}{\partial x_k}u_j'\frac{\partial^2 u_i'}{\partial x_j\partial x_k}} \tag{5.54}$$

The first term is in its final form, while the second term need to be changed. Move u'_j inside the last derivation, and subtract the missing term.

$$2\nu\overline{\frac{\partial u'_i}{\partial x_k}u'_j\frac{\partial^2 u'_i}{\partial x_j\partial x_k}} = 2\nu\overline{\frac{\partial u'_i}{\partial x_k}\frac{\partial}{\partial x_k}\left(u'_j\frac{\partial u'_i}{\partial x_j}\right)} - 2\nu\overline{\frac{\partial u'_i}{\partial x_k}\frac{\partial u'_i}{\partial x_k}\underbrace{\frac{\partial u'_j}{\partial x_j}}_{=0}} \tag{5.55}$$

where the the last term is zero due to the incompressible form of the continuity equation. The term must still be changed. This is done in reverse. Starting with the final version and then checking whether this is a correct form:

$$\nu\overline{\frac{\partial}{\partial x_j}\left(u'_j\frac{\partial u'_i}{\partial x_k}\frac{\partial u'_i}{\partial x_k}\right)} = \nu\underbrace{\overline{\frac{\partial u'_j}{\partial x_j}}}_{=0}\overline{\frac{\partial u'_i}{\partial x_k}\frac{\partial u'_i}{\partial x_k}} + 2\nu\overline{\frac{\partial u_i}{\partial x_j}\frac{\partial}{\partial x_j}\left(u'_j\frac{\partial u'_i}{\partial x_k}\right)} \tag{5.56}$$

The resulting term (LHS) can be rewritten with the definition of the dissipation to give:

$$\nu\overline{\frac{\partial}{\partial x_j}\left(u'_j\frac{\partial u'_i}{\partial x_k}\frac{\partial u'_i}{\partial x_k}\right)} = \frac{\partial}{\partial x_j}\left(\overline{u'_j\varepsilon'}\right) \tag{5.57}$$

where

$$\varepsilon' = \nu\frac{\partial u'_i}{\partial x_k}\frac{\partial u'_i}{\partial x_k} \tag{5.58}$$

Collecting the terms from the third convective term gives:

$$2\nu\overline{\frac{\partial u'_i}{\partial x_k}\frac{\partial}{\partial x_k}\left(u'_j\frac{\partial u'_i}{\partial x_j}\right)} = 2\nu\overline{\frac{\partial u'_i}{\partial x_k}\frac{\partial u'_j}{\partial x_k}\frac{\partial u'_i}{\partial x_j}} + \nu\frac{\partial}{\partial x_j}\left(\overline{u'_j\frac{\partial u'_i}{\partial x_k}\frac{\partial u'_i}{\partial x_k}}\right) \tag{5.59}$$

These are the turbulent production and turbulent transport terms.

5.6.3 Body Force Term

The only body force that survives the manipulation of the above is the Coriolis force:

$$4\nu\overline{\frac{\partial u'_i}{\partial x_k}\frac{\partial}{\partial x_k}\left(\epsilon_{imn}\Omega_m u'_n\right)} \tag{5.60}$$

There is no simple rewriting of this term.

5.6.4 Pressure Term

Applying the operands on the pressure term gives:

$$2\nu\overline{\frac{\partial u'_i}{\partial x_k}\frac{\partial}{\partial x_k}\left(\frac{1}{\rho}\frac{\partial p'}{\partial x_i}\right)} \tag{5.61}$$

Start with the derivation:

$$= 2\frac{\nu}{\rho}\overline{\frac{\partial u'_i}{\partial x_k}\frac{\partial^2 p'}{\partial x_k\partial x_i}} \tag{5.62}$$

Changing the derivation order for the pressure and moving the spatial-derivative of the velocity, u_i', inside the derivation with respect to x_i and then subtracting the product term gives:

$$= 2\frac{\nu}{\rho}\frac{\partial}{\partial x_i}\left(\overline{\frac{\partial u_i'}{\partial x_k}\frac{\partial p'}{\partial x_k}}\right) - 2\frac{\nu}{\rho}\overline{\underbrace{\frac{\partial^2 u_i}{\partial x_i \partial x_k}}_{=0}\frac{\partial p'}{\partial x_k}} \tag{5.63}$$

By changing the derivation order and assuming incompressible flow, the last term is zero.

5.6.5 Viscous Term

The viscous term is:

$$2\nu\overline{\frac{\partial u_i'}{\partial x_k}\frac{\partial}{\partial x_k}\left(\nu\frac{\partial^2 u_i'}{\partial x_j \partial x_j}\right)} \tag{5.64}$$

Start by moving one of the derivations of the double derivation of u_i' outside the parenthesis:

$$= 2\nu^2\overline{\frac{\partial u_i'}{\partial x_k}\frac{\partial^2}{\partial x_k \partial x_j}\left(\frac{\partial u_i'}{\partial x_j}\right)} \tag{5.65}$$

Now the first u_i' is moved inside the derivation, and something must thus be deducted. This is most simply done when the answer is known and can be backtracked:

$$= \nu^2\frac{\partial^2}{\partial x_k \partial x_k}\left(\overline{\frac{\partial u_i'}{\partial x_m}\frac{\partial u_i'}{\partial x_m}}\right) - 2\nu^2\overline{\frac{\partial^2 u_i'}{\partial x_k \partial x_m}\frac{\partial^2 u_i'}{\partial x_k \partial x_m}} \tag{5.66}$$

Check the above operation:

$$\begin{aligned}\nu^2\frac{\partial^2}{\partial x_k \partial x_k}\left(\overline{\frac{\partial u_i'}{\partial x_m}\frac{\partial u_i'}{\partial x_m}}\right) &= \nu^2\frac{\partial}{\partial x_k}\left(\overline{\frac{\partial^2 u_i'}{\partial x_k \partial x_m}\frac{\partial u_i'}{\partial x_m} + \frac{\partial u_i'}{\partial x_m}\frac{\partial^2 u_i'}{\partial x_k \partial x_m}}\right) = \\ 2\nu^2\frac{\partial}{\partial x_k}\left(\overline{\frac{\partial u_i'}{\partial x_m}\frac{\partial^2 u_i'}{\partial x_k \partial x_m}}\right) &= 2\nu^2\overline{\frac{\partial^2 u_i'}{\partial x_k \partial x_m}\frac{\partial^2 u_i'}{\partial x_k \partial x_m}} + 2\nu^2\overline{\frac{\partial u_i'}{\partial x_m}\frac{\partial}{\partial x_k}\left(\frac{\partial^2 u_i'}{\partial x_k \partial x_m}\right)}\end{aligned} \tag{5.67}$$

Substituting the above equation into Eq. 5.66 gives Eq. 5.65.
The second term of Eq. 5.66 is now at its final version, whereas the first term of Eq. 5.66 needs to be rewritten with ε:

$$\frac{\partial}{\partial x_k}\left(\nu\frac{\partial}{\partial x_k}\left(\nu\overline{\frac{\partial u_i'}{\partial x_m}\frac{\partial u_i'}{\partial x_m}}\right)\right) = \frac{\partial}{\partial x_k}\left(\nu\frac{\partial \varepsilon}{\partial x_k}\right) \tag{5.68}$$

Summing up the viscous terms:

$$2\nu\overline{\frac{\partial u_i'}{\partial x_k}\frac{\partial}{\partial x_k}\left(\nu\frac{\partial^2 u_i'}{\partial x_k \partial x_k}\right)} = \frac{\partial}{\partial x_k}\left(\nu\frac{\partial \varepsilon}{\partial x_k}\right) - 2\overline{\left(\nu\frac{\partial^2 u_i'}{\partial x_k \partial x_m}\right)^2} \tag{5.69}$$

5.6.6 Dissipation Rate Equation

Adding the above together yields the transport equation for the dissipation rate:

$$\frac{D\varepsilon}{Dt} = P_\varepsilon^1 + P_\varepsilon^2 + P_\varepsilon^3 + P_\varepsilon^4 + G_\varepsilon + T_\varepsilon + \Pi_\varepsilon + D_\varepsilon^\nu - D_\varepsilon \tag{5.70}$$

with the following denotation and exact form:

$$P_\varepsilon^1 = -2\nu\overline{\frac{\partial u_i'}{\partial x_k}\frac{\partial u_j'}{\partial x_k}}\frac{\partial U_i}{\partial x_j} \qquad \text{Mixed production}$$

$$P_\varepsilon^2 = -2\nu\overline{\frac{\partial u_i'}{\partial x_k}\frac{\partial u_i'}{\partial x_j}}\frac{\partial U_j}{\partial x_k} \qquad \text{Production by mean velocity gradient}$$

$$P_\varepsilon^3 = -2\nu\overline{u_j'\frac{\partial u_i'}{\partial x_k}}\frac{\partial^2 U_i}{\partial x_j \partial x_k} \qquad \text{Gradient production}$$

$$P_\varepsilon^4 = -2\nu\overline{\frac{\partial u_i'}{\partial x_k}\frac{\partial u_j'}{\partial x_k}\frac{\partial u_i'}{\partial x_j}} \qquad \text{Turbulent production}$$

$$G_\varepsilon = 4\nu\overline{\frac{\partial u_i'}{\partial x_k}\frac{\partial}{\partial x_k}\left(\epsilon_{imn}\Omega_m u_n'\right)} \qquad \text{Production by rotation}$$

$$T_\varepsilon = -\nu\frac{\partial}{\partial x_j}\left(\overline{u_j'\varepsilon}\right) \qquad \text{Turbulent transport}$$

$$\Pi_\varepsilon = -2\frac{\nu}{\rho}\frac{\partial}{\partial x_i}\left(\overline{\frac{\partial u_i'}{\partial x_k}\frac{\partial p'}{\partial x_k}}\right) \qquad \text{Pressure transport}$$

$$D_\varepsilon^\nu = \nu\frac{\partial^2 \varepsilon}{\partial x_k \partial x_k} \qquad \text{Viscous diffusion}$$

$$D_\varepsilon = 2\overline{\left(\nu\frac{\partial^2 u_i'}{\partial x_k \partial x_m}\right)^2} \qquad \text{Dissipation}$$

5.7 Reynolds Average Vorticity Equation

In a similar way as for the Navier-Stokes equation, the vorticity equation can be transformed into a turbulent vorticity equation by means of a decomposition of the variables into a mean and fluctuating quantity. For the vorticity, the mean vorticity and the fluctuating vorticity are defined as:

$$\omega_i = \overline{\omega}_i + \omega_i' \tag{5.71}$$

Inserting this identity[12] and the velocity decomposition into the mean vorticity, Eq. 4.41, and then time-averaging yields:

$$\rho\frac{\partial \omega_i}{\partial t} + \rho u_j\frac{\partial \omega_i}{\partial x_j} + \overline{\rho u_j'\frac{\partial \omega_i'}{\partial x_j}} + 2\rho u_j\frac{\partial \Omega_i}{\partial x_j} = \rho\omega_j\frac{\partial u_i}{\partial x_j} + \overline{\rho\omega_j'\frac{\partial u_i'}{\partial x_j}} + 2\rho\Omega_j\frac{\partial u_i}{\partial x_j} + \mu\frac{\partial^2 \omega_i}{\partial x_j^2} \tag{5.72}$$

Note that the solid body rotation, Ω_i, is assumed to be constant and does not possess any fluctuating term. Both the fluctuating and mean vorticity are solenoidal (i.e. divergenceless) [52]:

$$\frac{\partial \omega_i}{\partial x_i} = \frac{\partial \omega_i'}{\partial x_i} = 0 \tag{5.73}$$

[12] Dropping the overbar for the mean component.

Using this in the turbulent vorticity equation, the turbulent terms can be reformulated:

$$\rho\frac{\partial\omega_i}{\partial t}+\rho u_j\frac{\partial\omega_i}{\partial x_j}+2\rho u_j\frac{\partial\Omega_i}{\partial x_j}=\rho\omega_j\frac{\partial u_i}{\partial x_j}+2\rho\Omega_j\frac{\partial u_i}{\partial x_j}+\rho\frac{\partial\overline{\omega_j'u_i'}}{\partial x_j}-\rho\frac{\partial\overline{u_j'\omega_i'}}{\partial x_j}+\mu\frac{\partial^2\omega_i}{\partial x_j^2} \quad (5.74)$$

The term $\overline{u_j'\omega_i'}$ is a transport term, while $\overline{\omega_j'u_i'}$ is a production term of vorticity caused by stretching and rotation of the fluid elements.

6 Turbulence Models

The above exact transport equations for the relevant properties include a number of unknowns. The goal of turbulence modeling is to model these unknowns in terms of known properties in a physically realistic way.

6.1 Boussinesq Hypothesis vs Second-Moment Closures

Reynolds averaging yielded a new unknown, the Reynolds stress tensor, $R_{ij} = \overline{u_i' u_j'}$, which in fact, as it is a symmetric two-rank tensor, consists of six unknowns. This tensor has been the fundamental problem in turbulence modeling, from its start by Boussinesq. He proposed, in 1877 a model for these Reynolds stresses even before Reynolds himself derived them in 1895. The assumption made by Boussinesq [4] was to introduce the concept of a 'turbulent' viscosity in such way that the Reynolds stress would be equal to a scalar times a gradient. The *Boussinesq hypothesis* is thus:

$$R_{ij} = \overline{u_i' u_j'} = \frac{2}{3} k \delta_{ij} - \nu_t \left(\frac{\partial U_i}{\partial x_j} + \frac{\partial U_j}{\partial x_i} \right) = \frac{2}{3} k \delta_{ij} - 2 \nu_t S_{ij} \tag{6.1}$$

The terms within parentheses are equal to two times the strain-rate tensor, S_{ij}, and the coefficient, ν_t, is denoted the turbulent viscosity or eddy viscosity. The $2/3$ is added to make the relation invariant. The eddy viscosity was devised as a constant value by Boussinesq, which however can only be expected if the turbulent field is at least *homogeneous*. In more elaborated eddy viscosity models (EVMs) the turbulent viscosity is allowed to vary depending on some turbulent property. However, the underlying assumption about homogeneous flow can not be regarded as a general fluid flow case.

In second-moment closure models, the Reynolds stresses are not simplified and each of the six stresses is solved with its own transport equation, as done in Reynolds Stress Models (RSMs). A number of terms in these equations are then modeled, hence the denotation second-moment closure models. The RSM are thus a more physical model than the EVMs based on the Boussinesq hypothesis, although the RSMs are generally plagued by being numerically stiffer and more prone to non-convergent solutions.

6.2 Algebraic Models

A model based on the Boussinesq hypothesis using an algebraic relation to compute the turbulent viscosity, μ_t, is called an algebraic equation model. Fifty years after Boussinesq, Prandtl put forward the *mixing length hypothesis*, which is based on the local velocity gradients, to model the turbulent viscosity:

$$\nu_t = l_m^2 \frac{\partial U}{\partial y} \tag{6.2}$$

where l_m is the mixing-length and has been found to be a linear relation close to solid boundaries. The relation coefficient is the von Kármán coefficient, κ:

$$l_m = \kappa y \tag{6.3}$$

where κ has a value of around 0.42.
Despite its limited physical characteristics, a number of similar models, notably the

Cebeci-Smith model (1967) and Baldwin-Lomax model (1978), see Wilcox [58], have later been used in the aircraft industry.

The main problems with the mixing-length or algebraic equations are their locality description of the turbulent viscosity, ν_t. Any non-locality in the eddy viscosity models (EVMs) must enter through the use of a transport equation for a relevant velocity and/or length scale. The basic ideas of such one- or two-equation models were initiated in the 1940s, by Prandtl (1945) [45], Kolmogorov (1942) [30] and Chou (1945) [8].

6.3 One-Equation Models

The natural velocity scale for eddy viscosity is the square root of the kinetic energy:

$$u = k^{1/2} = \sqrt{\frac{1}{2}u_i u_i} \tag{6.4}$$

With this quantity, in 1945 Prandtl introduce non-locality in the description of the eddy viscosity:

$$\nu_t = k^{1/2} l \tag{6.5}$$

A length scale is however needed in this model, which is its main drawback. The relevant length scale must be taken through empirical arguments, and changed according to the flowfield. This shortcoming, shared with the zero-equations, has set serious limitations to the usefulness of these models. A new approach by Spalart-Allmaras (1992), see e.g. Wilcox [58], uses a transport model for the turbulent viscosity itself, instead of the k-equation. This is an interesting idea, although the transport effects, which have been proven to be necessary for a physically valid model, can not be modeled with this model.

6.4 Two-Equation Models

The main drawback of the zero- and one-equation models is the need of *a priori* knowledge, to estimate the correct length scale. In two-equation models, this is solved by introducing an additional transport equation for the length scale or some other turbulent quantity. This has proven to be a reasonable approach to yield generality in engineering predictions in a large variety of flows. Thus a number of two-equation turbulence models have been developed, starting with Kolmogorov in 1942. He based the $k-\omega$ model on the kinetic energy, k, and the transport equation for the specific dissipation, ω, which has the dimension s^{-1}, i.e. inverse to time. However the most popular two-equation model is that based on the transport equation for the dissipation, ε, in addition to the k equation, i.e. the $k-\varepsilon$ model developed by Chou in 1945. There also exist models based on the length scale itself, l, and time scale, τ, although they are not as common. In this report, only two-equation EVMs based on the either the dissipation, ε-equation, or the specific dissipation, ω-equation, are used.

6.4.1 $k-\varepsilon$ Model, Abid *et al.*

The $k-\varepsilon$ equation of Abid *et al.* [2] is a low-Reynolds number two-equation EVM based on similar grounds as the standard $k-\varepsilon$ of Jones and Launder [27] with only some slight differences in the closure constants and boundary conditions.

The modeled transport equations for the turbulent kinetics energy, k, and dissipation rate equation, ε, in this model are:

$$\frac{Dk}{Dt} = P_k - \varepsilon + \frac{\partial}{\partial x_j}\left[\left(\nu + \frac{\nu_t}{\sigma_k}\right)\frac{\partial k}{\partial x_j}\right] \tag{6.6}$$

and

$$\frac{D\varepsilon}{Dt} = C_{\varepsilon 1}\frac{\varepsilon}{k}P_k - C_{\varepsilon 2}f\frac{\varepsilon^2}{k} + \frac{\partial}{\partial x_j}\left[\left(\nu + \frac{\nu_t}{\sigma_\varepsilon}\right)\frac{\partial \varepsilon}{\partial x_j}\right] \tag{6.7}$$

where $P_k = 2\nu_t S_{ij} S_{ij}$ is the turbulent production of k, using the Boussinesq hypothesis, Eq. 6.1, with the turbulent viscosity defined as:

$$\nu_t = C_\mu \frac{k^2}{\varepsilon} \tag{6.8}$$

The constant $C_\mu = 0.088$ was given a slightly lower value than the standard value $= 0.09$. The closure coefficients are:

$$\sigma_k = 1.0, \qquad \sigma_\varepsilon = 1.3, \qquad C_{\varepsilon 1} = 1.39, \qquad C_{\varepsilon 2} = 1.83 \tag{6.9}$$

A damping factor, f, was introduced to remove the singularity of the dissipation equation at the wall and was given the value:

$$f = 1 - \exp\left(-\frac{R_y}{12.5}\right), \qquad R_y = \frac{\sqrt{k}y}{\nu} \tag{6.10}$$

The boundary conditions for the k and ε equation are:

$$k = 0, \qquad \varepsilon = 2\nu\left(\frac{\partial\sqrt{k}}{\partial y}\right)^2 \tag{6.11}$$

6.4.2 Two-layer $k-\varepsilon$ Model, Chen and Patel

The two-layer, or zonal $k-\varepsilon$ model of Chen and Patel [7] uses two different approaches to compute the eddy viscosity, one in the main flow, or high-Reynolds number (HRN) flow, and another in the near wall region, or the low-Reynolds number (LRN) flow. The matching line between the two regions is set at $y^+ \approx 50$, where $y^+ = yu_\tau/\nu$.
The HRN model is the standard $k-\varepsilon$ model, with k modeled as:

$$\frac{Dk}{Dt} = P_k - \varepsilon + \frac{\partial}{\partial x_j}\left[\left(\nu + \frac{\nu_t}{\sigma_k}\right)\frac{\partial k}{\partial x_j}\right] \tag{6.12}$$

and ε as:

$$\frac{D\varepsilon}{Dt} = C_{\varepsilon 1}\frac{k}{\varepsilon}P_k - C_{\varepsilon 2}\frac{\varepsilon^2}{k} + \frac{\partial}{\partial x_j}\left[\left(\nu + \frac{\nu_t}{\sigma_\varepsilon}\right)\frac{\partial k}{\partial x_j}\right] \tag{6.13}$$

The eddy viscosity, which is used in the Boussinesq equation, Eq. 6.1, is formulated as:

$$\nu_t = C_\mu \frac{k^2}{\varepsilon} \tag{6.14}$$

The above HRN model is then combined with the LRN model close to the walls. This model is the one-equation model by Wolfshtein [60]. The latter, unlike the LRN $k-\varepsilon$ models, requires only the solution of one transport equation, the turbulent kinetic energy. In the Wolfshtein model, the dissipation rate is set with the aid of a turbulent length scale:

$$\begin{aligned} \varepsilon &= \frac{k^{3/2}}{l_\varepsilon} \\ l_\varepsilon &= C_l y(1-\exp(-R_y/A_\varepsilon)) \end{aligned} \tag{6.15}$$

where $R_y = \sqrt{k}y/\nu$. The eddy viscosity is set as:

$$\begin{aligned} \nu_t &= C_\mu \sqrt{k} l_\mu \\ l_\mu &= C_l y(1-\exp(-R_y/A_\mu)) \end{aligned} \tag{6.16}$$

This concept removes the problematic boundary condition for the dissipation rate, with the turbulent length scale being a simple relation of the wall distance.
The closure coefficients involved are:

$$\begin{aligned} C_\mu = 0.09, \qquad C_{\varepsilon 1} = 1.44, \qquad C_{\varepsilon 2} = 1.92, \qquad \sigma_k = 1 \qquad \kappa = 0.435 \\ \sigma_\varepsilon = \kappa^2/(C_{\varepsilon 2} - C_{\varepsilon 1}/\sqrt{(C_\mu)}, \qquad A_\varepsilon = 2C_l, \qquad A_\mu = 70, \qquad C_l = \kappa C_\mu^{-3/4} \end{aligned} \tag{6.17}$$

6.4.3 $k-\omega$ Model, Abid *et al.*

The $k-\omega$ equation by Abid *et al.* [2] is based on the standard $k-\omega$ model by Wilcox [56]. The main difference between the models is the definition of the specific dissipation. Abid *et al.* use the true ω in the sense that it is the dissipation divided by the turbulent kinetic energy, $\omega \equiv \varepsilon/k$ while Wilcox includes a closure coefficient in the definition, $\omega \equiv \varepsilon/\beta^* k$. This change in definition makes the closure coefficients different. Otherwise the two models are essential equal. Note also that this definition does not affect the predicted ν_t. One important characteristic of the standard $k-\omega$ model is that it can be integrated to the wall without any damping function, and thus there is no need of any errornous wall functions.

The modeled transport equations for the turbulent kinetics energy, k, and the specific dissipation rate equation, ω, in the Abid *et al.* model are:

$$\frac{Dk}{Dt} = P_k - \omega k + \frac{\partial}{\partial x_j}\left[\left(\nu + \frac{\nu_t}{\sigma_k}\right)\frac{\partial k}{\partial x_j}\right] \tag{6.18}$$

and

$$\frac{D\omega}{Dt} = C_{\omega 1}\frac{\omega}{k}P_k - C_{\omega 2}\omega^2 + \frac{\partial}{\partial x_j}\left[\left(\nu + \frac{\nu_t}{\sigma_\omega}\right)\frac{\partial \omega}{\partial x_j}\right] \tag{6.19}$$

with the turbulent viscosity defined as:

$$\nu_t = C_\mu \frac{k}{\omega} \tag{6.20}$$

The closure coefficients are:

$$\sigma_k = 1.4, \qquad \sigma_\omega = 2.0, \qquad C_{\omega 1} = 0.55, \qquad C_{\omega 2} = 0.83 \tag{6.21}$$

The boundary conditions for the k and ω equation are:

$$k = 0, \qquad \omega = 10\frac{6\nu}{C_{\omega 2} y^2} \tag{6.22}$$

6.4.4 $k-\omega$ Model, Peng *et al.*

The $k-\omega$ model by Peng *et al.* [43] is similar to the LRN Wilcox [57], however with a cross-diffusion term added in the ω equation. Furthermore, the coefficients and the wall-damping functions are re-tuned. The turbulent kinetic energy equation:

$$\begin{aligned} \frac{Dk}{Dt} &= P_k - c_k f_k \omega k + \frac{\partial}{\partial x_j}\left[\left(\nu + \frac{\nu_t}{\sigma_k}\right)\frac{\partial k}{\partial x_j}\right] \\ f_k &= 1 - 0.722\exp\left[-\left(\frac{R_t}{10}\right)^4\right] \end{aligned} \tag{6.23}$$

and the specific dissipation rate equation:

$$\begin{aligned} \frac{D\omega}{Dt} &= C_{\omega 1} f_\omega \frac{\omega}{k} P_k - C_{\omega 2}\omega^2 + \frac{\partial}{\partial x_j}\left[\left(\nu + \frac{\nu_t}{\sigma_\omega}\right)\frac{\partial \omega}{\partial x_j}\right] + C_\omega \frac{\nu_t}{k}\left(\frac{\partial k}{\partial x_j}\frac{\partial \omega}{\partial x_j}\right) \\ f_\omega &= 1 + 4.3\exp\left[-\left(\frac{R_t}{1.5}\right)^{1/2}\right] \end{aligned} \tag{6.24}$$

where $R_t = k/\omega\nu$.
The cross diffusion term, $\partial k/\partial x_j \partial\omega/\partial x_j$, in the ω equation appears when the ε equation is transformed to the ω equation. Its effect is to enhance the predictions in the outer region of the boundary layer where the standard $k-\omega$ has difficulties, [37]. The eddy viscosity in the Peng *et al.* $k-\omega$ model is set as:

$$\begin{aligned} \nu_t &= C_\mu f_\mu \frac{k}{\omega} \\ f_\mu &= 0.025 + \left[1 - \exp\left\{-\left(\frac{R_t}{10}\right)^{3/4}\right\}\right]\left[0.975 + \frac{0.001}{R_t}\exp\left\{-\left(\frac{R_t}{200}\right)^2\right\}\right] \end{aligned} \tag{6.25}$$

The boundary conditions for the turbulent kinetic energy and the specific dissipation rate are:

$$k = 0, \qquad \omega = \frac{6\nu}{C_{\omega 2} y^2} \tag{6.26}$$

The constants in this model are:

$$\begin{aligned} &C_\mu = 1.0, \quad C_k = 0.09, \quad \sigma_\omega = 1.35, \quad \sigma_k = 0.8 \quad C_\omega = 0.75 \\ &C_{\omega 1} = 0.42, \quad C_{\omega 2} = 0.075 \end{aligned} \tag{6.27}$$

6.5 RSM, Reynolds Stress Models

According to the discussion on second-moment closures and models based on the Boussinesq hypothesis, the RSM is a more physically correct model. This is primarily due to the exact representation of the Reynolds stress through their own transport models. With knowledge of the Reynolds stresses, the production term can be described exactly, as can the body generation term, which is of great advantage when predicting rotating fluids. However, even with a second-moment closure model, there must be some modeling. This is noted below. A symbolic description of the Reynolds stress transport equation is:

$$\frac{DR_{ij}}{Dt} = P_{ij} + G_{ij} + \Pi_{ij} - \varepsilon_{ij} + \frac{\partial D_{ij}}{\partial x_k} + \frac{\partial D^\nu_{ij}}{\partial x_k} \tag{6.28}$$

where the terms are either exact or modeled according to:

$$
\begin{aligned}
P_{ij} &= -\left(\overline{u_i'u_k'}\frac{\partial U_j}{\partial x_k} + \overline{u_j'u_k'}\frac{\partial U_i}{\partial x_k}\right) && \text{(exact)}\\
G_{ij} &= -2\Omega_k\left(\epsilon_{jkl}\overline{u_i'u_l'} + \epsilon_{ikl}\overline{u_j'u_l'}\right) && \text{(exact)}\\
\Pi_{ij} &= \overline{\frac{p'}{\rho}\left(\frac{\partial u_j'}{\partial x_i} + \frac{\partial u_i'}{\partial x_j}\right)} && \text{(modeled)}\\
\varepsilon_{ij} &= 2\nu\overline{\frac{\partial u_j'}{\partial x_k}\frac{\partial u_i'}{\partial x_k}} - \nu\frac{\partial^2\overline{u_i'u_j'}}{\partial x_k x_k} && \text{(modeled)}\\
D_{ij} &= -\left(\overline{\frac{u_i'p'}{\rho}}\delta_{jk} + \overline{\frac{u_j'p'}{\rho}}\delta_{ik} + \overline{u_k'u_i'u_j'}\right) && \text{(modeled)}\\
D_{ij}^{\nu} &= -\nu\frac{\partial\overline{u_i'u_j'}}{\partial x_k} && \text{(exact)}
\end{aligned}
$$

In a standard form – Launder-Reece-Rodi [34] formulation – the Reynolds stresses terms are modeled according to:

6.5.1 Pressure-strain Term, Π_{ij}

Generally, the pressure-strain term is composed of a slow part, $\Pi_{ij,1}$, a rapid part, $\Pi_{ij,2}$, and a wall reflection part, $\Pi_{ij,w}$. The slow part is modeled according to Rotta [49]

$$\Pi_{ij,1} = -c_1\frac{\varepsilon}{k}\left(\overline{u_i'u_j'} - \frac{2}{3}\delta_{ij}k\right) \tag{6.29}$$

The rapid part according to the Launder-Reece-Rodi (LRR[13]) [34] formulation is:

$$\Pi_{ij,2} = -\frac{c_2+8}{11}\left(P_{ij} - \frac{2}{3}P\delta_{ij}\right) - \frac{30c_2-2}{55}2kS_{ij} - \frac{8c_2-2}{11}\left(P_{ij}^* - \frac{2}{3}P\delta_{ij}\right) \tag{6.30}$$

where P_{ij}^* is defined as

$$P_{ij}^* = -\left(\overline{u_i'u_k'}\frac{\partial U_k}{\partial x_j} + \overline{u_j'u_k'}\frac{\partial U_k}{\partial x_i}\right) \tag{6.31}$$

The closure coefficient c_2 was found to be close to 0.4.
Launder *et al.* also devised a reduced form of the above rapid part, denoted 'isotropization-of-production' which is formulated as:

$$\Pi_{ij,2} = -\gamma\left(P_{ij} - \frac{2}{3}P\delta_{ij}\right) \tag{6.32}$$

with $\gamma = 0.6$.
The wall reflection part is modeled as:

$$\Pi_{ij,w} = \frac{k^{3/2}}{\varepsilon y}\left[0.125\frac{\varepsilon}{k}\left(\overline{u_i'u_j'} - \frac{2}{3}k\delta_{ij}\right) + 0.015(P_{ij} - P_{ij}^*)\right] \tag{6.33}$$

This wall reflection term was proposed in a different way by Gibson and Launder and is currently more common. The total pressure-strain term is the sum of the slow part, rapid part and wall reflection part.

[13]The Launder-Reece-Rodi pressure-strain model is commonly denoted LRR.

6.5.2 Dissipation Rate Tensor, ε_{ij}

The dissipation rate tensor is modeled according to Kolmogorov's assumption of isotropy of the small scales:

$$\varepsilon_{ij} = \frac{2}{3}\delta_{ij}\varepsilon \tag{6.34}$$

The scalar dissipation rate using the Reynolds stresses differs slightly from the EVM dissipation rate equation. According to Hanjalic and Launder [17], the RSM dissipation rate equation can be formulated as:

$$\frac{D\varepsilon}{Dt} = -c_{\varepsilon 1}\overline{u_i'u_k'}\frac{\varepsilon}{k}\frac{\partial U_i}{\partial x_k} - c_{\varepsilon 2}\frac{\varepsilon^2}{k} + \frac{\partial}{\partial x_k}\left(c_\varepsilon \frac{k}{\varepsilon}\overline{u_k'u_l'}\frac{\partial \varepsilon}{\partial x_l}\right) \tag{6.35}$$

6.5.3 Diffusive Transport Term, D_{ij}

The only part of the diffusive transport tensor that is modeled is the triple correlation, which is modeled according to Hanjalic and Launder [17]:

$$D_{ij} = -\overline{u_i'u_j'u_k'} = c_s\frac{k}{\varepsilon}\left(\overline{u_k'u_l'}\frac{\partial}{\partial x_l}\overline{u_i'u_j'} + \overline{u_i'u_l'}\frac{\partial}{\partial x_l}\overline{u_j'u_k'} + \overline{u_j'u_l'}\frac{\partial}{\partial x_l}\overline{u_k'u_i'}\right) \tag{6.36}$$

However, Launder *et al.* also used a trunked version, the GGDH [14] of Daly and Harlow [10]:

$$D_{ij} = -\overline{u_i'u_j'u_k'} = c_s'\frac{k}{\varepsilon}\left(\overline{u_k'u_l'}\frac{\partial \overline{u_i'u_j'}}{\partial x_l}\right) \tag{6.37}$$

The majority of the Reynolds Stress Models developed are similar to the above formulation, and thus this model can serve as the basis for later discussions.

6.6 ARSM, Algebraic Reynolds Stress Models

The classic Algebraic Reynolds Stress Model (ARSM) by Rodi [48] was developed from the Reynolds Stress Model, with the assumption of a relation between the convective and the diffusive terms in the Reynolds stresses with those in the equation for the turbulent kinetic energy [15]:

$$\begin{aligned} \text{Transport of } \overline{u_i'u_j'} &\approx \frac{\overline{u_i'u_j'}}{k} \cdot \text{transport of } k \\ \frac{D\overline{u_i'u_j'}}{Dt} - \frac{\partial(D_{ij}+D_{ij}^\nu)}{\partial x_k} &= \frac{\overline{u_i'u_j'}}{k}\left(\frac{Dk}{Dt} - \frac{\partial(D_j+D_j^\nu)}{\partial x_j}\right) \end{aligned} \tag{6.38}$$

Simply this substitution would not be very valuable since the convective and diffusive terms in the k equation (the RHS of above) are as difficult to model as the convective and diffusive terms in the full Reynolds stress equation (the LHS above). However, by using

[14] GGDH=Generalized Gradient Diffusion Hypothesis.

[15] See Eq's. 5.36 and 5.39 for an explanation of the individual terms.

the identity of the k equation, Eq. 5.39, for the RHS and the Reynolds stress equation, Eq. 5.36, for the LHS, the equation can be changed to:

$$P_{ij} + G_{ij} + \Pi_{ij} - \varepsilon_{ij} = \frac{\overline{u_i' u_j'}}{k} (P_k - \varepsilon) \tag{6.39}$$

which is the hypothesis used by Rodi, where the production terms, P_{ij} and P_k and G_{ij} are exact while the rest must be modeled. Note that, in the ARSM formulation, an equation for the turbulent kinetic energy is needed in addition to the Reynolds stress equation and the dissipation rate equation. The k equation differs somewhat from the eddy viscosity-based models, since the Reynolds stresses are known:

$$\frac{Dk}{Dt} = P_k - \varepsilon + \frac{\partial}{\partial x_k} \left[\left(\nu + c_k \frac{k}{\varepsilon} \overline{u_k' u_l'} \right) \frac{\partial k}{\partial x_l} \right] \tag{6.40}$$

with the production term in its exact form as:

$$P_k = -\overline{u_k' u_l'} \frac{\partial U_k}{\partial x_l} \tag{6.41}$$

The dissipation rate equation, the pressure-strain term and the dissipation rate term are modeled in a similar fashion as for the Reynolds stress model.

6.7 EARSM, Explicit Algebraic Reynolds Stress Models

The implicit relation for the Reynolds stresses above has been found to be numerically and computationally cumbersome, since there are no diffusion or damping terms present. The basis of the EARSM follows the same ideas as in the ARSM, as postulated by Rodi; the transport of Reynolds stresses is set equal to the normalized transport of kinetic energy. However, in the explicit ARSM (EARSM), the Reynolds stresses are explicitly related to the mean flow field, see Eq. 6.51. This makes the model more robust and reduces the computational complexity level to that of a $k - \varepsilon$ model. Normally, the anisotropy tensor is used instead of the Reynolds stresses in the turbulent transport equation. The anisotropy tensor is defined as:

$$a_{ij} \equiv \frac{\overline{u_i' u_j'}}{k} - \frac{2}{3} \delta_{ij} \tag{6.42}$$

Start by substituting the production term, P_{ij}, in equation 6.39 with the help of the anisotropy tensor:

$$\begin{aligned} P_{ij} &= -\overline{u_i' u_k'} \frac{\partial U_j}{\partial x_k} - \overline{u_j' u_k'} \frac{\partial U_i}{\partial x_k} = \\ -k \left(a_{ik} + \frac{2}{3} \delta_{ik} \right) (S_{jk} + \Omega_{jk}) &- k \left(a_{jk} + \frac{2}{3} \delta_{jk} \right) (S_{ik} + \Omega_{ik}) = \\ -k \left(a_{ik} S_{jk} + a_{jk} S_{ik} + a_{ik} \Omega_{jk} + a_{jk} \Omega_{ik} \right) &- \frac{4}{3} k S_{ij} \end{aligned} \tag{6.43}$$

This may need some explanation. The mean velocity gradients, $\partial U_j / \partial x_k$ and $\partial U_i / \partial x_k$, are rewritten with the rotational tensor, Ω_{ij}, and the strain-rate tensor, S_{ij}, defined as:

$$S_{ij} = \frac{1}{2} \left(\frac{\partial U_i}{\partial x_j} + \frac{\partial U_j}{\partial x_i} \right) \tag{6.44}$$

$$\Omega_{ij} = \frac{1}{2} \left(\frac{\partial U_i}{\partial x_j} - \frac{\partial U_j}{\partial x_i} \right) \tag{6.45}$$

Adding them together obviously cancels the right side of the terms.
Furthermore, the terms including the Kronecker delta, δ_{ij}, multiplied by the rotational tensor disappear:

$$-k\frac{2}{3}\delta_{ik}\Omega_{jk} - k\frac{2}{3}\delta_{jk}\Omega_{ik} = -k\frac{2}{3}\left(\Omega_{ij} + \Omega_{ji}\right) \equiv 0 \tag{6.46}$$

The last identity is due to the anti-symmetry of the rotational tensor.
The next term to be reformulated is the RHS of Eq. 6.39:

$$\frac{\overline{u_i' u_j'}}{k}\left(P_k - \varepsilon\right) = \left(a_{ij} + \frac{2}{3}\delta_{ij}\right)\left(P_k - \varepsilon\right) \tag{6.47}$$

The Kronecker delta multiplied by the scalar dissipation rate is equal to the tensor dissipation rate, see Eq. 6.34, while the turbulent kinetic energy production, P_k, is twice the trace of the Reynolds stress production, P_{ij}, see the above result, Eq. 6.43[16]:

$$\begin{aligned} \varepsilon\frac{2}{3}\delta_{ij} &= \varepsilon_{ij} \\ P_k\frac{2}{3}\delta_{ij} &= -k a_{mn} S_{mn}\frac{2}{3}\delta_{ij} \end{aligned} \tag{6.48}$$

and hence the RHS can be changed to:

$$\frac{\overline{u_i' u_j'}}{k}\left(P_k - \varepsilon\right) = \left(P_k - \varepsilon\right) a_{ij} - \varepsilon_{ij} - k a_{mn} S_{mn}\frac{2}{3}\delta_{ij} \tag{6.49}$$

Inserting the above relation and Eq. 6.43 into Eq. 6.39 yields:

$$\begin{aligned} \left(P_k - \varepsilon\right) a_{ij} = -\frac{4}{3}kS_{ij} - k\left(a_{ik}S_{jk} + a_{jk}S_{ik} - a_{mn}S_{mn}\frac{2}{3}\delta_{ij}\right) \\ -k\left(a_{ik}\Omega_{jk} + a_{jk}\Omega_{ik}\right) + \Pi_{ij} + G_{ij} \end{aligned} \tag{6.50}$$

By applying some model for the pressure-strain term and the dissipation rate, defined in the anisotropy tensor, the governing equation can be written in terms of the strain rate tensor, S_{ij}, rotation rate tensor, Ω_{ij}, and the anisotropy tensor, a_{ij}. The strain rate and rotation tensor can be described from mean velocity gradients and are thus known. What is left is the anisotropy tensor. This also needs to be modeled in some known parameters, hence the denotation *explicit* ARSM. The most general form of the anisotropy tensor can be described with ten tensorially independent groups expressed in S_{ij} and Ω_{ij}, where all higher-order terms can be reduced with the aid of the Caley-Hamilton theorem:

$$\begin{aligned} \mathbf{a} = \beta_1\mathbf{S} + \beta_2\left(\mathbf{S}^2 - \frac{1}{3}II_S\mathbf{I}\right) + \beta_3\left(\Omega^2 - \frac{1}{3}II_\Omega\mathbf{I}\right) + \beta_4(\mathbf{S}\Omega - \Omega\mathbf{S}) + \\ \beta_5(\mathbf{S}^2\Omega - \Omega\mathbf{S}) + \beta_6\left(\mathbf{S}\Omega^2 + \Omega^2\mathbf{S} - \frac{2}{3}IV\mathbf{I}\right) + \beta_7\left(\mathbf{S}^2\Omega^2 + \Omega^2\mathbf{S}^2 - \frac{2}{3}V\mathbf{I}\right) \\ \beta_8(\mathbf{S}\Omega\mathbf{S}^2 - \mathbf{S}\Omega\mathbf{S}) + \beta_9(\Omega\mathbf{S}\Omega^2 - \Omega^2\mathbf{S}\Omega) + \beta_{10}(\Omega\mathbf{S}\Omega^2 - \Omega^2\mathbf{S}^2\Omega) \end{aligned} \tag{6.51}$$

[16]The trace of the strain-rate tensor, S_{ii}, is zero with the help of the continuity equation and assuming incompressible flow. The product $a_{ik}\Omega_{ik}$ is zero since the anisotropy tensor is symmetric and the rotational tensor is anti-symmetric.

where coefficients β_* is a function of the invariants of $\mathbf{S}$ and Ω, which can be written as:

$$II_S = tr(\mathbf{S}^2) \equiv S_{km}S_{mk}, \qquad II_\Omega = tr(\Omega^2) \equiv \Omega_{km}\Omega_{mk}, \qquad III_S = tr(\mathbf{S}^3) \equiv S_{km}S_{mn}S_{nk}$$
$$IV = tr(\mathbf{S}\Omega^2) \equiv S_{km}\Omega_{mn}\Omega_{nk}, \qquad V = tr(\mathbf{S}^2\Omega^2) \equiv S_{km}S_{mn}\Omega_{np}\Omega_{pk} \tag{6.52}$$

$\mathbf{a}, \mathbf{S}, \Omega$ are contracted notation of the tensors $a_{ij}, S_{ij}, \Omega_{ij}$, and $\mathbf{I}$ is the identity matrix. Eq. 6.50, described in the mean velocity gradients, using the anisotropy relation, Eq. 6.51, together with the transport equations for the turbulent kinetic energy and the dissipation rate, constitutes an EARSM.

6.7.1 Gatski and Speziale

In the EARSM by Gatski and Speziale [13], the explicit relation for the Reynolds stresses is given as:

$$\overline{u_i u_j} = \frac{2}{3}k\delta_{ij} - 2C_\mu^* k \left[\left(S_{ij}^* - \frac{1}{3}S_{kk}^*\delta_{ij} \right) + \left(S_{ik}^*\Omega_{kj}^* + S_{jk}^*\Omega_{ki}^* \right) - 2\left(S_{ik}^*S_{kj}^* - \frac{1}{3}S_{kl}^*S_{kl}^*\delta_{ij} \right) \right] \tag{6.53}$$

In the above, the strain rate tensor, S_{ij}, and rotational rate tensor, Ω_{ij}, are non-dimensionalized and normalized according to:

$$S_{ij}^* = \frac{1}{2}g\tau(2 - C_3)S_{ij}$$
$$\Omega_{ij}^* = \frac{1}{2}g\tau(2 - C_4)\left[\Omega_{ij} + \left(\frac{C_4 - 4}{C_4 - 2} \right) \epsilon_{mji}\Omega_m \right] \tag{6.54}$$

where τ is the turbulent timescale. g is a function of the production-to-dissipation rate according to:

$$g = \left(\frac{1}{2}C_1 + \frac{P_k}{\varepsilon} - 1 \right)^{-1} \tag{6.55}$$

while the others are a function of the pressure-strain model:
Launder, Reece and Rodi (LRR), [34]

$$C_1 = 3.0, \qquad C_2 = 0.8, \qquad C_3 = 1.75, \qquad C_4 = 1.31 \tag{6.56}$$

Speziale, Sarkar and Gatski (SSG), [51]

$$C_1 = 3.4 + 1.8P/\varepsilon, \qquad C_2 = 0.8 - 1.3\sqrt{II_b}, \qquad C_3 = 1.25, \qquad C_4 = 0.4 \tag{6.57}$$

where II_b is the invariant $(b_{ij}b_{ij})$ of the specific anisotropy tensor[17]. The production-to-dissipation rate for the SSG pressure strain was set equal to 1.9, which is the value in equilibrium homogeneous flows, while the invariant of the anisotropy tensor was set to 0.11, which is the value predicted in two-dimensional homogeneous turbulence.

[17] $b_{ij} = (u_i u_j - 2/3k\delta_{ij})/2k$

In the model by Abid *et al.* [2], this relation is used together with either a $k-\omega$ EVM, or a $k-\varepsilon$ EVM. In the case of a $k-\omega$ model, the eddy viscosity is defined as:

$$\nu_t^* = C_\mu^* \frac{k}{\omega} \tag{6.58}$$

and C_μ^* depends on the flow:

$$\begin{aligned} C_\mu^* &= \left[\frac{C_2 - 4/3}{C_3 - 2}\right]\left[\frac{3\left(1+\eta^2\right) + 0.2\left(\eta^6 + \xi^6\right)}{3 + \eta^2 + 6\eta^2\xi^2 + 6\xi^2 + \eta^6 + \xi^6}\right] \\ \eta^2 &= S_{ij}^* S_{ij}^*, \qquad \xi^2 = \Omega_{ij}^* \Omega_{ij}^* \end{aligned} \tag{6.59}$$

Note that the expression for the C_μ^* has been changed in accordance with Abid *et al.* [1] for reasons of numerical stability. In the expression for the eddy viscosity Eq. (6.58), two additional transport equations is needed. In this report, the $k-\varepsilon$ and $k-\omega$ of Abid *et al.* [2] were employed. However, virtually any EVM can be used.

6.7.2 Wallin and Johansson

The description of the EARSM by Wallin and Johansson [25], [54], [55] is somewhat more complicated than that of Gatski and Speziale and is derived in a similar manner as the EARSM by Girimaji [14]. Their model is fully explicit using the full anisotropy expression, which in the limit of 2D flow offers an exact solution and in 3D flow an asymptotic 2D approximation. It is convenient to include the effects of rotation from the start, and Wallin and Johansson define a new absolute rotation tensor for this purpose. The mean rotation tensor is thus replaced by the absolute rotation tensor, Ω_{ij}^A, which is the sum of the mean rotation tensor and the solid body rotation tensor according to:

$$\Omega_{ij}^A = \Omega_{ij} + \Omega_{ij}^S \tag{6.60}$$

where Ω_{ij}^S is the solid body rotation tensor, defined as:

$$\Omega_{ij}^S = \epsilon_{jik}\Omega_k \tag{6.61}$$

Ω_k being the constant angular velocity. The solid body rotation term, Ω_{ij}^S, is closely connected with the Coriolis timescale; $2\epsilon_{ijk}\Omega_k$. Normally the Coriolis acceleration effects enter the transport equation for the Reynolds stresses via the body force. However, in this model, the Coriolis accelerations are split into two parts. The first part of this is included in the above absolute rotation tensor, Ω_{ij}^A, which is included in the shear generation term, see Eq. 6.43

$$\frac{P_{ij}}{k} = -\frac{4}{3}S_{ij} - \left(a_{ik}S_{kj} + S_{ik}a_{kj}\right) + a_{ik}\Omega_{kj}^A - \Omega_{ik}^A a_{kj} \tag{6.62}$$

and the second part of the Coriolis acceleration is included in the solid body rotational generation term:

$$\frac{G_{ij}^S}{k} = a_{ik}\Omega_{kj}^S - \Omega_{ik}^S a_{kj} \tag{6.63}$$

Apart from this change, the rapid part of the pressure-strain term must be modified. Taking the Launder-Reece-Rodi model, the rapid part is:

$$\frac{\Pi_{ij,2}}{k} = \frac{4}{5}S_{ij} + \frac{9c_2+6}{11}\left(a_{ik}S_{kj} + S_{ik}a_{kj} - \frac{2}{3}a_{km}S_{mk}\delta_{ij}\right) + \frac{7c_2-10}{11}\left(a_{ik}\Omega^A_{kj} - \Omega^A_{ik}a_{kj}\right) \tag{6.64}$$

where the absolute rotational tensor appears again, and thus the pressure strain term changes as a result of the solid body rotational velocity. Now we may rewrite the ARSM, Eq. 6.39:

$$\frac{\overline{u_i'u_j'}}{k}\left(\frac{P_k}{\varepsilon} - 1\right) = \frac{k}{\varepsilon}\left(\frac{P_{ij}}{k} + \frac{G_{ij}}{k} + \frac{\Pi_{ij}}{k}\right) - \frac{\varepsilon_{ij}}{\varepsilon} \tag{6.65}$$

and insert the above Eqs. 6.62, 6.63 and 6.64 together with the Rotta slow part, Eq. 6.29, and the isotropic dissipation rate, Eq. 6.34:

$$\begin{aligned}
\frac{\overline{u_i'u_j'}}{k}\left(\frac{P_k}{\varepsilon} - 1\right) = \\
- \underbrace{\frac{1}{\varepsilon}\left(\frac{2}{3}\varepsilon\delta_{ij}\right)}_{\text{isotropic dissipation}} \\
\underbrace{+\frac{k}{\varepsilon}\left[-\frac{4}{3}S_{ij} - \left(a_{ik}S_{kj} + S_{ik}a_{kj}\right) + a_{ik}\Omega^A_{kj} - \Omega^A_{ik}a_{kj}\right]}_{\text{shear generation}} \\
\underbrace{+\frac{k}{\varepsilon}\left[a_{ik}\Omega^S_{kj} - \Omega^S_{ik}a_{kj}\right]}_{\text{rotational generation}} \\
\underbrace{+\frac{k}{\varepsilon}\left[-c_1\frac{\varepsilon}{k}\left(\frac{\overline{u_i'u_j'}}{k} - \frac{2}{3}\delta_{ij}\right)\right]}_{\text{Rotta slow part}} \\
\underbrace{+\frac{k}{\varepsilon}\left[\frac{4}{5}S_{ij} + \frac{9c_2+6}{11}\left(a_{ik}S_{kj} + S_{ik}a_{kj} - \frac{2}{3}a_{km}S_{mk}\delta_{ij}\right) + \frac{7c_2-10}{11}\left(a_{ik}\Omega^A_{kj} - \Omega^A_{ik}a_{kj}\right)\right]}_{\text{LRR rapid part}}
\end{aligned} \tag{6.66}$$

Substituting the Reynolds stresses to the anisotropy tensor:

$$\frac{\overline{u_i'u_j'}}{k} = a_{ij} + \frac{2}{3}\delta_{ij} \tag{6.67}$$

LHS can be rewritten as:

$$\frac{\overline{u_i'u_j'}}{k}\left(\frac{P_k}{\varepsilon} - 1\right) = a_{ij}\left(\frac{P_k}{\varepsilon} - 1\right) + \left(\frac{P_k}{\varepsilon} - 1\right)\frac{2}{3}\delta_{ij} \tag{6.68}$$

Furthermore, noting that the normalized Rotta term is actually the anisotropy tensor multiplied by a constant:

$$\frac{k}{\varepsilon}\left[-c_1\frac{\varepsilon}{k}\left(\frac{\overline{u_i'u_j'}}{k}-\frac{2}{3}\delta_{ij}\right)\right]=-c_1 a_{ij} \tag{6.69}$$

it can be moved to the LHS to yield:

$$\begin{aligned}
a_{ij}\left(c_1+\frac{P_k}{\varepsilon}-1\right)+\left(\frac{P_k}{\varepsilon}-1\right)\frac{2}{3}\delta_{ij} &= -\frac{2}{3}\delta_{ij} \\
+\frac{k}{\varepsilon}\left[-\frac{4}{3}S_{ij}-(a_{ik}S_{kj}+S_{ik}a_{kj})+a_{ik}\Omega^A_{kj}-\Omega^A_{ik}a_{kj}\right] & \\
+\frac{k}{\varepsilon}\left[a_{ik}\Omega^S_{kj}-\Omega^S_{ik}a_{kj}\right] & \\
+\frac{k}{\varepsilon}\left[\frac{4}{5}S_{ij}+\frac{9c_2+6}{11}\left(a_{ik}S_{kj}+S_{ik}a_{kj}-\frac{2}{3}a_{km}S_{mk}\delta_{ij}\right)+\frac{7c_2-10}{11}\left(a_{ik}\Omega^A_{kj}-\Omega^A_{ik}a_{kj}\right)\right] &
\end{aligned} \tag{6.70}$$

The $2/3$ terms cancel out, while the P_k/ε term can be changed to:

$$\frac{P_k}{\varepsilon}\frac{2}{3}\delta_{ij}\equiv-\frac{k}{\varepsilon}\left[a_{mk}S_{km}\frac{2}{3}\delta_{ij}\right] \tag{6.71}$$

The term in front of the RHS, k/ε, is the turbulent time scale, τ, and is used to normalize the mean strain rate tensor and the mean rotation tensor:

$$\mathbf{S}^*\equiv\tau S_{ij}=\frac{\tau}{2}\left(\frac{\partial U_i}{\partial x_j}+\frac{\partial U_j}{\partial x_i}\right) \tag{6.72}$$

$$\Omega^*\equiv\tau\Omega^A_{ij}=\frac{\tau}{2}\left(\frac{\partial U_i}{\partial x_j}-\frac{\partial U_j}{\partial x_i}\right)+\tau\epsilon_{jik}\Omega_k \tag{6.73}$$

With this substitution, the equation is:

$$\begin{aligned}
\mathbf{a}\left(c_1+\frac{P_k}{\varepsilon}-1\right) &= \frac{2}{3}tr(\mathbf{aS}^*)\mathbf{I}-\frac{4}{3}\mathbf{S}^*-(\mathbf{aS}^*+\mathbf{S}^*\mathbf{a})+\mathbf{a}\Omega^*-\Omega^*\mathbf{a} \\
+\mathbf{a}\Omega^S-\Omega^S\mathbf{a}+\frac{4}{5}\mathbf{S}^*+\frac{9c_2+6}{11}\left(\mathbf{aS}^*+\mathbf{S}^*\mathbf{a}-\frac{2}{3}tr(\mathbf{aS}^*)\mathbf{I}\right)+\frac{7c_2-10}{11}\left(\mathbf{a}\Omega^*-\Omega^*\mathbf{a}\right) &
\end{aligned} \tag{6.74}$$

where the short notation for the identity tensor, $\mathbf{I}$, and the anisotropy tensor, $\mathbf{a}$, are used. To get the final version of the *implicit* ARSM, the rotation rate tensor is rearranged and the terms are added together:

$$\left(c_1-1+\frac{P_k}{\varepsilon}\right)\mathbf{a}=-\frac{8}{15}\mathbf{S}^*+\frac{7c_2+1}{11}\left(\mathbf{a}\Omega^R-\Omega^R\mathbf{a}\right)-\frac{5-9c_2}{11}\left(\mathbf{aS}^*+\mathbf{S}^*\mathbf{a}-\frac{2}{3}tr(\mathbf{aS}^*)\mathbf{I}\right) \tag{6.75}$$

where Ω^R is the effective mean rotation tensor which depends on the choice of pressure-strain model. In the case of the above LRR, the effective mean rotation tensor is:

$$\Omega^R=\Omega^A+\frac{11}{7c_2+1}\tau\Omega^S=\tau\Omega_{ij}+\frac{7c_2+12}{7c_2+1}\tau\Omega^S \tag{6.76}$$

The constant, c_2, was originally suggested, by Launder *et al.* to be 0.4 [34], although recent studies have indicated a slightly higher value. Setting $c_2 = 5/9$ in Eq. 6.75 would simplify the equation to:

$$\left(c_1 - 1 + \frac{P_k}{\varepsilon}\right)\mathbf{a} = -\frac{8}{15}\mathbf{S} + \frac{4}{9}\left(\mathbf{a}\Omega^R - \Omega^R\mathbf{a}\right) \tag{6.77}$$

Note that this still represents a non-linear ARSM relation since $P_k/\varepsilon = -tr\{\mathbf{aS}\}$. In order to formulate an EARSM of the above ARSM, the following steps must be performed [55]:

1. The general form of the anisotropy equation, Eq. 6.42, is inserted into the ARSM
2. The resulting linear equation system for the β coefficients is then solved with the aid of the Cayley-Hamilton theorem. The β coefficients are now functions of the production-to-dissipation ratio, P_k/ε
3. The last step is to formulate the non-linear scalar equation for the P_k/ε.

In the 2D case, these steps are shown in the report by Dahlström [9]. For the general 3D case, the non-zero β coefficients are:

$$\begin{aligned} \beta_1 &= -\frac{N(2N^2 - 7II_\Omega)}{Q}, \qquad \beta_3 = -\frac{12N^{-1}IV}{Q} \\ \beta_4 &= -\frac{2(N^2 - 2II_\Omega)}{Q}, \qquad \beta_6 = -\frac{6N}{Q}, \qquad \beta_9 = \frac{6}{Q} \end{aligned} \tag{6.78}$$

where the denominator is:

$$Q = \frac{6}{5}(N^2 - 2II_\Omega)(2N^2 - II_\Omega) \tag{6.79}$$

and N is related to the production-to-dissipation ratio as:

$$N = c_1' + \frac{9}{4}\frac{P_k}{\varepsilon}, \qquad c_1' = \frac{9}{4}(c_1 - 1) \tag{6.80}$$

The non-linear equation for N is then formulated, which in the general 3D case is a sixth-order equation. For a 2D case, this is reduced to a third order equation:

$$N^3 - c_1'N^2 - \left(\frac{27}{10}II_S + 2II_\Omega\right) + 2c_1'II_\Omega = 0 \tag{6.81}$$

which can be exactly solved. This also forms the approximation for the 3D case.

7 Turbulence Models and Rotation

Modeling rotating turbulent flow naturally suffers from the same limitations as does modeling non-rotating turbulent flow. Furthermore, the rotationally induced acceleration terms that appear result in increased complexity. The following is from a paper by Iacovides and Launder (1995) [23]

> To be fair, we must acknowledge that research sponsorship of CFD applied to internal cooling began at least a decade ago. It is however, a measure of the complexity of the flows involved – from both physical and computational points of view – that those 10 years have produced rather little in the form of well-validated, user-oriented software.

This is mainly because the numerically stable and less CPU-demanding models do a fairly poor job of predicting rotational effects. The still most commonly used turbulence models, the eddy-viscosity models (EVM), are based on the k equation[18], which does not include rotation. Hence, more advanced models are needed. However, the second-order moments models (RSM), which do predict rotational effects, have severe drawbacks. They are generally numerically cumbersome, and non-convergent solution can be the result.

7.1 EVM vs RSM

A profound result of strong Coriolis and centrifugal forces is the near-wall secondary flows. As a consequence, turbulence models need to resolve the near-wall region accurately to predict the overall flow. Thus the computationally efficient wall functions would not perform as well in these flows, as they do in other simpler flows[19]. Secondly, the strong streamline curvature in these flows gives the models based on eddy-viscosity a rather gloomy prospect for success.

Looking at the production terms in the transport equation for the Reynolds-stresses, Eq. 5.36, clarifies this. For simplicity, consider a unidirectional flow (2D) undergoing orthogonal mode rotation about the third axis. The production terms are, see [31]:

	i=1,j=1	i=2,j=2	i=3,j=3	i=1,j=2
P_{ij}	$-2\overline{u'v'}dU/dy$	0	0	$-\overline{v'}dU/dy$
G_{ij}	$4\Omega\overline{u'v'}$	$-4\Omega\overline{u'v'}$	0	$-2\Omega(\overline{u'^2} - \overline{v'^2})$

As can be noted from the above that the turbulent kinetic energy – which is the sum of the $\overline{u_i'u_i'}$ – is not affected by the rotation since $G_{ii} \equiv 0$. The generation of shear stress is:

$$P_{12} = -\overline{v'^2}\frac{dU}{dy} - 2\Omega\left(\overline{u'^2} - \overline{v'^2}\right) \tag{7.1}$$

The first term is either negative or positive and thus yields an increase of the shear stress on the pressure side of the channel (where $dU/dy > 0$) and a decrease on the suction side (where $dU/dy < 0$). In an eddy viscosity model, the second term in Eq. 7.1 is always zero, because the fluctuating velocities are isotropic. However, in a Reynolds-stress model, this term is present and is negative, providing that the streamwise fluctuations ($\overline{u'^2}$) exceed

[18] In addition to the k equation, another transport equation is needed, such as the dissipation rate, ε, specific dissipation, ω, or the turbulent time, τ

[19] The wall functions approach has severe limitations in other areas as well, e.g. heat transfer.

the cross-stream ($\overline{v'^2}$). Thus the eddy viscosity model predicts the same result regardless of whether there is a rigid body rotation, whereas a Reynolds stress based model with a more complex description of the Reynolds stresses captures the rotational effects.

7.2 Rotational Modifications to the EVMs

As stated above, the eddy viscosity concept will not include any generation due to the rotation. That is not to say that the secondary motions are not captured, since those are directly affected by the Coriolis acceleration and the term $2\epsilon_{ijk}\Omega_j u_k$ in the Navier-Stokes equation. Although the rotation does not affect the generation of the turbulent kinetic energy, it does affect the dissipation rate, see Eq. 5.70, although in a more intricate way. Normally this is neglected in the EVMs and thus the turbulence is not modified by solid body rotation at all. This deficiency, which is actually an effect of the underlying physics of the model, or rather lack of physics, has in some models been improved through some ad hoc terms. This may seem horrifying to some purists, but as we are dealing with turbulence *modeling*, it is yet another tuning process for the models. These ad hoc modifications are made to either the k equation or the ε equation or both. Below these modifications are exemplified through three different models.

7.2.1 $e-\omega^2$ Model of Wilcox and Chambers

One model that includes some effects of streamline curvature and rotation through the k equation was presented by Wilcox and Chambers [59]. Their model, which is a 2D model for boundary layers, consists of the turbulent kinetic energy, e, and the specific dissipation, ω^2. This model, which is not based on the ordinary $k-\varepsilon$ theme, and not even the, popular $k-\omega$ by Wilcox but rather on the $e-\omega^2$, is essentially equivalent to other models, except for one term, see [59]:

$$9\Omega\frac{e}{\omega}\frac{\partial U}{\partial y} \tag{7.2}$$

This term is associated with the rigid body rotation and is an ad hoc modification suitable for the $k-\varepsilon$ models. Wilcox and Chambers try to circumvent this fact, however by noting that their turbulent kinetic energy is equivalent to:

$$e = \frac{9}{4}\overline{v'^2} \tag{7.3}$$

in difference to the equiproportional k, which is:

$$k = \frac{1}{2}\left(\overline{u'^2}+\overline{v'^2}+\overline{w'^2}\right) = \frac{3}{2}\overline{v'^2} \tag{7.4}$$

Their reasoning is based on the fact that the near-wall behavior is anisotropic, and relations between the fluctuating energies are, see Hinze [19]:

$$\overline{u'^2} : \overline{v'^2} : \overline{w'^2} = 4:2:3 \tag{7.5}$$

By letting e depend only on $\overline{v'^2}$, the total energy would be:

$$\overline{u'^2}+\overline{v'^2}+\overline{w'^2} = 2\overline{v'^2}+\overline{v'^2}+\frac{3\overline{v'^2}}{2} = \frac{9\overline{v'^2}}{4} \tag{7.6}$$

In the $i = 2, j = 2$ equation for the Reynolds stresses, the following Coriolis term is evident, see table on page 47:

$$G_{22} = -4\Omega\overline{u'v'} \tag{7.7}$$

By assuming the Boussinesq hypothesis (2D):

$$-\rho u'v' = \nu_t \frac{dU}{dy} \tag{7.8}$$

the following term appears in the $\overline{v'^2}$ equation :

$$-4\Omega\overline{u'v'} = 4\Omega\nu_t \frac{dU}{dy} \tag{7.9}$$

Thus, in the e equation, the term would be ($9/4 \cdot \overline{v'^2}$ -equation):

$$9\Omega\nu_t \frac{dU}{dy} \tag{7.10}$$

as found above, with $\nu_t = e/\omega$. This term makes the model depend on the solid body rotation and it does predict some of the turbulent rotational effects. A general 3D variant of the above model adapted to a $k - \varepsilon$ based eddy viscosity was used by Howard *et al.* [20]. In this report, the additional term, $9\Omega\nu_t dU/dy$, is used together with the EVMs of Abid *et al.*.

7.2.2 The $k - \varepsilon$ Model of Launder *et al.*

It was stated above that the non-modified turbulent kinetic energy equation is not affected by rotation of the coordinate system. However, the dissipation rate equation will change, although it is not certain how it will change. The Coriolis term in the dissipation rate equation, ε is, see Eq. 5.60:

$$2\nu\overline{\frac{\partial u_i'}{\partial x_k}\frac{\partial}{\partial x_k}\left(2\epsilon_{imn}\Omega_m u_n'\right)} \tag{7.11}$$

It can be argued that this term should be dependent on the background vorticity, 2Ω, and the mean shear vorticity, $-dU/dy$, for an orthogonally rotating 2D flow [31]:

$$S = -\frac{2\Omega}{\partial U/\partial y} \tag{7.12}$$

This ratio can also be considered as a gradient rotational number. Bradshaw [5] used this ratio to define a Richardson number or, alternatively according to Tritton [53], the Bradshaw number as:

$$Ri = \text{or } B = S(S+1) \tag{7.13}$$

Launder *et al.* [33] choose this parameter as the modifier to their ε Eq.:

$$Ri = -2\Omega\left(\frac{\partial U}{\partial y} - 2\Omega\right) / \left(\frac{\partial U}{\partial y}\right)^2 \tag{7.14}$$

where the rotation is around the $z-$axis. This equation can be simplified according to Johnston *et al.* [26] to:

$$Ri = -\frac{2\Omega}{\partial U/\partial y} \tag{7.15}$$

in the near-wall region, which is used in the paper by Howard *et al.* [20]. This modification actually gave better agreement with experimental data than did the non-simplified Richardson number. The denominator of Eq. 7.14, $(\partial U/\partial y)^2$, has the dimension $(time)^{-2}$. Launder *et al.* proposed to replace this with the turbulent time scale, defined by:

$$\tau = \frac{k}{\varepsilon} \tag{7.16}$$

Thus the two Richardson numbers would be:

$$Ri = -2\Omega \left(\frac{k}{\varepsilon}\right)^2 \left(\frac{\partial U}{\partial y} - 2\Omega\right) \tag{7.17}$$

$$Ri = -2\Omega \left(\frac{k}{\varepsilon}\right)^2 \frac{\partial U}{\partial y} \tag{7.18}$$

Following similar reasoning as above, Launder *et al.* conclude that the k equation should be left as it is, thus turning to the ε equation:

> The ε equation itself is very much a black-box equation and there are, therefore, no clear guidelines as to whether, in the ε equation, the coefficient of the generation term (that containing mean strains) or the primary decay term (that containing C_2) or both should be modified. ... On the grounds of seeking the simplest possible form the present work has assumed that effects of curvature on the length scale can be accommodated by making only the effective value of C_2 depend on the Richardson number.

Thus, from this, the postulated modified ε equation would be:

$$\frac{D\varepsilon}{Dt} = C_{\varepsilon 1}\frac{k}{\varepsilon}P_k - C_{\varepsilon 2}(1 - C_c Ri)\frac{\varepsilon^2}{k} + \frac{\partial}{\partial x_j}\left[\left(\nu + \frac{\nu_t}{\sigma_\varepsilon}\right)\frac{\partial k}{\partial x_j}\right] \tag{7.19}$$

where factor C_c is a closure coefficient. Using several tests, this was optimized at $C_c = 0.2$, in [33]. The above ε equation together with a standard k equation defines the Launder *et al.* model.

7.2.3 Richardson Number Modifications According to Hellsten

Boussinesq eddy viscosity models which are modified according to system rotation are mostly based on the assumption that the turbulent length scale is corrected according to:

$$l = \frac{l_0}{1 + C_c Ri} \text{ or } l = l_0(1 - C_c Ri) \tag{7.20}$$

Hellsten [18], following the approach by Launder *et al.* used the second turbulent quantity (in this case the ω equation) to implement the length scale correction. The Richardson number used in the above Launder *et al.* $k - \varepsilon$ model could not be used, however, since

it is not generalized to three dimensions, as noted by Khodak and Kirsch [29]. Instead, the general Richardson number definition of Khodak and Hirsch is used:

$$Ri = -\left(\frac{k}{\varepsilon}\right)^2 |\Omega_{ij}| \left(|S_{ij}| - |\Omega_{ij}|\right) \tag{7.21}$$

In the case of a 2D rotating duct, this reduces to:

$$Ri = -\left(\frac{k}{\varepsilon}\right)^2 \left|\frac{\partial U}{\partial y} - 2\Omega\right| \left(\left|\frac{\partial U}{\partial y}\right| - \left|\frac{\partial U}{\partial y} - 2\Omega\right|\right) \tag{7.22}$$

Hellsten noted that this definition performed reasonably well in a 2D fully developed rotating channel. However, it deteriorated in a general 3D flow, where a new definition of the Richardson number was necessary:

$$Ri = \frac{|\Omega_{ij}|}{|S_{ij}|}\left(\frac{|\Omega_{ij}|}{|S_{ij}|} - 1\right) \tag{7.23}$$

Using the length scale correction equation 7.20 and the definition of the Richardson, the dissipation/destruction term in the ω equation is multiplied by the following factor:

$$\frac{1}{1 + C_{rc} Ri} \tag{7.24}$$

The closure coefficient, C_{rc}, was calibrated in the 2D fully developed flow in a rotating channel and given the value: $C_{rc} = 3.6$. Hellsten used this modification with the SST $k - \omega$ model of Menter [38]. In this report, this modification is used with the Abid *et al.* EVMs without any change to the constant. The modification factor has also been used in conjunction with the dissipation rate equation (ε or ω equation) in the EARSMs, to enhance the predictions in rotating structures.

7.3 Rotational Modifications to the RSMs

The Reynolds Stress Models (RSM) that have an exact formulation of the production terms also include the Coriolis-induced turbulence in a natural way, since this is also described exactly by the use of the Reynolds stresses in the body generation term. However, the substantial derivative of the Reynolds stresses, $D(\overline{u_i' u_j'})/Dt$, is not frame invariant, Launder *et al.* [35]. When a fixed body rotation is applied to this model, it thus causes a problem. The substantial derivative can however be made frame-invariant in several ways. One way is to add the production term, P_{ij}, to either side of the transport equation for the Reynolds stresses:

$$\frac{D\overline{u_i' u_j'}}{Dt} + P_{ij} = 2P_{ij} + G_{ij} + \ldots \tag{7.25}$$

or assign half of the rotation generation to the convective terms [20]:

$$\frac{D\overline{u_i' u_j'}}{Dt} - \frac{1}{2}G_{ij} = P_{ij} + \frac{1}{2}G_{ij} + \ldots \tag{7.26}$$

[20] This was done in the EARSM of Wallin and Johansson, see above.

Either way, the effective generation due to rotation is only half as great relative to the shear generation. The above rewriting might seem cosmetic, but it will affect the pressure-strain terms. The rotational effect produces an additional term, $\Pi_{ij,3}$, which can be written in a similar manner as the 'isotropizy-of-production' rapid part, $\Pi_{ij,2}$, as:

$$\Pi_{ij,3} = -c_2 \frac{1}{2}\left(G_{ij} - \frac{1}{3}\delta_{ij}G_{kk}\right) = -c_2\frac{1}{2}G_{ij} \tag{7.27}$$

The last identity is due to the zero trace of the rotational generation, see Eq. 5.39. The additional factor of 0.5 is according to the above reasoning. The rotationally induced term and the rapid term can thus be added:

$$\Pi_{ij,2} + \Pi_{ij,3} = -c_2\left(P_{ij} + \frac{1}{2}G_{ij} - \frac{1}{3}\delta_{ij}P_{kk}\right) \tag{7.28}$$

The constant c_2 is assigned the same value as the $\Pi_{ij,2}$ term because both terms originate from similar generation terms.

7.4 Rotational Modifications to the EARSMs

The rotational modifications to the EARSMs are included in the expression for the Reynolds stresses above. In the case of the Gatski and Speziale model, the non-dimensionalized rotational rate tensor is:

$$\Omega_{ij}^A = \frac{1}{2}g\tau(2 - C_4)\left[\Omega_{ij} + \left(\frac{C_4 - 4}{C_4 - 2}\right)\epsilon_{mji}\Omega_m\right] \tag{7.29}$$

where Ω_m is the solid body rotation, which thus changes the expression for the Reynolds stresses. This is contrary to the EVM based on the Boussinesq hypothesis, where the turbulence level is not affected by the rotation. In the case of the Wallin and Johansson EARSM, the solid body rotation enters simply through a modification of the mean rotation rate tensor:

$$\Omega_{ij}^A = \Omega_{ij} + \Omega_{ij}^S \tag{7.30}$$

where $\Omega_{ij}^S = \epsilon_{jik}\Omega_k$, and Ω_k is the solid body rotation. In addition to this modification, a body generation term is added:

$$\frac{G_{ij}^S}{k} = a_{ik}\Omega_{kj}^S - \Omega_{ik}^S a_{kj} \tag{7.31}$$

8 Heat Transfer Models

Less attention is generally given to the heat transfer models, and they are mostly of less complexity than the turbulence models used in conjunction with the Reynolds average Navier-Stokes equation. Using the same decomposition as for the velocities, the temperature can be written as:

$$\theta = \Theta + \theta' \tag{8.1}$$

Inserting this relation into the temperature equation, Eq. 3.12, and time averaging yields:

$$\frac{\partial \Theta}{\partial t} + \frac{\partial U_i \Theta}{\partial x_i} = \frac{\partial}{\partial x_i}\left(\frac{\nu}{Pr}\frac{\partial \theta}{\partial x_i} - \overline{u_i'\theta'}\right) \tag{8.2}$$

The resulting new unknown, $\overline{u_i'\theta'}$, is denoted the turbulent heat flux, and causes the same problems for the temperature equation as the Reynolds stresses do for the momentum equation. The turbulent Prandtl number, Pr_t, generally varies with the flow, see e.g. Kays [28]. In most turbulent Prandtl models a constant value is however used and is normally set to: $Pr_t = 0.92$. In this report, this last option has been used for all heat transfer predictions, although a turbulent Prandtl number depending on the wall approximate as devised by Kays was also tested.

8.1 Turbulent Prandtl Number Based Models

One approach toward modelling the turbulent heat flux is to assume that the Boussinesq hypothesis is equally valid for the temperature-velocity fluctuation as for the velocity-velocity fluctuations:

$$\overline{u_i'\theta'} = -\epsilon_h \frac{\partial \Theta}{\partial x_i} \tag{8.3}$$

with ϵ_h is denoted the *eddy diffusivity of heat* in a similar manner as the eddy-viscosity, ν_t. In order to distinguish the different phenomena from each other, the eddy-viscosity is sometimes denoted as the *eddy diffusivity of momentum*, ϵ_m. From the above definition of eddy diffusivities, a turbulent Prandtl number can be defined:

$$Pr_t = \frac{\epsilon_m}{\epsilon_h} \tag{8.4}$$

With knowledge of the turbulent Prandtl number, the heat transfer model is defined. Substituting the Boussinesq assumption and the definition of the turbulent Prandtl number into the averaged heat transfer equation, Eq. 8.2 yields:

$$\frac{\partial \Theta}{\partial t} + \frac{\partial U_i \Theta}{\partial x_i} = \frac{\partial}{\partial x_i}\left(\frac{\nu}{Pr} + \frac{\nu_t}{Pr_t}\right)\frac{\partial \Theta}{\partial x_i} \tag{8.5}$$

with $\nu_t = \epsilon_m$ in the definition of the turbulent Prandtl number.

8.2 Reynolds Stress Based Models

In the case that a second order moment model is used for the turbulent transport equation, and the Reynolds stresses are thus known, it is possible to utilize the Generalized Gradient-Diffusion Hypothesis (GGDH) of Daly and Harlow [10]:

$$-\overline{u_i'\theta'} = c_\theta \overline{u_i'u_j'} \frac{k}{\varepsilon} \frac{\partial \Theta}{\partial x_j} \tag{8.6}$$

where $c_\theta = 0.3$. However, in the flows investigated in this report, it was found by Raisee [46] that the GGDH does not improve the predictions of heat transfer.

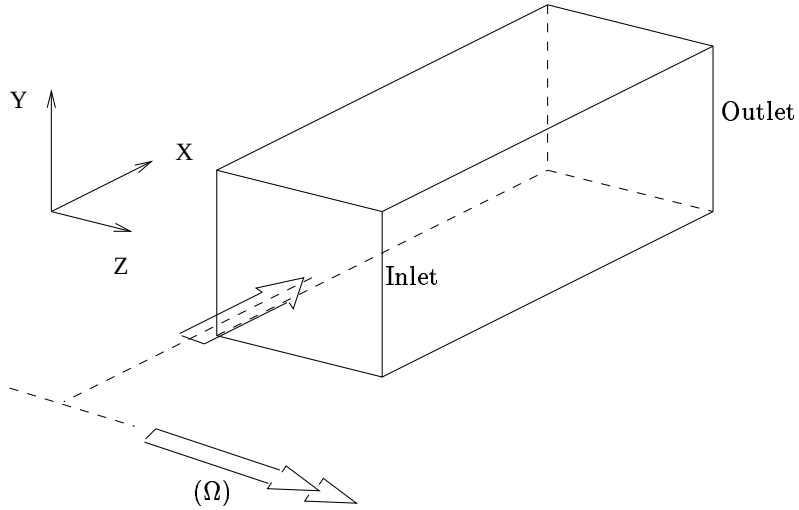

Figure 9.1: General Outline of the Test Cases

9 Numerical Aspects

9.1 Solver

The code with which all the following computations are made is a domestic Finite Volume Method (FVM) code: CALC-BFC, developed by Davidson and Farhanieh [11]. The code employs collocated variables using Boundary Fitted Coordinates (BFCs), on a non-orthogonal coordinate system. SIMPLEC is used for the pressure-velocity coupling. The code uses Hybrid discretization scheme for the turbulent quantities and QUICK for the momentum equations. A Tri-Diagonal Matrix Algorithm (TDMA) is employed to solve the discretised differential equations.

9.2 Periodic Flow Condition

The cases examined here have a geometrical pattern which identically repeats itself after a certain distance in the stream-wise direction, i.e. the flow is periodic. These geometrical modules, with a generally appearance as in Fig. 9.1, have identical inlet and outlet flow data except for the pressure and temperature field. This makes it possible, after modifications, to perform the calculations for only one of these modules, with a correspondingly reduced computational effort. The governing equations, Eqs. 3.3 and 3.12, however need to be modified. The reason for this is that pressure and temperature do not repeat themselves in each module, since they will continuously decay/increase along the stream-wise direction. In a periodic flow regime, the pressure, P, and temperature, Θ, can be decomposed into a fluctuating term and a linearly varying term in the stream-wise direction [42]. In a 2D case with the periodic condition in the x-direction, the following will apply:

$$\begin{aligned} \Theta(x,y) &= \tilde{\Theta}(x,y) + \frac{d\overline{\Theta}}{dx}x \\ P(x,y) &= \tilde{P}(x,y) - \frac{d\overline{P}}{dx}x \end{aligned} \tag{9.1}$$

where the fluctuating terms, $\tilde{P}(x, Y)$ and $\tilde{\Theta}(x, y)$, identically repeat themselves in each module. The linear temperature increase is given by the heat flux and mass flow:

$$\frac{d\overline{\Theta}}{dx} = \frac{\dot{Q}}{\dot{m}c_p L} \tag{9.2}$$

The level of the pressure gradient must be found iteratively. Apart from the substitution of the above fluctuating pressure, $\tilde{P}$, and temperature, $\tilde{\Theta}$, additional source terms are needed in the momentum equation ($d\overline{P}/dx\delta_{i1}$) and in the temperature equation ($-\rho U_i d\overline{\Theta}/dx\delta_{i1}$), both of which appear on the right-hand side of Eq. 3.3 and Eq. 3.12, respectively.

9.3 Boundary Conditions

9.3.1 Cyclic

The inlet and outlet have periodic boundaries, as noted above, with the identity given as:

$$\begin{aligned} \phi(ni) &= \phi(2) \\ \phi(1) &= \phi(ni-1) \end{aligned} \tag{9.3}$$

where ϕ will be the velocity components, U_i, the fluctuating pressure, $\tilde{P}$, temperature, $\tilde{\Theta}$, and the turbulent properties, k, ε or ω.

9.3.2 Walls

The walls were set at no-slip condition, where zero values of velocities were enforced. In the case of temperature predictions, this was set as uniform heat flux on the walls. The heat flux on the rib faces, face AB, BC and CD in Fig. 10.5, was set to 1/3 of the nominal heat flux to yield a constant total heat flux through the base area of the lower wall. This simplified heat flux wall condition may have resulted in some discrepancies in the predicted Nusselt number.

The turbulent properties were set to zero (k and Reynolds stresses) apart from the ω in the $k-\omega$ equations. Due to the definition of the specific dissipation, the value of ω goes to infinite at the walls. This is not applicable in a numerical scheme, however, and an approximate value is needed. According to Wilcox [56] and Menter [38], the boundary condition of ω is inversely proportional to the wall distance squared:

$$\omega = \text{constant}\frac{\nu}{C_{\omega 2} y^2} \tag{9.4}$$

This approximation is valid for $y^+ < 2.5$, according to Wilcox [58]. For a mesh-independent solution, there should be seven to ten nodes within this range, which is an unrealistic demand in the present predictions, especially for higher Reynolds number cases. As will be shown in the next section, this demand can be eased and still result in grid-independent results.

9.4 Implementation Considerations

The code CALC-BFC uses a systematic approach when solving the different variables, which, can be generalized according to:

$$\frac{\partial}{\partial t}(\rho\Phi) + \frac{\partial}{\partial x_i}(\rho U_i \Phi) = \frac{\partial}{\partial x_i}\left(\Gamma_\Phi \frac{\partial \Phi}{\partial x_i}\right) + S \tag{9.5}$$

This differential equation is used for velocities, turbulent quantities (k, ε/ω) and temperature. The source term, S, includes all remaining terms in the equations, such as the production and dissipation term in the turbulent differential equations. In the case of an EARSM, the solution method is to solve the Reynolds stress equation in a separate routine. The stresses then affect the momentum equation through a split operation. The Reynolds stresses are divided into an eddy viscosity part and a remaining part which, in the case of the Gatski and Speziale EARSM, are as follows:

$$\begin{aligned}\overline{u_i u_j} = &\underbrace{\frac{2}{3}k\delta_{ij} - 2C_\mu^* k\left(S_{ij}^* - \frac{1}{3}S_{kk}^*\delta_{ij}\right)}_{\text{EVM}} \\ &\underbrace{-2C_\mu^* k\left[\left(S_{ik}^*\Omega_{kj}^* + S_{jk}^*\Omega_{ki}^*\right) - 2\left(S_{ik}^* S_{kj}^* - \frac{1}{3}S_{kl}^* S_{kl}^*\delta_{ij}\right)\right]}_{\text{OT}}\end{aligned} \tag{9.6}$$

where OT is short for other terms. The EVM part is included in the momentum equation through the eddy viscosity in a similar way as an model based on the Boussinesq hypothesis, while the other terms are included in the source term of the momentum equation. This operation is made for reasons of numerical stability, which is necessary in more complex flow geometries. Note also that the EARSMs use the standard k and ε, ω equations in addition to the Reynolds stresses, which makes the implementation of the EARSM very similar to that of the EVMs. The additional computational effort for solving the Reynolds stresses explicitly is fairly small, which makes the EARSM very attractive for an EVM-based code.

The solution of the EVMs is straightforward, apart from the zonal or two-layer $k-\varepsilon$ model, which uses two different solution techniques depending on where in the flowfield the solution is required. Close to the walls, the one-equation low-Reynolds number (LRN) model is used, and further out in the flowfield the model reverts to the standard two-equation $k-\varepsilon$ high-Reynolds number (HRN) model. A profound problem with this is to decide where the partition line between the HRN model and LRN model should be. In the following computations, a pre-selected grid line was chosen, which makes the implementation easier and numerically more robust, although a trial-and-error method was needed since the correct partition line could only be obtained from a converged solution, and thus several runs were needed for each test case. According to Chen and Patel [7], the one-equation model should be used for nodes which have a y^+ of 50 or less.

The number of nodes at which the boundary condition for the ω – in the $k-\omega$ models – is fixed, through Eq. 9.4, is also pre-selected. This is a much smaller problem than for the zonal, since ω is fixed only for a very small number of nodes[21], which even in a separated flow regime do not depart a great deal from the desired number of fixed nodes.

9.5 Meshes

In all numerical simulations, the mesh plays an important part in the computational considerations. A good mesh is sometimes essential to reach convergence. In most cases, the computational effort increases with the size of the grid and, generally, the finest grid

[21] In these test cases, one to three nodes are used.

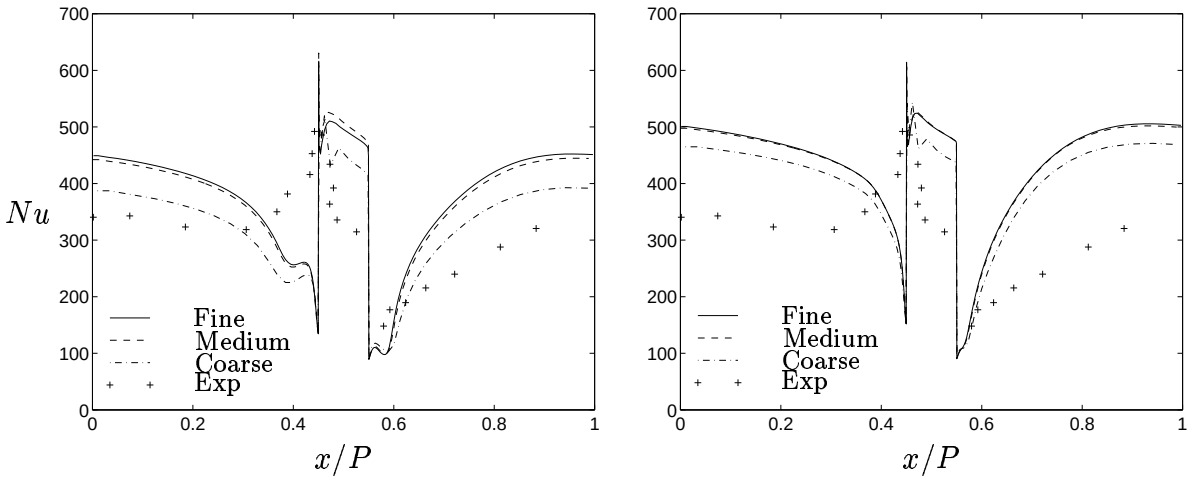

(a) Abid *et al* $k-\omega$ (b) Peng *et al* $k-\omega$

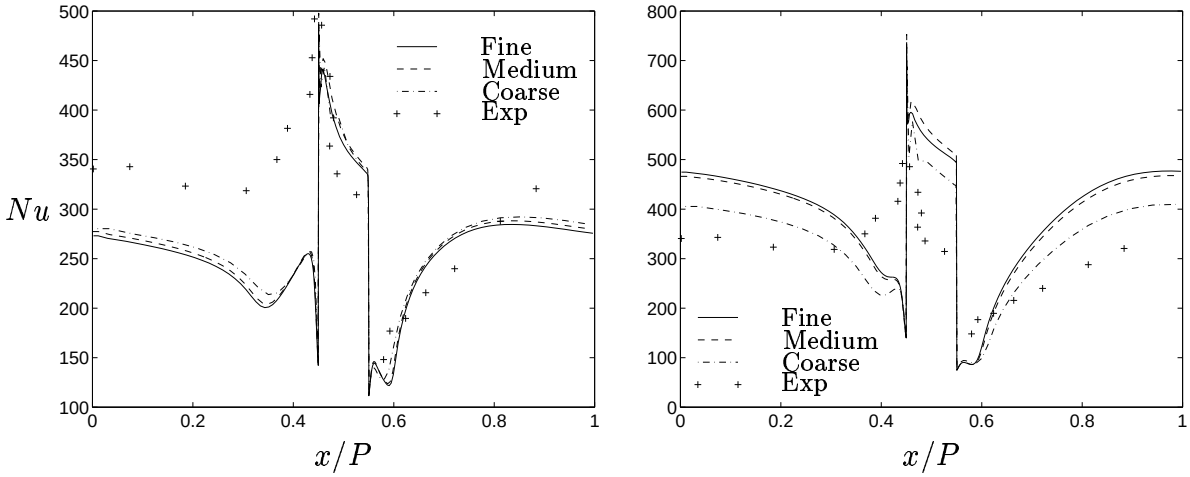

(c) Zonal $k-\varepsilon$ (d) EARSM

Figure 9.2: Nusselt Number, 2D Ribbed Channel

also gives the most correct results. In other cases, only a very coarse mesh can give a converged solution and, in these cases, the results should be treated very carefully. The conclusion to be made from such a simulation should perhaps be that, for such a combination of model and test case, a converged solution could not be reached, even though some results were achieved for a particular mesh. Three important parameters of a mesh are the aspect ratio, the skewness ratio and the stretching factor. The aspect ratio defines the ratio between one side of the control volume with respect to another side. Generally, the nodes should be as close to a square as possible. The skewness ratio is an indicator of the angle in the corners and, because squared cells are preferable, an angle of 90° is desirable. Since the computational mesh in this thesis is orthogonal, the skewness ratio is always one. The stretching factor defines the change in size of the nodes from one position to another. A factor of 1.2, indicating an increase of 20% for the cell length from one cell to the next, is generally regarded as an upper limit.

For a certain mesh, it is very difficult to conclude whether it is good enough, and often it does not help to compare with experiments or other results. To be certain of the

quality of the mesh, a grid-independent check must be made. In this case, a number of runs on different meshes are made and the solutions are then compared. If the results from the finest and the next finest mesh are nearly equal the results are considered to be grid-independent. That is not to say that the results are correct, but at least that they are not dependent on the mesh. A number of mesh checks were made, and only two of the test cases are shown here, the Rolls-Royce 2D ribbed channel and the UMIST 3D ribbed channel (stationary).

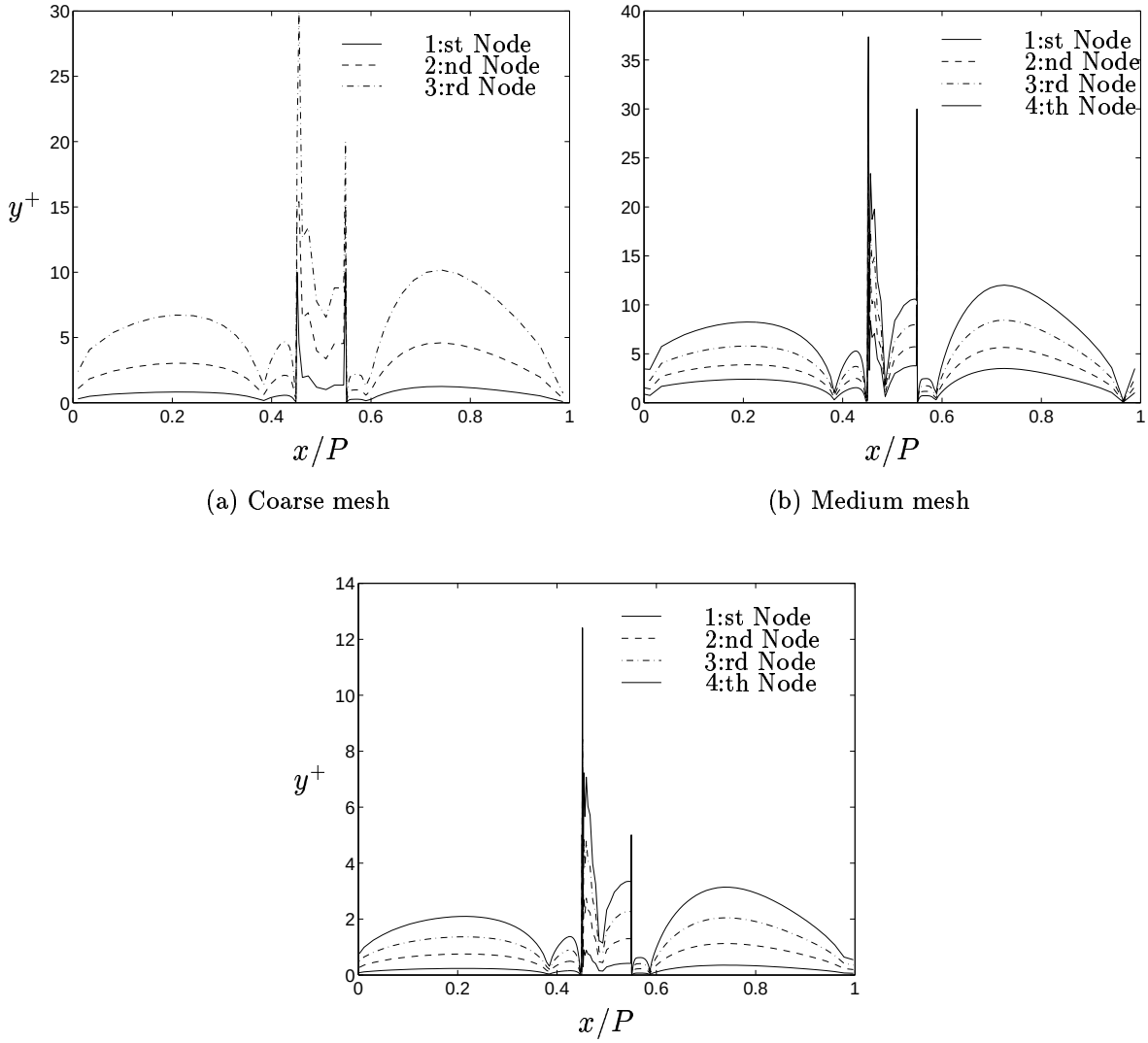

(a) Coarse mesh

(b) Medium mesh

(c) Fine mesh

Figure 9.3: y^+ Values for First Nodes, 2D Ribbed Channel

The 2D ribbed channel, Rolls-Royce case, has a $Re = 122\,400$[22], which is fairly high and thus needs a relative fine mesh to be grid-independent. The variable that is compared is the Nusselt number[23], which is the most grid-sensitive variable solved. Three different meshes were employed: the coarse mesh measuring: 55×60, the medium mesh, 110×120 and the fine mesh, 140×180. Four different turbulence models are used: the Abids *et al.*

[22]See the results section for further details.

[23]The Nusselt number is the non-dimensional heat flux.

$k-\omega$ [2], the Peng *et al* $k-\omega$ [43], Chen and Patel two-layer $k-\varepsilon$ [7] and the Gatski and Speziale EARSM [13], based on the Abid *et al.* $k-\omega$ EVM. Fig. 9.2 shows the grid sensitivity of the different turbulence models, where the results on the different meshes are compared.

For all turbulence models, a grid-independent solution is reached with the medium mesh. In the case of the zonal model, even the coarse mesh gives a fairly good outcome. In the case of a $k-\omega$ based model (including the EARSM), the boundary condition for the ω is an important matter for correct wall behavior and thus a grid-independent solution. As stated above, the ω value for the wall proximate node(s) is fixed through an equation based on the wall distance, see Eq. 9.4. In this case, the number of nodes used for fixing the ω are: one, two and three nodes for the coarse, medium, and fine mesh, respectively. The Peng *et al.* model is used to visualize the difference in the y^+ value of the near-wall nodes. Fig. 9.3 shows the first three/four nodes for the lower ribbed wall and their y^+ value along the surface.

If the medium mesh can be accepted as a grid-independent mesh, c.f. Fig. 9.2(b), then it seems sufficient to fix only two nodes – if these are within roughly $y^+ < 2.5$. The Wilcox [58] condition of seven to ten nodes within $y^+ < 2.5$ is clearly a very restricted requirement, although there is of course a difference between a correct ω value and a correct Nusselt number, which obviously depends on more than only the ω equation. Comparing the coarse mesh 9.3(a) and the medium mesh 9.3(b), it can be seen that the y^+ value for the second node is fairly similar over most of the channel, while the Nusselt number predicted by the coarse and medium mesh differs a great deal. This indicates that fixing only one node, as is done for the coarse mesh, even though the y^+ value is in the correct range, is not sufficient for capturing the heat flux. It must be admitted that this is not the only difference between the meshes. However, from other predictions, it has also been seen that fixing at least two nodes is required when using a $k-\omega$ model. From Fig. 9.3 it can also be noted that the y^+ value approaches zero at several points. These are the points at which the flow either separates or re-attaches[24]. If some of the terms, such as damping terms, in a turbulence model are based on y^+, the prediction of the model at these points will be inadequate.

The second case is the UMIST 3D ribbed channel case, with a Reynolds number of: $Re = 100\,000$. This case has a staggered rib configuration, which adds complexity[25]. The grid independency computations were made on a 2D mesh, symbolizing the centerline of the square duct. This was made to save time, since a 3D computation is much more computer resource demanding. The meshes for the course, medium and fine grid were: 60×60, 120×120 and 150×150, respectively. The turbulence models used in this computation were: the Abids *et al.* $k-\omega$ [2], Chen and Patel two-layer $k-\varepsilon$ [7] and the Gatski and Speziale EARSM [13] based on the Abid *et al.* $k-\omega$ EVM. In Fig. 9.4, the grid sensitivity of the different models can be compared.

Contrary to the Rolls-Royce case, this case does not reach grid-independent solutions for all turbulence models. In the case of the $k-\omega$ and EARSM models, probably not even the computation on the finest grid can be considered grid-independent. This is obviously a problem later on when a 3D computation is made on this case with a rather coarse mesh. The zonal $k-\varepsilon$ model reaches however a grid-independent solution, and even the first coarse grid gives a fairly reasonable grid-independent result – which is not to say

[24] See further discussion in the results section

[25] For further details see the result section.

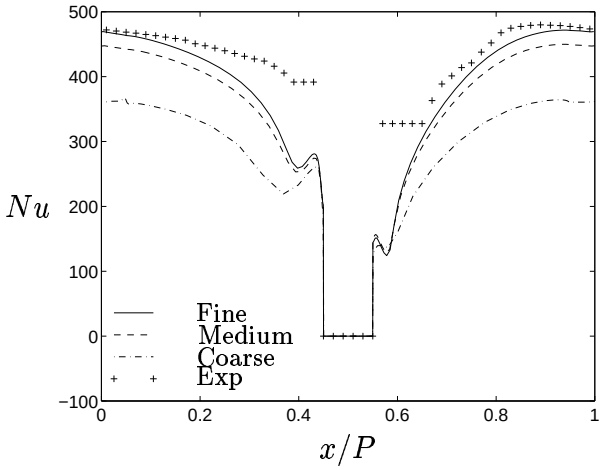

(a) Abid *et al* $k-\omega$

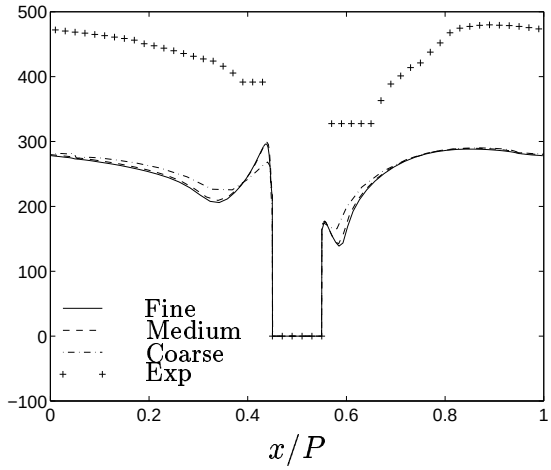

(b) Zonal $k-\varepsilon$

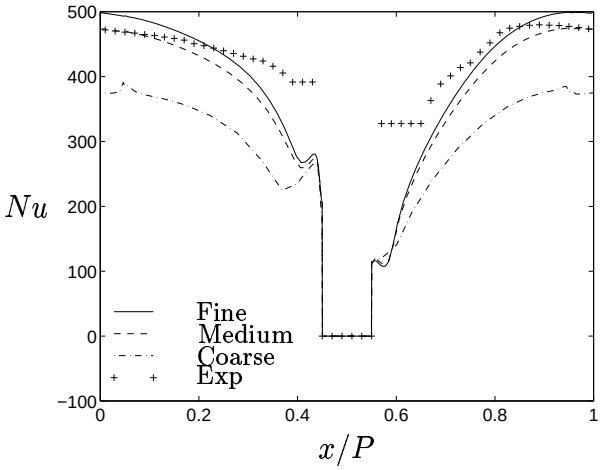

(c) EARSM

Figure 9.4: Nusselt Number on Centerline, 3D Ribbed Channel

that the prediction and the experimental results agree!

10 Results

This section presents a number of test cases which have been tested with several different turbulence models. It could be concluded that this is a turbulence model test, and in some way it is – however the main point is to test the models and state which model(s) performs best in these environments. This is not often based on only one test case; some real conclusions can be drawn about the performance of a turbulence model – and hence the models are tested in this thesis against different complex test cases.

There are two geometrically distinct differences between the test cases: they are either two-dimensional (2D) or three-dimensional (3D). In the case of a 2D calculation, the third axis has an enforced symmetrical boundary condition, which essentially means that the channel is infinitely wide. A judgement of how close this asymptotic condition may be achieved in either applications or in experimental rigs is left to the reader. The predictions are of course made in strict 2D, but it is reasonable to believe that the deviation between a 2D prediction and a wide 3D prediction is fairly similar for all turbulence models. Thus conclusions and discussions of the performance of the turbulence models can be closed without any hesitation regarding the two-dimensionality. It should also be noted that it is arranged in most of the 'two-dimensional' experiments that the side-wall effects are small, and thus any data points extracted from the centerline can be treated as two-dimensional data. The other geometrical case, the 3D cases, do not need this approximation, however, instead of experimental problems, the 3D cases are numerically more troublesome. The meshes increase greatly in size when a 3D calculation is done instead of a 2D and, hence, whenever possible, a 2D calculation is performed. For the three dimensional calculations included the meshes are not refined on the same level as for the 2D calculations. This is due to the very great increase in computational resources needed, which should be kept in mind in comparisons of the fairly good results of a 2D run with the less good results of a 3D run.

There are a few repeatedly used parameters which should be discussed before they are used. The first is the *Reynolds number*, $Re = UH/\nu$. The velocity is commonly taken as the mean or bulk velocity, U_m, U_b. The length scale for a channel should be the hydraulic diameter, $D_h = 4A/P$, although it can also be based on the channel height, H, or the channel half-height, h. In a duct with a square cross-section, the hydraulic diameter and the channel height are identical, which in all other cases they differ. In the 2D limit, the hydraulic diameter is $D_h = 4HB/(2H + 2B) = 2H$, although the channel height is used in most cases. Notations Re_D, Re_H and Re_h thus indicate a Reynolds number based on the hydraulic diameter, the channel height and the channel half-height, respectively.

The second parameter which is the *rotational number*, $Ro = \Omega H/U$, which is the inverse of the Rossby number. Ω is the angular velocity, and U is the streamwise velocity. H is a characteristic length which is taken either as the channel height, H, or the hydraulic diameter, D_h.

The third parameter is the *Nusselt number* which, for a prescribed heat flux at the wall, q_w, is $Nu = 2q_w Pr_l H/\mu c_p(\theta_w - \theta_b)$, where Pr_l is the molecular Prandtl number, H is the channel height (or hydraulic diameter), θ_w is the wall temperature and θ_b the bulk temperature. This is the fundamental heat transfer parameter, which is used whenever heat transfer is calculated.

10.1 Test Cases

Some characteristics of the different test cases is briefly given below.

2D Rotating Channel: Two test cases are made for the 2D rotating channel, one in comparison with DNS data of Kristofersen and Andersson [31] and the other with an experiment by Johnston *et al.* [26].

DNS-data	$Re_H = 5800$	$Ro_H = 0.2$	[31]
Experiment	$Re_H = 11500$	$Ro_H = 0.21$	[26]

2D Ribbed Channel: There are a total of six different 2D ribbed roughened test cases. They are denoted according to where or by whom the experiment was made:

Drain, Martin(H)	$Re_D = 12\,600$	$P/e = 7.2$	$e/H = 0.2$	[12]
Drain, Martin(F)	$Re_D = 37\,200$	$P/e = 7.2$	$e/H = 0.2$	[12]
Baughn, Yan	$Re_H = 50\,000$	$P/e = 10$	$e/H = 0.0625$	[3]
UMIST(a)	$Re_H = 100\,000$	$P/e = 10$	$e/H = 0.1$	[39]
UMIST(b)	$Re_H = 40\,000$	$P/e = 10$	$e/H = 0.1$	[39]
Rolls-Royce	$Re_H = 122\,400$	$P/e = 10$	$e/H = 0.1$	[24]

In all cases except the Drain and Martin(F) case, there exist only Nusselt data with which to compare. The Drain & Martin(F) test case includes only velocity data[26].

3D Rotating Channel: In the section on 3D rotating channel, only one comparison is made, with a LES computation of Pallares and Davidson [40]. In addition to the rotating case, a stationary case is also presented. The Reynolds number is $Re_H \approx 4000$, and, in the case of rotation, the rotational number is $Ro_H = 0.1$.

3D Ribbed Channel: In the case of a three dimensional ribbed channel, two different experiments are used to make comparisons with the predictions:

Baughn	$Re_H = 50\,000$	$Ro_H = 0$	$P/e = 10$	$e/H = 0.0625$	[3]
UMIST	$Re_H = 100\,000$	$Ro_H = 0$	$P/e = 10$	$e/H = 0.1$	[22]
UMIST	$Re_H = 100\,000$	$Ro_H = 0.2$	$P/e = 10$	$e/H = 0.1$	[22]

10.2 2D Rotating Channel

This section gives a specific feature of the turbulence models: whether or not they are capable of modifying the predictions due to rotational induced forces. Since the test cases are 2D with infinite width, see Fig. 10.1, the otherwise very dominant Coriolis force is not present and thus only second order effects are captured. In the case of a standard eddy viscosity model, the velocity profiles are fully symmetric even though both DNS data and experiments show an increasingly asymmetric profile with higher rotational numbers. To mimic the features shown in the experiments, a number of modifications are possible for the standard EVM; these are adding non-linear terms, as in EARSM, or modifying either the k-equation or the ε, ω or both.

These modifications add up to a large variety of possible turbulence models. The models used in this section are listed below:

[26]Notation F is for Flowfield and H for Heat transfer

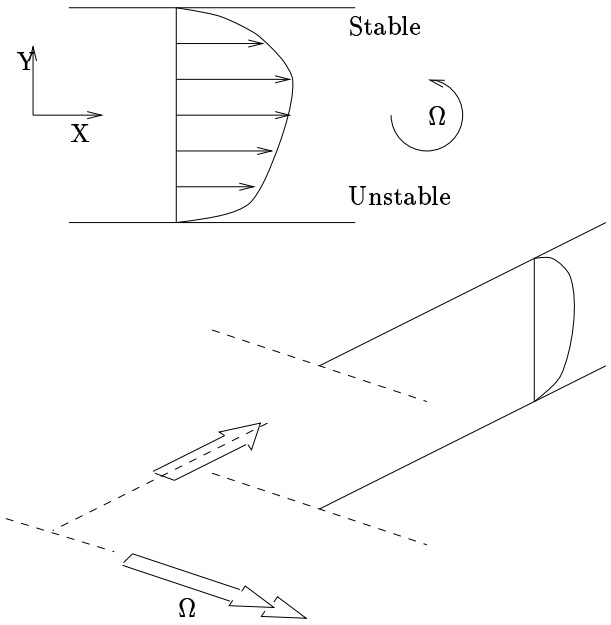

Figure 10.1: Geometry of 2D Rotating Channel

- Standard $k-\omega$, Abid *et al.* [2] (Std $k-\omega$)
- $k-\omega$ with modification to the k-Eq., Wilcox and Chambers [59] ($k-\omega$ mod k)
- $k-\omega$ with modification to the ω-Eq., Hellsten [18] ($k-\omega$ mod ω)
- Standard $k-\varepsilon$, Abid *et al.* [2] (Std $k-\varepsilon$)
- $k-\varepsilon$, with modification to the k-Eq., Wilcox and Chambers [59] ($k-\varepsilon$ mod k)
- $k-\varepsilon$ with modification to the ε-Eq., Hellsten [18] ($k-\varepsilon$ mod ε)
- Gatski and Speziales' [13] EARSM based on Abid *et al.'s* [2] $k-\omega$ with the SSG pressure-strain model. (SSG-EARSM(GS)-$k-\omega$)
- Gatski and Speziales' [13] EARSM based on Abid *et al.'s* [2] $k-\omega$ with the SSG pressure-strain model and modification to the ω-Eq., Hellsten [18] (SSG-EARSM(GS)-$k-\omega$ mod ω)
- Gatski and Speziales' [13] EARSM based on Abid *et al.'s* [2] $k-\varepsilon$ with the SSG pressure-strain model. (SSG-EARSM(GS)-$k-\varepsilon$)
- Gatski and Speziales' [13] EARSM based on Abid *et al.'s* [2] $k-\omega$ with the LRR pressure-strain model. (LRR-EARSM(GS)-$k-\omega$)
- Johansson and Wallin's [55] EARSM based on Abid *et al.'s* [2] $k-\varepsilon$ with the LRR pressure-strain model. (LRR-EARSM(JW)-$k-\varepsilon$)

Two different test cases are used in this section, one a DNS prediction [31] and the other an experiment [26].

10.2.1 DNS Test Case, $Re_H = 5800, Ro_H = 0.2$

In the case of the DNS comparison the Reynolds number based on the channel half-height is $Re = U_m h/\nu = 2900$, which is equivalent to a wall-shear Reynolds number of $Re_\tau = u_\tau h/\nu = 194$. The computation was made on mesh measuring 30×100, with 100 nodes in the wall normal direction, giving enough nodes to achieve a y^+ value of less than one for the first node. 30 nodes were used in the streamwise direction, even though the flow is fully developed and essentially a 1D prediction could have been done. The extra nodes in the streamwise direction were used to smooth out any iteration fluctuations in the massflow rate. The DNS database has a number of different rotational numbers, although only $Ro_H = 2\Omega h/U_m = 0.2$ has been used for comparison here. This rotational number was chosen because it is in the range found in turbine blades in gas turbines and it is high enough to clearly indicate the problems the different turbulence models have in predicting the flowfield. The most striking difference between a rotational and a stationary 2D duct prediction is the amplification of the turbulent kinetic energy on the unstable side, and the reduction of the same on the stable side for the rotating case. This changed level of turbulent kinetic energy affects the mean velocity profile as well through a stabilization process on the stable side and a more sharp gradient on the unstable side – as can be seen on the schematic figure, Fig. 10.1. One of the fundamental important parameters closely connected to this process is the friction velocity, u_τ, at the two walls. A table comparing the predicted friction velocity from the different turbulence models and from the DNS data is shown below:

Model	U_m/u_τ	$U_m/u_{\tau s}$	$U_m/u_{\tau u}$
DNS	15.23	18.54	10.76
Std $k-\omega$	15.33	15.33	15.33
$k-\omega$ mod k	14.63	18.85	12.37
$k-\omega$ mod ω	15.09	20.12	12.59
Std $k-\varepsilon$	17.14	17.14	17.14
$k-\varepsilon$ mod k	11.12	14.96	9.24
$k-\varepsilon$ mod ε	14.52	21.86	11.63
SSG-EARSM(GS)-$k-\omega$	16.21	18.60	14.55
SSG-EARSM(GS)-$k-\omega$ mod ω	15.12	19.71	12.73
LRR-EARSM(GS)-$k-\omega$	16.02	18.36	14.40
SSG-EARSM(GS)-$k-\varepsilon$	15.98	17.05	15.11
LRR-EARSM(JW)-$k-\varepsilon$	20.16	25.28	17.26

The model is abbreviated according to the above list; u_τ is simply the RMS value of the friction velocity on the stable (laminar) side, $(u_{\tau s})$, and the unstable (turbulent) side, $(u_{\tau u})$: $u_\tau = \sqrt{0.5(u_{\tau s}^2 + u_{\tau u}^2)}$. A high U_m/u_τ, and thus a low u_τ, indicates a low value of the turbulent kinetic energy which can be found on the stable side of the channel and vice versa on the unstable side. Apart from the non-modified, i.e. standard $k-\varepsilon$ and $k-\omega$ models, all models predict higher levels of u_τ on the unstable side than on the stable side. The two standard EVMs predicted equal friction velocities on both sides, clearly a large discrepancy of the non-modified EVM. None of the models yield good agreement with the DNS data. However, although there is a relative large discrepancy for the wall quantities, reasonable mean properties could still be predicted as seen below.

The velocity profiles normalized with mean friction velocity, $U(y)/u_\tau$, are depicted in Fig. 10.2. Note that the friction velocity was taken from the DNS predictions. In

the graphs, the wall-normal coordinate (y) is found on the abscissa and the streamwise direction (U) is on the ordinate. The 2D duct is rotating (positively) around the z-axis, and thus the stable (laminar) side is found at $y = +1$ and the unstable (turbulent) side at $y = -1$. Both the $k-\omega$ model, see Fig. 10.2(a), and the $k-\varepsilon$ model, see Fig.

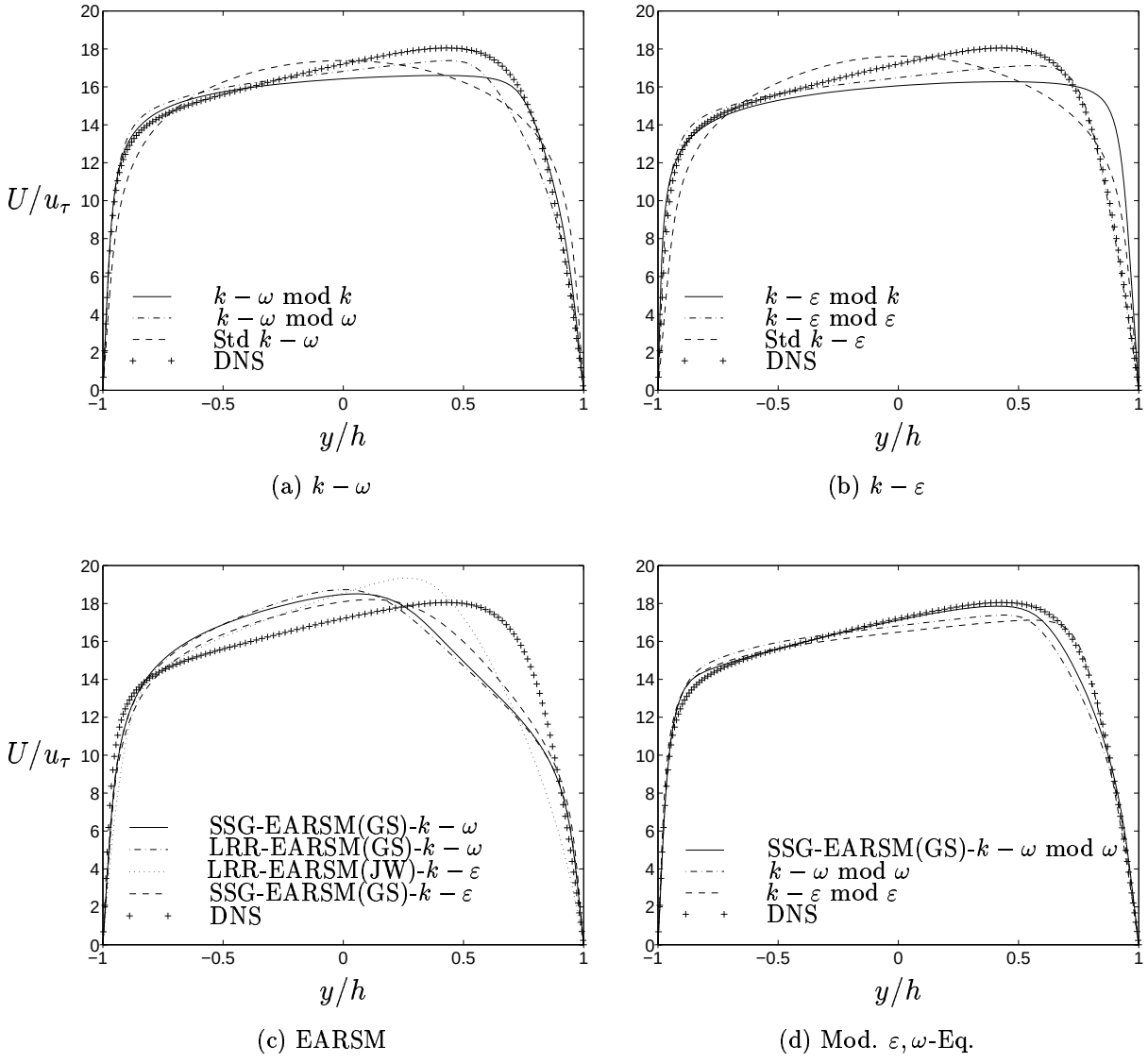

(a) $k-\omega$ (b) $k-\varepsilon$

(c) EARSM (d) Mod. ε,ω-Eq.

Figure 10.2: Velocity Profiles, Rotating 2D-duct

10.2(b), predict similar velocity profiles. In the case of the standard model without any modifications, they predict a fully symmetric velocity profile which renders them more or less useless in these cases. Adding the modification to the k-equation gives quite a large shift in turbulent kinetic energy, see later figures. However, without any modification to the length-scale equation (ω, ε), the asymmetry of the velocity profile becomes too small. If instead the length-scale equation is modified, the velocity profile agrees with the DNS data more closely, although the slope of the velocity profile in the center of the channel is somewhat off. The slope of the velocity profile is connected to the stability criteria and is thus an important parameter. Neutral stability is found where $Ri = 0$, see Johnston *et al.* [26], which is equivalent to the $2\Omega - du/dy = 0$ – found as a part of the numerator in

the Richardson number definition.

The EARSM generally predict the slopes rather well, see Fig. 10.2(c), although they predict too high a laminarization process on the stable side, although the near-wall behavior ($u_{\tau s}$) is rather close to the DNS data in most case, see table above. Changing the pressure-strain model causes only a very slight change in the velocity profile or the friction velocity. Neither does substituting the length-scale equation from ω to ε make any great difference in the velocity profile. Using the Wallin and Johansson EARSM instead of the Gatski and Speziales EARSM alters the velocity profile so that it is greater agreement with the DNS data. However, the only way to predict very good agreement is to add a Richardson number modification to the length-scale equation as can be seen in Fig. 10.2(d). In this figure, the Richardson number modifications[27] added to the EARSM(GS) $k-\omega$ and $k-\varepsilon$ were compared. All three do a fairly reasonable job, although only the EARSM yields the correct slope of the velocity profile. The velocity profile is the most important parameter in any engineering flow and is of great value when discussing the turbulence models. Still in order to quantify the turbulence models, a turbulent quantity is necessary. In this case, the turbulent kinetic energy was chosen, although the shear stress or some other Reynolds stresses could also have been chosen.

The turbulent kinetic energy profiles, normalized with the friction velocity, $k(y)/u_\tau^2$, are shown in Fig. 10.3. The figures are oriented in the same way as the velocity profiles, and thus the stable (laminar=low k) is found at $y=+1$ and the unstable (turbulent=high k) side is found at $y=-1$. The first striking discrepancy is the awful prediction of k using the modified k-equation in both the EVMs in Figs. 10.3(a) and 10.3(b). Almost equally bad is the k-profile using the non-modified EVM, which is once more fully symmetric around the centerline of the duct. By adding the simple Richardson number modification, the k-profiles improves quite a bit and there is a larger deviation only close to the walls. On the unstable side, both models fail to predict the peak in turbulent kinetic energy, although with fairly good agreement overall. The agreement is less good on the stable side, where the k-level away from the wall drops too low. Comparing the two EVMs, it seems that the $k-\omega$ model is more suitable as a basis, since the wall condition of the ω-equation captures some of the turbulent kinetic energy on the laminar side whereas the $k-\varepsilon$ fails to yield any turbulence at all on the same side.

Moving on to the EARSM, Fig. 10.3(c), the three EARSM(GS) do not greatly change the symmetric profile of the standard EVM which can be explained by the rather small anisotropy values captured by these models. Since the model is constructed in such a way, that only small anisotropy values are allowed, it is only reasonable to achieve a slightly asymmetrical profile of the turbulent kinetic energy. What can be observed is once more that the pressure-strain model is less important than the EVM on which the EARSM is based. A comparison of the EARSM(GS) and the EARSM(JW), shows some larger differences. The EARSM(JW) is able to capture more of the re-laminarization process on the stable side, and the peak on the unstable side is a bit higher. However, it is necessary to add the Richardson number modification to the EARSMs as well to reach satisfactory agreement, which can be observed in Fig. 10.3(d). From this figure, it is completely clear that the most important change is the Richardson number modification, because the difference between the EARSM(GS)-$k-\omega$ mod ω and $k-\omega$ mod ω is very small. It can also be observed that the length-scale equation affects the prediction, especially close to the walls. This is most likely an effect of the difference in boundary condition of the ω

[27] That is, modifications to the length-scale equation, ω or ε.

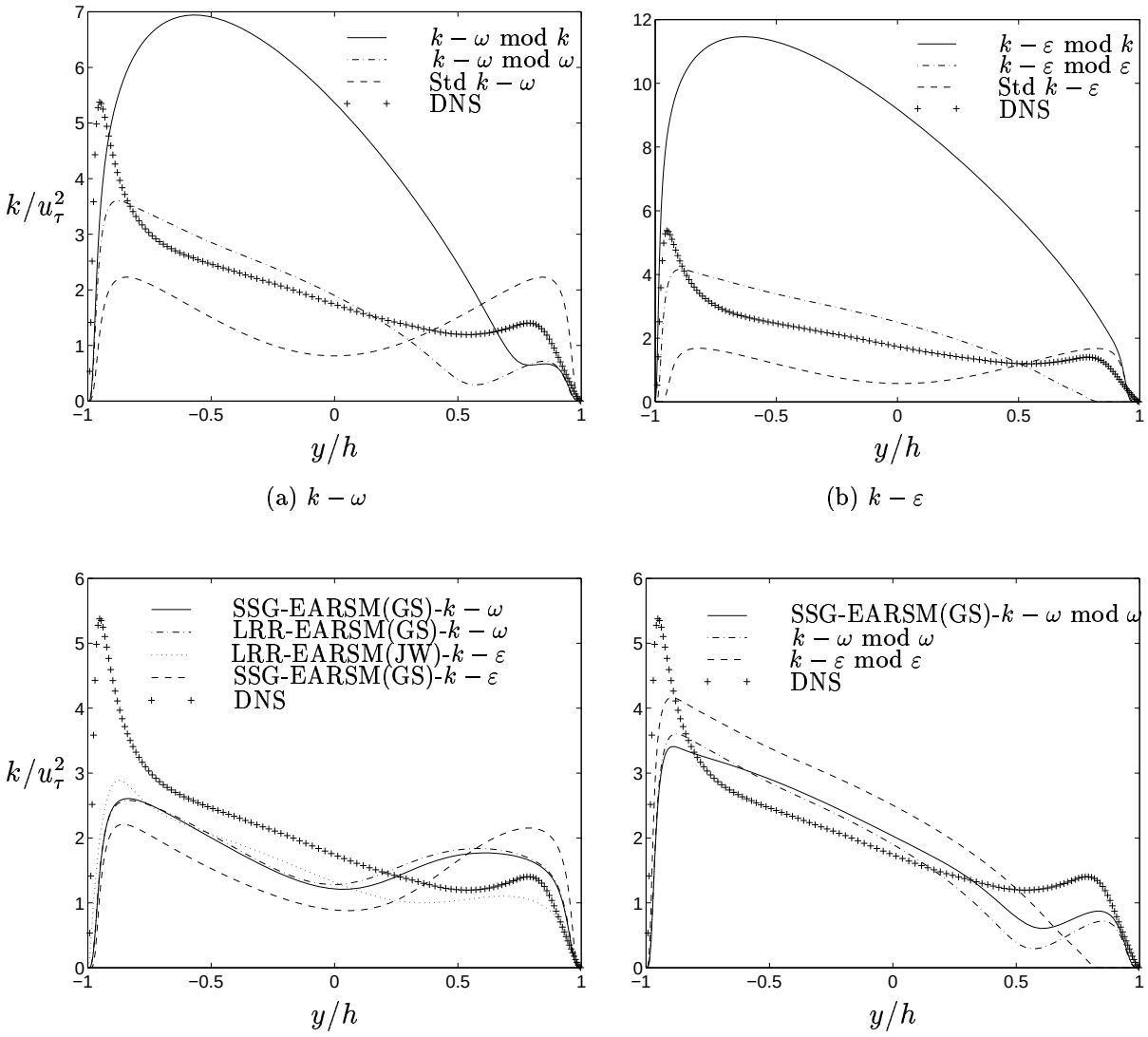

(a) $k-\omega$ (b) $k-\varepsilon$

(c) EARSM (d) Mod ε,ω-Eq.

Figure 10.3: Turbulent Kinetic Energy, Rotating 2D-duct

and the ε. The $k-\varepsilon$ gives overall higher k-levels than the $k-\omega$ apart from on the stable side, where the solution fully laminarizes in disagreement with the DNS data.

10.2.2 Johnston, $Re_H = 11.500, Ro_H = 0.21$

In addition to comparisons with the above DNS data, some of the turbulence models were tested against an experiment by Johnston *et al.* [26] that used a higher Reynolds number. This was done because it was feared that the DNS data were achieved for too low an Re-number making the value questionable. The Reynolds number based on the channel height for the experiment done by Johnston *et al.* is $Re_H = U_m H/\nu = 11\,500$, with a rotational number very close to that above, $Ro_H = 0.21$. The computational mesh was similar to that for the DNS comparison, although with a more stretched 30×100, grid allowing the first node to be within $y^+ = 1$ for this higher Reynolds number case.

Starting with the $k-\omega$ based modifications, see Fig. 10.4(a), the $k-\omega$ with a

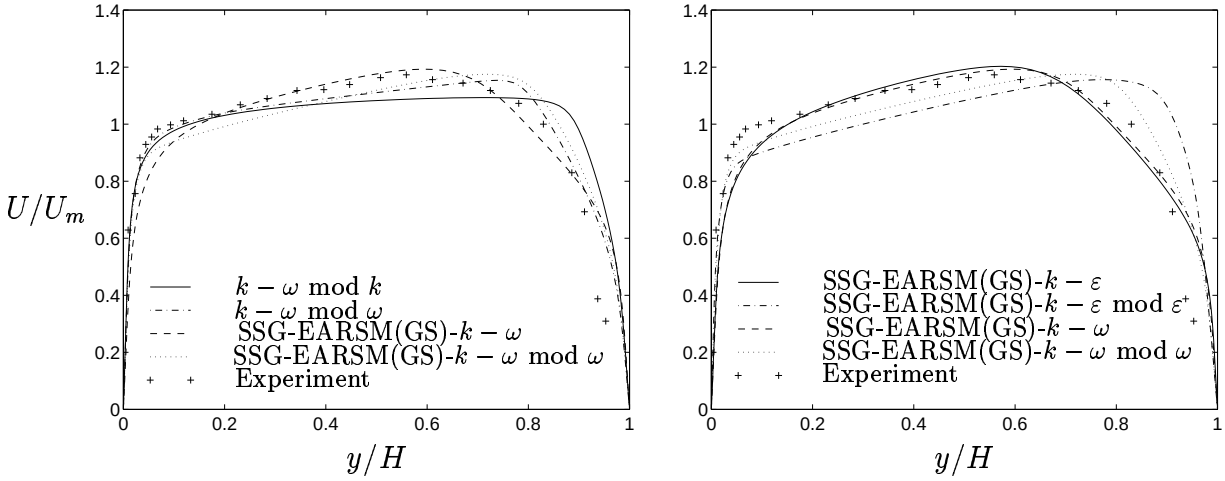

(a) $k-\omega$ based modifications

(b) EARSM based modifications

Figure 10.4: Velocity Profiles, Rotating 2D-duct

modified k-equation does the worst job, although it is of course slightly better than the non-modified $k-\omega$, which predicts no modification at all due to rotation. (This model is not included in the figure.) Once more, the EARSM seems to be needed in order to capture the correct slope of the velocity profile in the center part of the channel. Focusing on the stable side of the channel, where the largest discrepancies are found, the standard EARSM yields too low a value around $y/H = 0.8$, where the two Richardson number modified models over-predict the streamwise velocity. Further to the center, the EARSM starts to over-predict, while the two Richardson number modified models under-predict. In the center part of the channel, the EARSM with Ri-mod under-predict all the way with a correct slope, while the $k-\omega$ mod ω has too gentle a slope and achieves values closer to the experiment on the unstable side of channel. The $k-\omega$ mod k, which has the flattest slope, also comes very close to the experiment on the unstable side, although the prediction overall is rather poor. The two EARSM under-predict on the unstable side but in general agree well with the experimental data, and whether the Ri-modification should be used or not is open to discussion.

Fig. 10.4(b) compares the Gatski and Speziale EARSM with the SSG pressure-strain model based on either the $k-\omega$ or the $k-\varepsilon$ EVM. As can be observed in the figure, the non-Richardson-number modified EARSM predicts more or less the same velocity-profile independent of the EVM, which is in contrast to what was found from the lower Reynolds number predictions. There are some slight differences – but they are much smaller than for the low Reynolds number case. Adding the Richardson modification to the length-scale equation reveals a much larger difference between the two EVMs. Both get the correct slope, but the $k-\varepsilon$ more severely over-predicts on the stable side than does the $k-\omega$, indicating too low a value for turbulent production. In the center part, the $k-\varepsilon$ under-predicts more severely than the $k-\omega$, and thus it can be concluded that the $k-\omega$ based EVM is more suitable for this Richardson number modification.

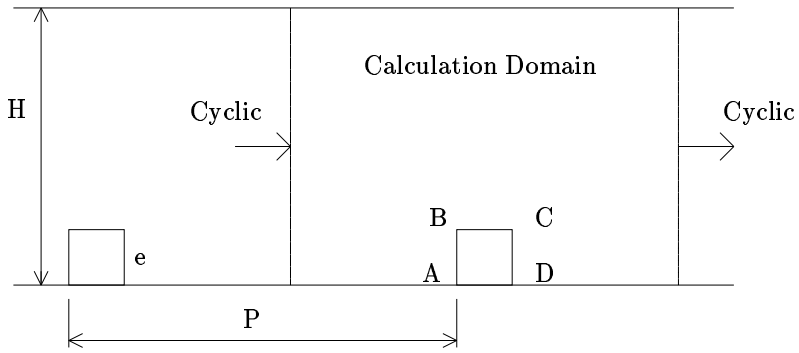

Figure 10.5: Geometry of 2D Ribbed Channel

10.3 2D Ribbed Channel

This section gives a number of different test cases, all with a schematic configuration as shown in Fig. 10.5. All of the below test cases have a rib attached to the lower wall to enhance the heat transfer through an increase in turbulence level. The geometrical condition from test case to test case varies slightly, with the blockage effect from the rib being fairly small – less than 20%. Two different geometrical parameters are used in describing these test cases:

- P/e, the pitch-to-rib height ratio. This is the distance between two repeating ribs over the side length of the rib.
- e/H, the rib height-to-channel height ratio. This is the side-length of the rib over the channel height (non-blocked).

It should be noted that all ribs are of a square cross-section, i.e. the rib length is equal to the rib height. In addition, the ribs are used normal to the streamwise flow. Apart from these geometrical parameters, the most important flow parameter is the Reynolds number. In this section, all of the computations are made on a two dimensional mesh with a symmetric boundary condition in the z-direction[28]. This would relate in the physical world to an infinitely wide channel, which naturally does not exist. Depending on how the experiments are done, this condition is more or less fulfilled. The computation is made with a periodic boundary condition, where essentially all variables are cycled from outlet to inlet. This is the same as computing a fully developed flow, where all disturbance from any inlet is neglected. In the case of a ribbed channel, the fully developed regime occurs after a few rib intervals [16] and was achieved in all experiments.

The periodic boundary condition is both advantageous and disadvantageous from a computational point of view. The advantage is that the initial flowfield is unimportant for the converged solution. The disadvantage is that the convergence rate is slower because of the trial-and-error iteration scheme for the unknown pressure gradient coefficient, β, through the channel.

The general characteristics of the flow through these 2D ribbed channels can be viewed in Fig. 10.6. This figure is taken from the computation of the Rolls-Royce case with the medium mesh and the Peng *et al.* turbulence model. Fig. 10.6(b) shows the flowfield just upstream of the rib. What is notable in this picture is the small re-circulation bubble on top of the rib behind the upper upstream corner. This is produced by the separation

[28]The streamwise direction is the x, the wall normal is y and z is the third symmetric direction.

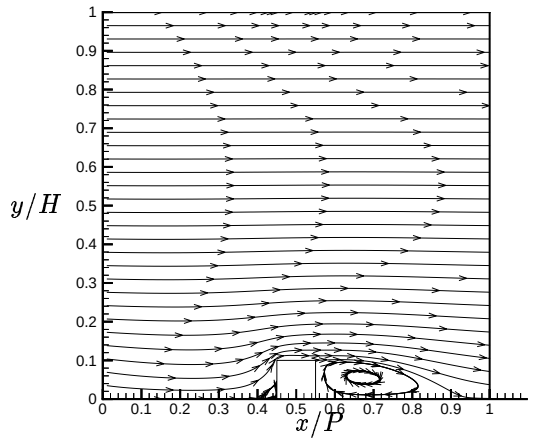

(a) Whole channel

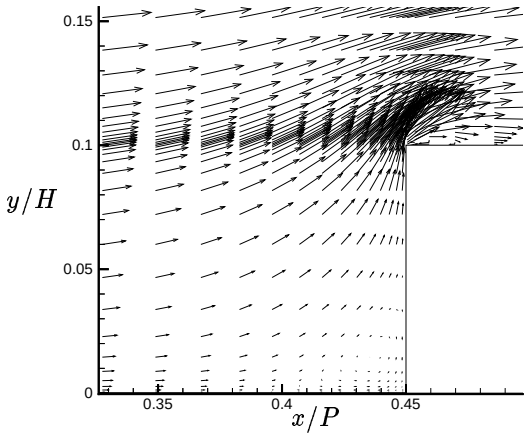

(b) Upstream of the rib

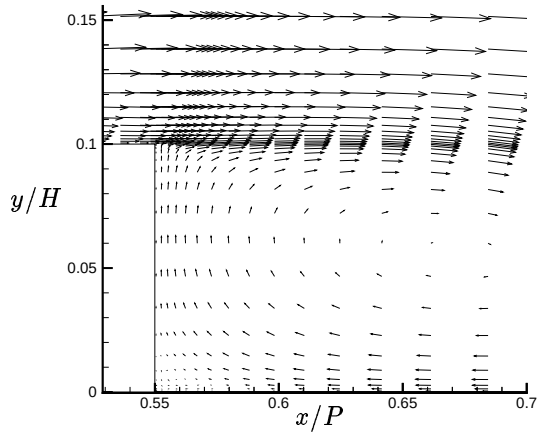

(c) Downstream of the rib

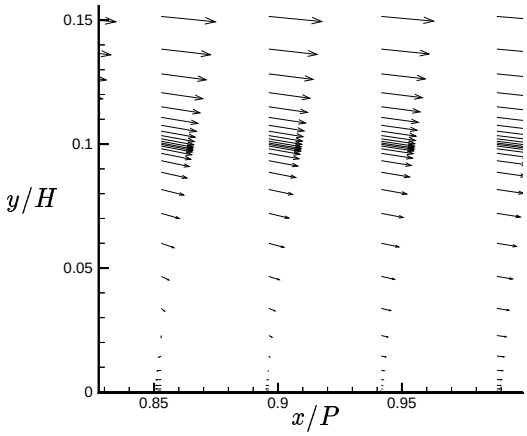

(d) Re-attachment point

Figure 10.6: Flowfield, Rolls-Royce 2D Ribbed Channel

from the corner and, depending on the turbulence model, the length of this re-circulation bubble varies. Not as clearly visible is the small re-circulation bubble in front of the rib, which can also be seen in Fig. 10.6(a). The rib acts as a blockage for the flow, forcing the fluid to separate from the lower wall some distance upstream of the rib, producing this re-circulation zone. Moving to the downstream side of the rib in Fig. 10.6(c), the upstream half of the large re-circulation bubble is visible and, furthermore, a counter-rotating smaller bubble is observable near the lower downstream corner of the rib. The re-attachment point depends on the turbulence model and, in the case of Peng *et al.*, this is close to $x/P = 0.95$, according to the pictures, which is equivalent to 4.5 step heights downstream of the rib. A close-up of the flow around the re-attachment point is shown in Fig. 10.6(d). The separation and re-attachment points are not very easy to detect from a visualization of only the flowfield according to Fig. 10.6. To capture these points

accurately, some other parameters are needed. One of these has in fact already been presented in the section regarding meshes and grid-independency. This section discussed the importance of the near-wall y^+ values for the cell nodes. In the definition of the y^+, the friction velocity at the wall, u_τ, is used in the numerator. Whenever the flow separates or re-attaches, the friction velocity is zero at the wall, and hence the y^+-value is zero. Re-capturing the y^+ values for the medium mesh for the Peng *et al.* turbulence model, Fig. 9.3(b), in Fig. 10.7 more clearly indicates the separation and re-attachment points.

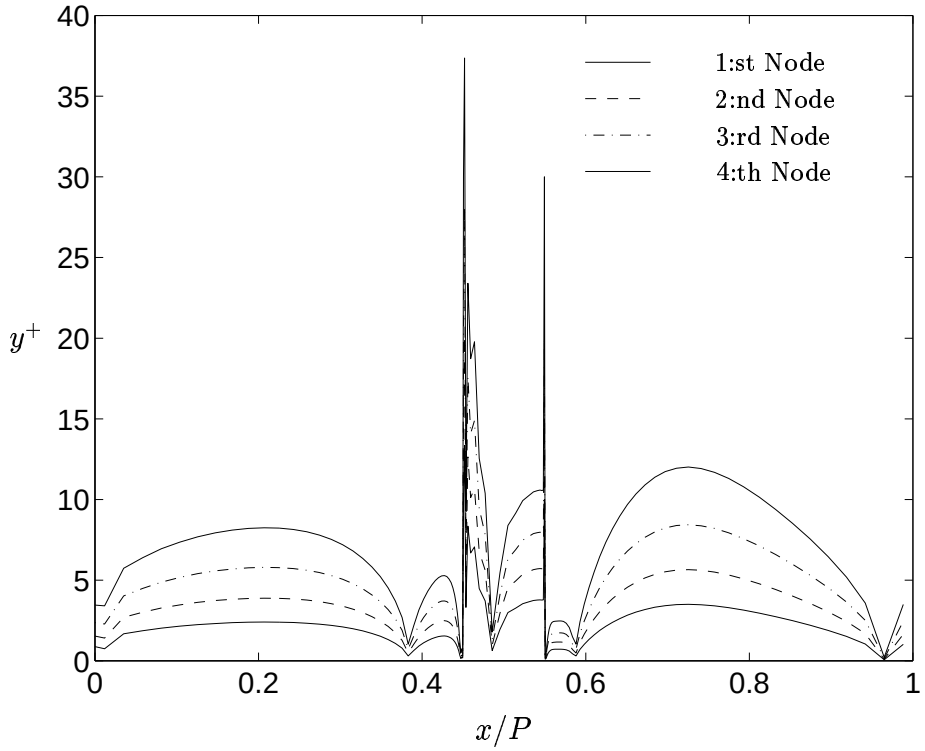

Figure 10.7: y^+, Rolls-Royce 2D Ribbed Channel

All the above discussed separation and re-attachment points are visualized through the y^+ values in a very neat way. From this picture, the re-circulation bubble in front of the rib can be estimated to be $x/P = 0.08$ long, while the smaller counter-rotating vortex behind the rib is somewhat smaller. The re-circulation bubble on the rib top measures roughly 35% of the rib length for this turbulence model. The above figures were shown only to visualize the flowfield, and this is neither the time or place to make a similar graphical presentation of the four turbulence models in the above Rolls-Royce case nor in all the test cases below. This detailed analysis of the flowfield will be resumed only when there is adequate experiment data with which to make comparisons, e.g. in the Drain & Martin(F) case.

10.3.1 Rolls-Royce, $Re_H = 122\,400$

The first obvious test case to be presented is the Rolls-Royce case, which has already been discussed in some detail above. The test case is denoted Rolls-Royce since the experiment was performed at Rolls-Royce, but the experimental data for this report were taken from the paper by Iacovides and Raisee [24]. The Reynolds number based on the channel height is $Re = 122\,400$, and the geometrical conditions are a pitch-to-height ratio

of $P/e = 10$ and a height-to-height ratio of $e/H = 0.1$, indicating a blockage factor of 0.1. The experiment was set up with heaters along the lower wall, including the bottom face of the rib. This is the same as having a constant heat flux through the wall and was implemented in the code. The upper wall was set to be adiabatic. The computations were made on three different meshes, coarse: 55×60, medium: 110×120 and fine: 140×180. The grid independence check can be seen in Fig. 9.2, and from this it can be concluded that the medium mesh gives detailed enough results and is thus used in the results below. The four different turbulence models used for this test case are: Peng *et al.* $k - \omega$ [43], Abid *et al.* $k - \omega$ [2], Chen and Patel zonal $k - \varepsilon$ [7] and the EARSM of Gatski and Speziale [13] using the $k - \omega$ of Abid *et al.*. The only available data from the experiment is the Nusselt number along the lower wall. Around the rib, only the Nusselt number at the rib top was measured. In Fig. 10.8, the Nusselt number for the different turbulence models is compared with the experiment made at Rolls-Royce. In the figure, the rib is positioned between $x/P = 0.45$ and $x/P = 0.55$, i.e. in the center of the computation, as seen in Fig. 10.5.

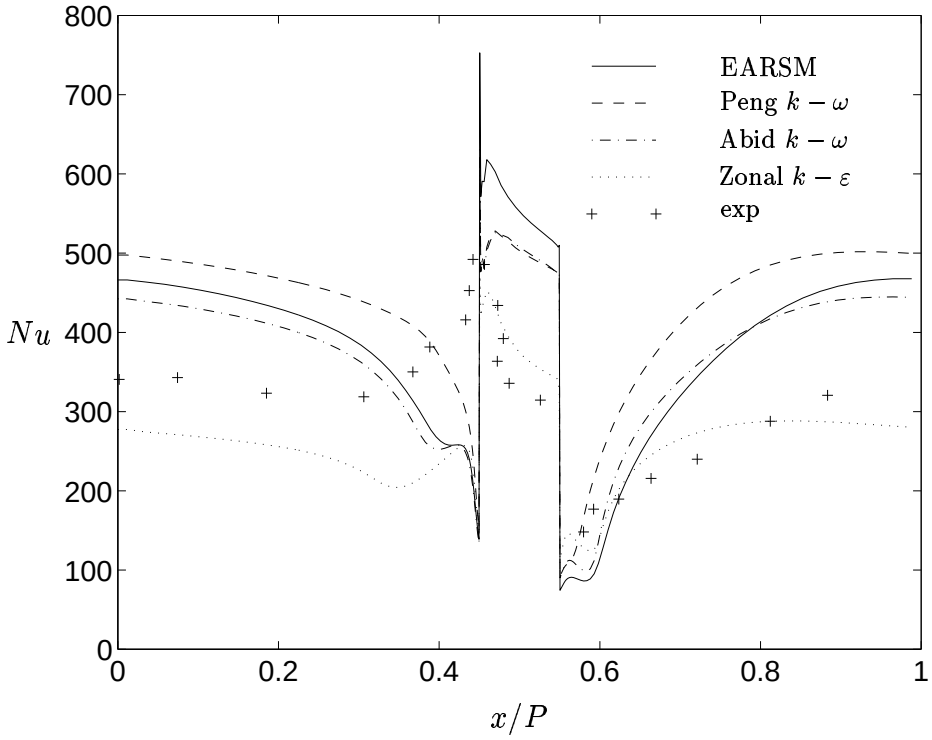

Figure 10.8: Nusselt Number, Rolls-Royce 2D Ribbed Channel

The two $k - \omega$ turbulence models predict similar behavior throughout the channel. Both models over-predict the Nusselt number, apart from just upstream of the rib, where a slight difference in the profile of the Nusselt number can also be observed between the models. In the mid-interval between the ribs, the Abid *et al.* model gives an over-prediction of roughly 30%, while the Peng *et al.* over-predicts by as much as 50%. On the rib top, the two models give almost identical results, with a fairly large over-prediction. The reason why the Peng *et al.* gives higher values of the Nusselt number should be traced to the low-Reynolds number formulation of that model and probably not to the extra cross-diffusion term that appears in the model. The Abid *et al.* $k - \omega$ is essentially a standard Wilcox $k - \omega$ model, which does not add any damping functions due to wall proximity, as the low-Reynolds number version of Peng *et al.* does.

The denotation high- and low-Reynolds number versions of the $k-\omega$ is somewhat unfortunate and does not correspond to the same denotation of the $k-\varepsilon$ models. A high-Reynolds number $k-\varepsilon$ usually refers to a model that uses wall-functions close to solid walls, while the low-Reynolds number version adds damping functions, which enables the model to be integrated to the wall. In the case of a $k-\omega$ model, both the low- and high-Reynolds number versions can be integrated to the wall – and the denotation indicates only whether or not any damping functions are involved.

The damping functions in the model of Peng *et al.* raise the turbulence level through a damping of the dissipation term in the k-equation close to the wall. Since the heat transfer is directly connected to the eddy viscosity through the heat transfer model, see Eq. 8.5, an increase in turbulence level inflicts an increase in heat transfer. This is visualized in Fig. 10.8 through the higher Nusselt number for the Peng *et al.* $k-\omega$ model than the Abid *et al.* ditto. This was also observed by Peng *et al.*, which noted that the standard Wilcox $k-\omega$ [56] – which is essentially identical to the Abid *et al.* model – quite severely under-predicts the near-wall profile of turbulent kinetic energy, [43].

Comparing the EARSM with the Abid *et al.* $k-\omega$ enables us to estimate the influence of non-isotropic Reynolds stresses in the 2D ribbed channel. As can be seen in the figure, the EARSM generally raises the Nusselt number as compared with the isotropic and linear EVM, apart from in the re-circulation region behind the rib. Overall, the differences are slight and in any case move the predictions away from the experiment. The only notable improvement is the more gentle rise after the rib, which is in agreement with the experiment. It should however be noted that the EARSM of Speziale and Gatski does not predict high levels of anisotropy, and thus a great deviation from the EVM $k-\omega$ would be unlikely.

The last turbulence model, the zonal, or two-layer $k-\varepsilon$ of Chen and Patel, differs quite a bit from the other three. Firstly, the overall predicted Nusselt number is much below the other three and also far below the levels found in the experiment. Apart from that, the main difference is in the upstream region of the rib, where the zonal $k-\varepsilon$ captures the physics from the experiment and raises the Nusselt number just in front of the rib, which the other three models fail to do. On the downstream part of the rib, the two-layer model raises the Nusselt number too quickly and then flattens out prior to what was found in the experiment. On the rib-top the predictions of this model agrees very well with the experiment.

Overall, the predictions of the zonal model are preferred, apart from some minor disagreement regarding the profile of the Nusselt number downstream of the rib, where the EARSM yields the most favorable result.

10.3.2 UMIST(a) and UMIST(b), $Re_H = 100\,000$ and $Re_H = 40\,000$

Both UMIST cases are treated in this section. They have identical geometrical conditions to each other and the above Rolls-Royce case, i.e. a pitch-to-height ratio of $P/e = 10$ and a height-to-height ratio of $e/H = 0.1$. The experiments were done by a M.Sc. student of Dr. Iacovides, Mr Nicklin [39] at UMIST (University of Manchester Institute of Science and Technology). The experiments were made in a channel of similar appearance as is shown in Fig. 10.5, with the rib located in the center part of the calculation domain on the lower wall. The Nusselt numbers were measured in this experiment, at both the upper and lower wall. Heaters were attached to both the lower and upper wall, introducing heat through a constant heat-flux boundary condition. The rib itself was isolated from the

heater, and thus a zero heat-flux was obtained over the rib. The experiments were made with two different Reynolds numbers, $Re_H = 100\,000$ and $Re_H = 40\,000$, both based on the channel height. In the predictions, the same mesh was used for both cases and measured 112×122. Three different turbulence models were used, the $k-\omega$ by Abid *et al.* [2], the EARSM by Gatski and Speziale [13] based on the above EVM and the zonal $k-\varepsilon$ of Chen and Patel [7]. The Nusselt numbers predicted with the three turbulence models are compared with the experimental data along the lower wall in Fig. 10.9.

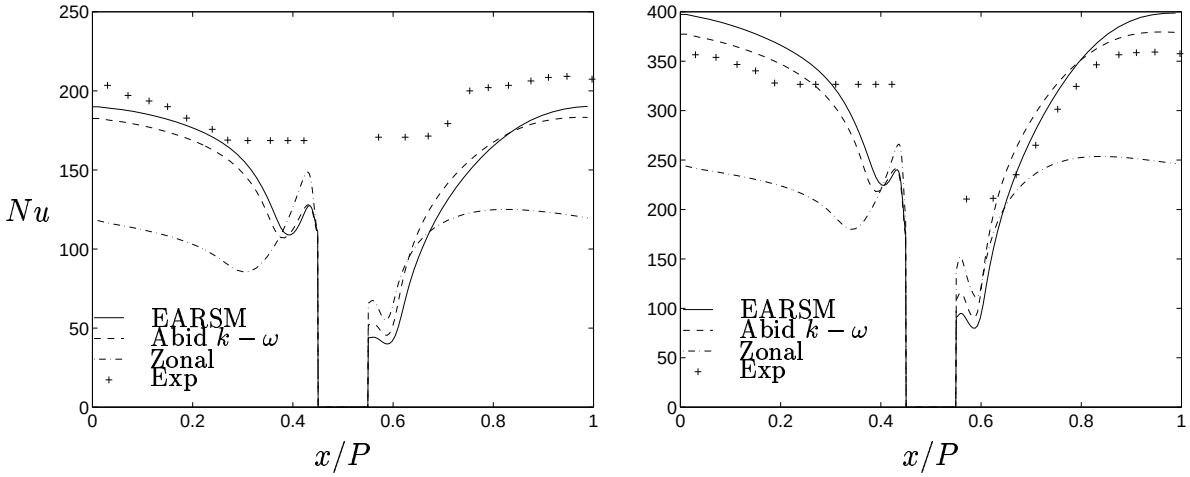

(a) $Re_H = 40\,000$ (b) $Re_H = 100\,000$

Figure 10.9: Nusselt Number, Lower Wall, UMIST 2D Ribbed Channel

Starting with comparing the results of the two experiments, the Reynolds number dependency of the Nusselt number can be clearly seen, where the increase from $Re_H = 40\,000$ to $Re_H = 100\,000$ gives rise to an increase in the Nusselt number of over 50%. In a flat plate with uniform heat-flux warming the flow, the Nusselt number dependency on the Reynolds number and Prandtl number for a large range of values was compiled into the Dittus-Boelter relation, given by McAdams [36] as:

$$Nu = 0.023 Re^{0.8} Pr^{0.4} \tag{10.1}$$

The ratio of the Reynolds number raised to 0.8 gives a factor of 2.08 in favor of the higher Reynolds number, which is more than is shown from these experiments, approximately 1.7 in the mid-range between the ribs.

Comparing the predictions obtained by the different turbulence models at the specific point of $x/P = 0$ and relating these to the experiment, the following table can be compiled:

	Experiment	EARSM	Abid $k-\omega$	Zonal
Nu(100k):	357	397	377	244
Ratio Pred/Exp:	-	1.11	1.06	0.68
Nu(40k):	204	190	183	118
Ratio Pred/Exp:	-	0.93	0.90	0.59
Ratio(100/40):	1.75	2.09	2.06	2.07

The rows are: the predicted/measured Nusselt number for the higher Reynolds number case, the ratio of the predicted Nusselt number with the measured, the predicted/measured

Nusselt number for the lower Reynolds number case, the ratio of the predicted Nusselt number with the measured and, finally, the ratio of the predicted/measure Nusselt number for the higher to the lower Reynolds number. A very interesting point is the last row, where all models yield exactly the same ratio as the Dittus-Boelter relation, Eq. 10.1 for a flat plate. The experiments show a much lower dependency on the Reynolds number, which is equivalent to: $Nu \sim Re^{0.61}$, close to the $Nu \sim Re^{2/3}$ found by Richardson [47] in similar configurations.

Apart from the difference in the level of the predicted Nusselt number for the two Reynolds number cases, the overall profiles of all turbulence models are the same for the low and high Reynolds number cases, as can be seen in Figs. 10.9(a) and 10.9(b).

The EARSM and the Abid *et al.* $k-\omega$ model have very similar results, which also agree rather well with the experiments. The largest deviation is behind the rib, where the turbulence models predict too large a drop in the Nusselt number, which could not be found from the experiment. It should be noted however, that for $Re_H = 100\,000$ the experiment and the predictions indicate a more similar behavior than for the lower Reynolds number case, although the measured decrease in the Nusselt number is not nearly as large as those predicted. For the two $k-\omega$-based turbulence models, there is also a drop in the Nusselt number in the upstream region of the rib, although with an increase just in front of the rib. This variation in Nusselt number is not at all visible from the measurements.

In the case of the zonal model, the overall profile shows less agreement, especially upstream of the rib, where there is a relative large increase in Nusselt number prior to the rib, contrary to what is found in the experiments. In addition, the overall level of the Nusselt number is severely under-predicted in both cases. As for the Rolls-Royce case, the zonal model yields a rather flat profile in the mid interval between the ribs, with a maximum Nusselt number too close to the rib. In fact, the zonal model predicts the overall maximum Nusselt number just in front of the rib, which is clearly erroneous when compared with the measured data.

Switching to the upper wall, the differences between the turbulence models are very slight, as can be seen in Fig. 10.10.

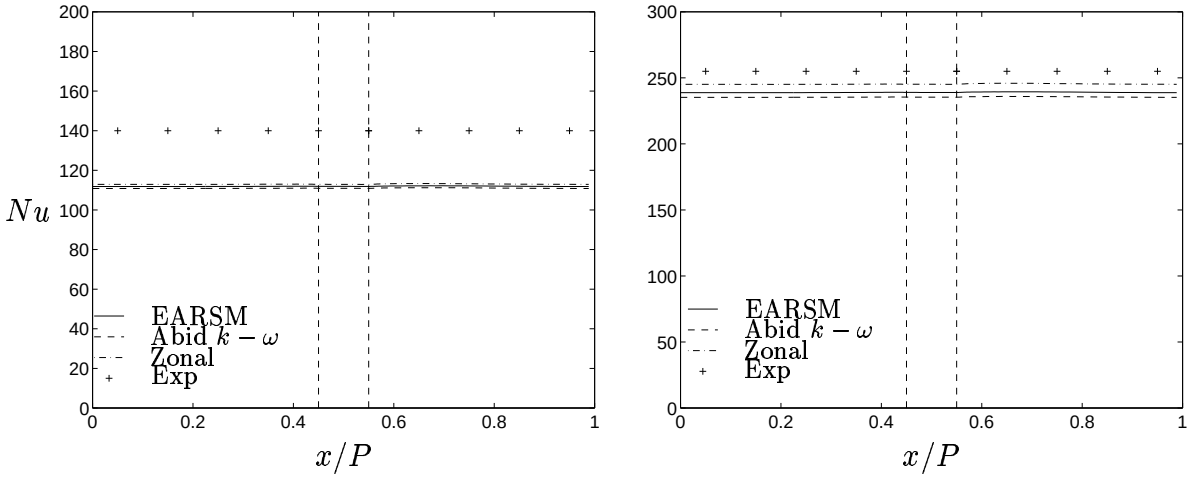

(a) $Re_H = 40\,000$ (b) $Re_H = 100\,000$

Figure 10.10: Nusselt Number, Upper Wall, UMIST 2D Ribbed Channel

All three turbulence models under-predict the heat transfer on the upper wall, more severely so for the low-Reynolds number case. In addition the small variation from the experiment can not be seen in the predictions, although this is most likely a defect in the measurements and should not be tried to be discussed with relevance to e.g. the position of the rib, which is graphically shown with two broken lines. In addition to the above calculations, the turbulence models were used to predict the Nusselt number in a smooth channel at the same Reynolds numbers. The results for the upper wall in the UMIST case and those for the smooth channel are compared with both the experimental data and the calculated Nusselt number with the Dittus-Boelter equation, Eq 10.1, in the table below:

	DB	Experiment	EARSM	Abid $k-\omega$	Zonal
Nu(100k):	199	255	160/239	161/235	171/245
Ratio Data/DB:	-	1.28	0.80/1.20	0.81/1.18	0.86/1.23
Nu(40k):	96	140	79/119	78/111	84/114
Ratio Data/DB:	-	1.46	0.81/1.24	0.81/1.16	0.88/1.19
Ratio(100/40):	2.04	1.82	2.03/2.01	2.06/2.12	2.04/2.15

The data in the table are given as, the first row: Dittus-Boelter (=DB) – Nusselt calculated for a flat plate using the Dittus-Boelter equation, Experiment – Nusselt number on the upper wall (non-ribbed) from the above experiment, EARSM #/# – the first number is the predicted Nusselt number with the EARSM for a smooth channel, and the second is the predicted Nusselt number for the upper wall in the ribbed channel. Similar notation for the Abid *et al.* model and the Chen and Patel zonal model. As in the previous table, the Nusselt number is given for both the higher and lower Reynolds number cases. However, here, the ratio is based on the Nusselt number given by the Dittus-Boelter (DB) equation instead of the experiment.

One can first note that, it is clearly so that the increase in the general level of turbulence by the ribs promotes the heat transfer on the non-ribbed wall as well. For the measured Nusselt number the increase for the upper non-ribbed wall in UMIST case compared with a smooth wall is 28% in the higher Reynolds number case and as much as 46% in the lower Reynolds number case. In the predictions the increase are roughly equal for both Reynolds number with between 43% and 49% for the higher Reynolds number case and between 35% and 50% for the lower Reynolds number case. The increase is highest with the EARSM and lowest with the zonal model. Furthermore, one can note that the $k-\omega$ based models under-predict the Nusselt number in smooth channels. This is associated with the fact that the standard $k-\omega$ models yield too low a value of the turbulent kinetic energy in the near-wall region, which hence affect the heat transfer to give a lower value.

For these two cases, a number of specific detailed near-wall data are plotted below. These are the streamwise velocity, U, the turbulent kinetic energy, k, specific dissipation, ω, and the total viscosity $\nu_{tot} = \nu_t + \nu$. Since there are no experimental data, these figures can be discussed only with relevance to each other, and no conclusion as to which set of data is the correct one can be made. Despite the lack of any measured data, there are some benefits in making the comparisons below. The turbulence model chosen for these comparisons is the Abid *et al.* $k-\omega$. Apart from comparing the two Reynolds numbers, the predictions have been made with a different boundary condition for the ω equation. The ω is either fixed only for the first node or for the first two nodes. The influence of this boundary condition can then be seen on the different parameters.

The flowfields for the two Reynolds numbers are shown in Fig. 10.11. There is only a very small change in the flowfield between the two Reynolds number, where the higher Reynolds numbers case yields a re-attachment point further upstream. A streamline is plotted in both Reynolds number cases which starts on the upper downstream corner of the rib and is then allowed to follow the flowfield. The streamline almost re-attaches for both cases, more closely for the higher Reynolds number case. This can be explained through the boundary layer, which in the higher Reynolds case is thinner and thus produces more turbulent kinetic energy, see Fig. 10.13 later in this section. This higher level of turbulent kinetic energy increases the exchange of momentum between the shear layer and the re-circulation region, which moves the re-attachment point further upstream. Argumently the difference is very slight. However, the reasoning behind the variation in the predictions is fruitful, and it is comforting to know that the turbulence model behaves as physics demands.

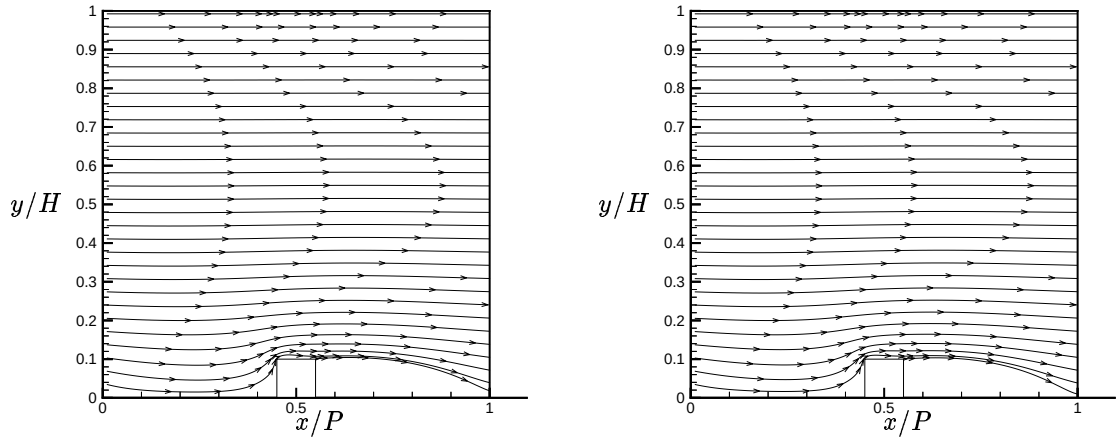

(a) $Re_H = 40\,000$ (b) $Re_H = 100\,000$

Figure 10.11: Streamlines, UMIST 2D Ribbed Channel

The data are extracted along certain x/P coordinates, where x denotes the distance from the LHS of the computation domain. In e.g. backward-facing step flow, an important quantity is the distance from the step height. For a ribbed channel, this would be equivalent to the distance from the downstream corner of the rib, which in this case is located at $x/P = 0.55$, since the rib is centered in the domain, as seen in Fig. 10.5. There are four different points where the data are compared, at $x/P = 0.75$, which is two step heights from the rib, $x/P = 0.95$ four step heights, $x/P = 0.05$ five step heights and, finally, $x/P = 0.35$, which is at eight step heights. For this case the main re-attachment point is located between $x/P = 0.95$ and $x/P = 0.05$, see Figs. 10.11(a) and 10.11(b). The first point is thus in the large re-circulation zone, and the last one is in the attached flow in front of the next rib.

The non-dimensionalized velocity profiles are shown in Fig. 10.12. First note the scale, where the ordinate covers only from the wall to $y/h = 0.007$, i.e. detailing only the very near-wall region. The first cell centers are located at: $0.0013, 0.0041, 0.0079, 0.013$, etc., see also the figure, where each node is indicated with a small jerk in the profile.

Because we are looking at the flow in re-attachment regions, it is inappropriate to use y^+ values. However, if someone is more familiar with plotting near-wall quantities in y^+ values, these vary for the lower Reynolds case from 5 to 130, with slightly higher values for the $Re_H = 100\,000$ case. See also the grid-independence test, 9.3, where the y^+ values are plotted along specific grid-lines, owing to the orthogonality of the mesh along specific wall distances. There is obviously a fairly large difference between the two Reynolds number predictions, where a change in the size of the re-circulation bubble can be concluded from Figs. 10.12(a) and 10.12(b). The higher Reynolds number shifts the minimum velocity towards the wall, and moves the re-attachment point further upstream, as also can be seen in Fig. 10.11. There is only a very slight change in the mean velocity profiles due to the imposed boundary condition on the ω equation. The largest deviation is associated with the re-attachment point, where the case with ω fixed for two nodes yields a re-attachment point further downstream, which is best visible in Fig. 10.12(c) for $Re_H = 100\,000$ case.

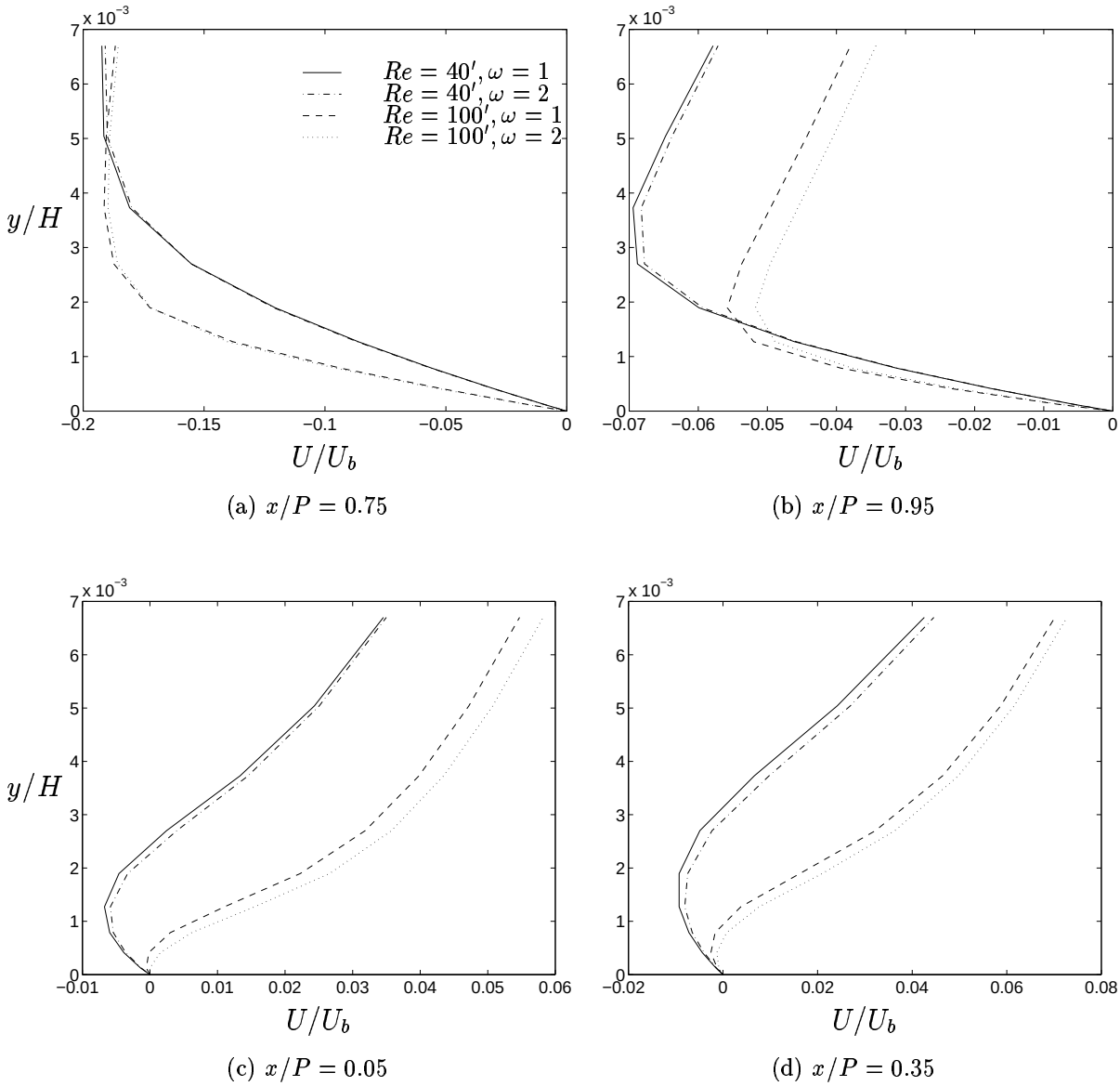

(a) $x/P = 0.75$

(b) $x/P = 0.95$

(c) $x/P = 0.05$

(d) $x/P = 0.35$

Figure 10.12: Velocity Profiles, UMIST 2D Ribbed Channel

To track some influence of the boundary condition for the ω equation, the turbulent kinetic energy, k, is plotted in Fig. 10.13. The first striking difference between the $Re_H = 100\,000$ and $Re_H = 40\,000$ case is that the higher Reynolds number case produces more turbulent kinetic energy. Apart from that, there is only a marginal difference between the cases with ω fixed for two nodes and those where ω is fixed for one node. When ω is fixed for two nodes there is slightly more turbulent kinetic energy, which indicates either less production of turbulent kinetic energy or more destruction of ω, i.e. higher ω values. To find out which is the case ω must be plotted as well.

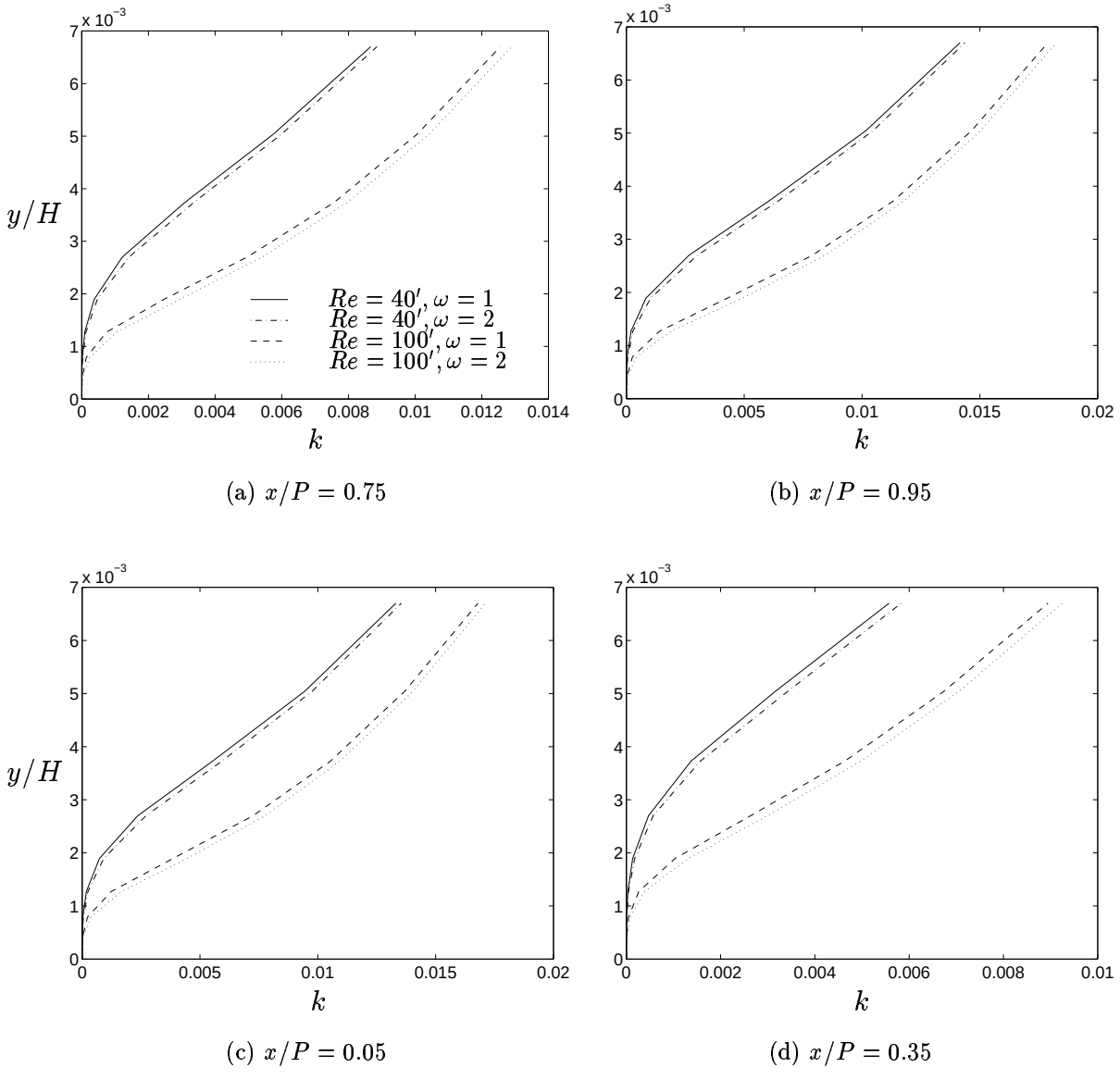

(a) $x/P = 0.75$

(b) $x/P = 0.95$

(c) $x/P = 0.05$

(d) $x/P = 0.35$

Figure 10.13: Turbulent Kinetic Energy Profiles, UMIST 2D Ribbed Channel

The non-dimensionalized specific dissipation rate (ω) is plotted in Fig. 10.14. It is non-dimensionalized with the viscosity and channel height according to: $\omega^* = \omega\nu/H^2$. Since the specific dissipation rate, spans such a vast range, it is favorable to use the logarithm as well besides the non-dimensionality

From these graphs it can be concluded that fixing two nodes reduces the near-wall specific dissipation rate, although only close to the wall – not including the fixed node(s),

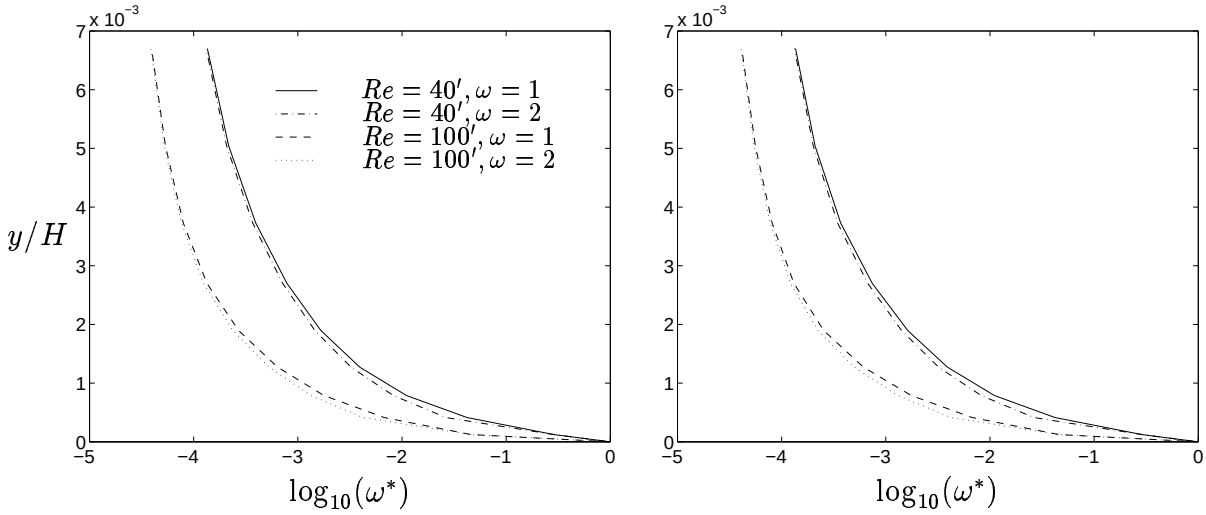

(a) $x/P = 0.75$ (b) $x/P = 0.95$

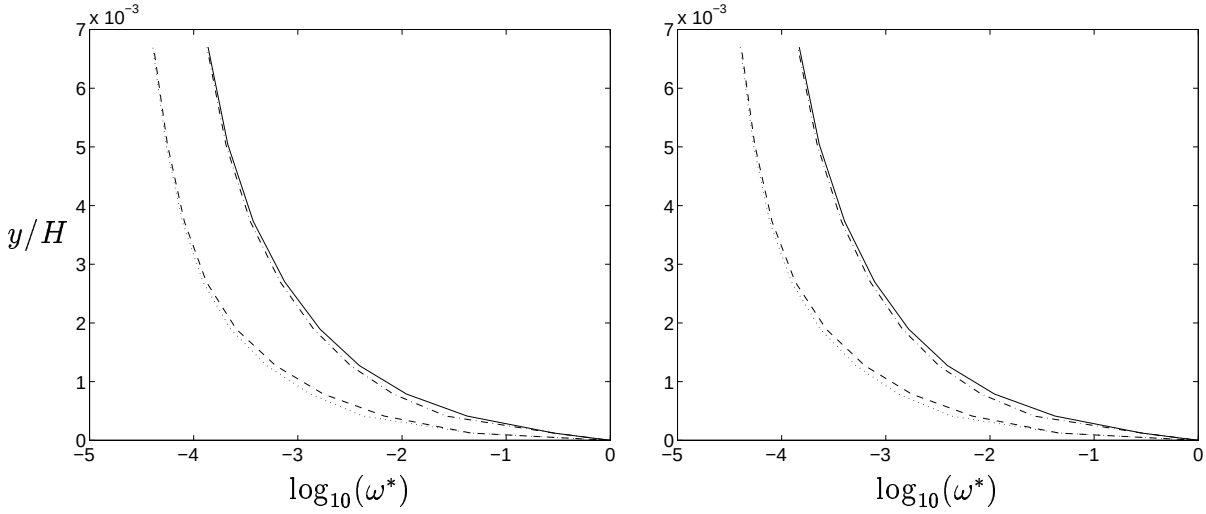

(c) $x/P = 0.05$ (d) $x/P = 0.35$

Figure 10.14: Profiles of Specific Dissipation, UMIST 2D Ribbed Channel

which is obviously identical. The reduction of turbulent kinetic energy is thus an effect of larger destruction and not less production. This could also have been assumed by looking at the velocity profiles, which indicate more or less equal gradients for either case, and hence the production should be equal. The reduction in the turbulent kinetic energy further away from the wall is however not a result of a local small specific dissipation rate, as seen in Fig. 10.14, but must be a result from a transport of k.

The parameter which effects the Nusselt number most is the viscosity. The viscosity profiles normalized with the molecular viscosity, according to: $\nu* = (\nu+\nu_t)/\nu$, is plotted in Fig. 10.15. The normalized viscosity is one at the wall, indicating zero turbulent viscosity. There is obviously a large difference between the high and low Reynolds number cases, where the higher Reynolds case produces much more turbulent viscosity through its higher turbulent kinetic energy. The difference is almost four-fold away from the near-wall region. The highest levels of viscosity occur around the re-attachment point, see Figs 10.15(b)

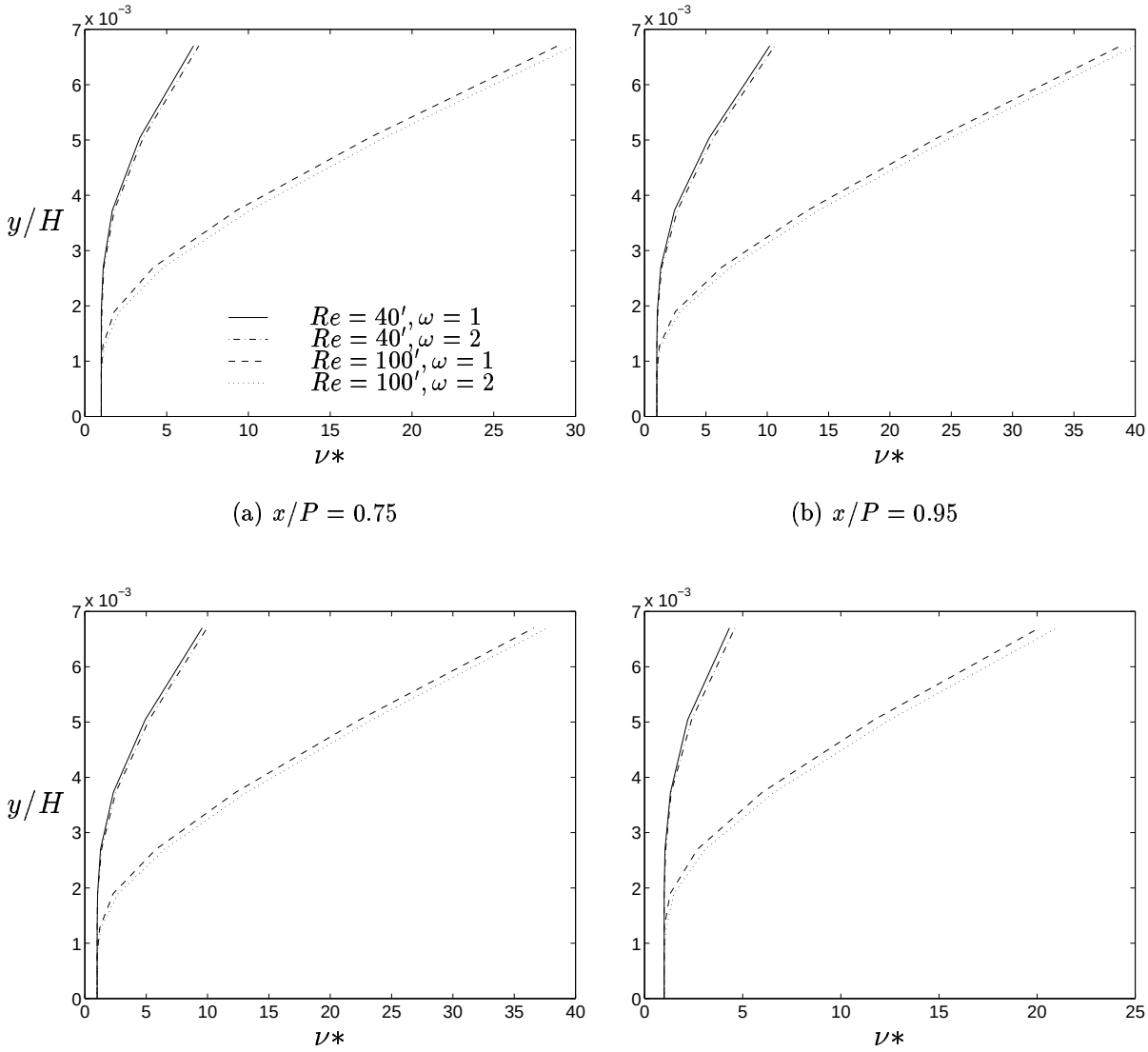

(a) $x/P = 0.75$

(b) $x/P = 0.95$

(c) $x/P = 0.05$

(d) $x/P = 0.35$

Figure 10.15: Near-Wall Viscosity, UMIST 2D Ribbed Channel

and 10.15(c). When comparing the one to the two node fixed boundary condition for the ω, it can be seen that the predictions in which the ω is fixed to two nodes produce the highest level of viscosity, although the difference is very small. It is revealing to compare the viscosity predictions with the Nusselt number predictions, since the latter is directly affected by the viscosity. Thus, in addition to being presented in the table on page 75, data from the predictions with Abid's *et al.* $k-\omega$, and fixing only the first node, are also shown in the following table:

	Experiment	Abid $k-\omega$ $\omega = 1$	Abid $k-\omega$ $\omega = 2$
Nu(100k):	357	362	377
Nu(40k):	204	179	183

The small difference in the viscosity for the lower Reynolds number case is directly shown in the comparable Nusselt number predictions, and likewise for the higher Reynolds number case, where the viscosity for the two predictions departs more and hence yields a

larger difference in the Nusselt number. While it can be concluded from this that the importance of the boundary condition increases with the Reynolds number, this is not entirely true. On the basis of earlier findings, it is more correct to state that: if the mesh permits only a small number of nodes to be within, say, $y^+ < 10$, then it is more important to fix two to three nodes for the ω boundary equation. On the other hand, if there is no limit to the number nodes in the near-wall region, then it is irrelevant whether one, two or seven to ten nodes is fixed in the case of predicting heat transfer. There is obviously a little sway in this statement; if only a few nodes can be afforded in the near-wall area, then how should two to three nodes be fixed with Eq. 9.4, which is only valid for $y^+ < 2.5$? There is no good answer to this, which is a problem associated with the $k-\omega$ equations. Generally it is better to fix two nodes than to be terrified of the condition that fixed nodes should be within $y^+ = 2.5$. Note also the y^+ values of the first nodes in Fig. 9.3 and compare with the predictions in Fig. 9.2.

10.3.3 Baughn and Yan $Re = 50\,000$

The Baughn and Yan test case differs from the above cases in two important matters: the geometrical parameters is changed and there are ribs on both the upper and lower walls. The Baughn and Yan [3] case has a smaller rib as compared to the channel height, with a height-to-height ratio of $e/H = 0.0625$. However, as there are ribs on both sides that stand opposite each other, the effective blockage effect is larger, 13.5%. The pitch-to-height is however the same $P/e = 10$, as in the above test cases. The Reynolds number based on the channel height is: $Re_H = 50\,000$. Owing to the symmetry condition in this test case, it is legitimate to perform the calculation on only half the channel. In these predictions, the lower half was chosen with a symmetry condition applied on the centerline. Thus, with this simplification, even this case can be treated with the general appearance of the calculation domain as in Fig. 10.5. Due to the symmetry line on the upper part of the calculation domain, this test case is very numerically efficient to calculate, since there is only need of mesh refinement near the lower wall. The mesh used in the predictions displayed is: 112×82, which doubles in the y-direction for the full channel. The turbulence models used in this test case are the same as in the previous test case, thus: $k-\omega$ by Abid *et al.* [2], the EARSM by Gatski and Speziale [13] based on the above EVM and the zonal $k-\varepsilon$ of Chen and Patel [7]. The heat-flux in the experiment was applied as for the Rolls-Royce case, with a heater along the lower (and upper) wall. The rib was made of highly conductive material transmitting the heat-flux to the flow. In the predictions, this was simulated with equal heat-flux from the three faces of the rib. Due to the uniform heat-flux and continuity[29], the heat-flux from the faces of the rib was set to $q_{face} = q_w/3$.

Since the geometry condition is changed, it is interesting to display the flowfield from this calculation. Fig. 10.16 depicts the predictions with the $k-\omega$ model. The variation in the different turbulence models is very slight, and hence it is sufficient to compare only one of the turbulence models; the Abid *et al.* model is chosen along the line of the above UMIST test case choice. Fig. 16(a) shows the streamlines; notable is the increased re-attachment length with this smaller rib, where the re-attachment point is found at 5.5 step heights downstream the rib. This can be compared with Fig. 10.11 – the UMIST case – where the re-attachment point is located at 5.2 for the $Re_H = 40\,000$ case and 4.9 step heights for the $Re_H = 100\,000$ case. Fig. 10.16(b) plots the velocity vectors on the

[29]The sum of the heat-flux from the faces must be equal to that through the base area.

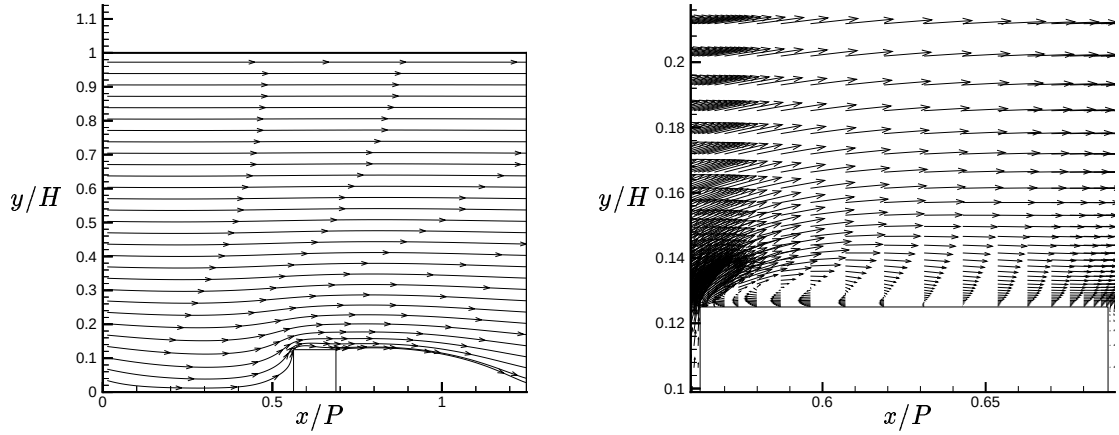

(a) Streamlines

(b) Detail of rib-top

Figure 10.16: Flowfield, Baughn and Yan 2D Ribbed Channel

top of the rib. The re-circulation bubble from the upstream corner of the rib increased from roughly 0.3 rib lengths in the Rolls-Royce case, see Fig. 10.6(b), to 0.6 rib length in this case.

The Nusselt number along the lower wall, including the rib top for the turbulence model and the experiment, is depicted in Fig. 10.17. The general trend from the previous test cases is repeated. The EARSM and the $k-\omega$ have a similar profile as the experiment, while the zonal model deviates somewhat. All models overall yield too low a Nusselt number, and much more so for the zonal model.

Comparing the $k-\omega$ with the EARSM, the EARSM predicts a slower increase of the Nusselt number downstream of the rib, in agreement with the experiment, and captures the right position of the peak heat transfer, although not the right level. The $k-\omega$ predicts the maximum Nusselt number earlier, with a quicker increase behind the rib. Upstream of the rib, both models predict a small bump, which could possible be traced in the measurement, although the predicted bumps are much larger with a predicted Nusselt number level below the measured.

The zonal predicts a rather large increase in the Nusselt number behind the rib, much more than the $k-\omega$ models, once more in disagreement with the experiment. Upstream of the rib, the bump predicted by the zonal model is larger with a higher predicted Nusselt number than is given in the $k-\omega$ model, although still below the measured.

The terrible part in this test case is the predicted Nusselt number on the rib top. None of the turbulence models are even close to capturing the values of the experiment. Even the profiles fail, although there is a small question regarding the validity of the experiment which can not be guaranteed.

The difficulties in measuring local heat transfer are well known and, although the appearance of the profile in the interval of the ribs looks fine, the very sharp gradients on the rib top could possible be a result of some measuring discrepancy. However, without a possibility to compare the velocity field on the rib top, it is difficult to speculate as to where the large predicted discrepancies originate. A reasonable guess is that the size of the re-circulation bubble on the rib top is severely under-predicted because – judging from

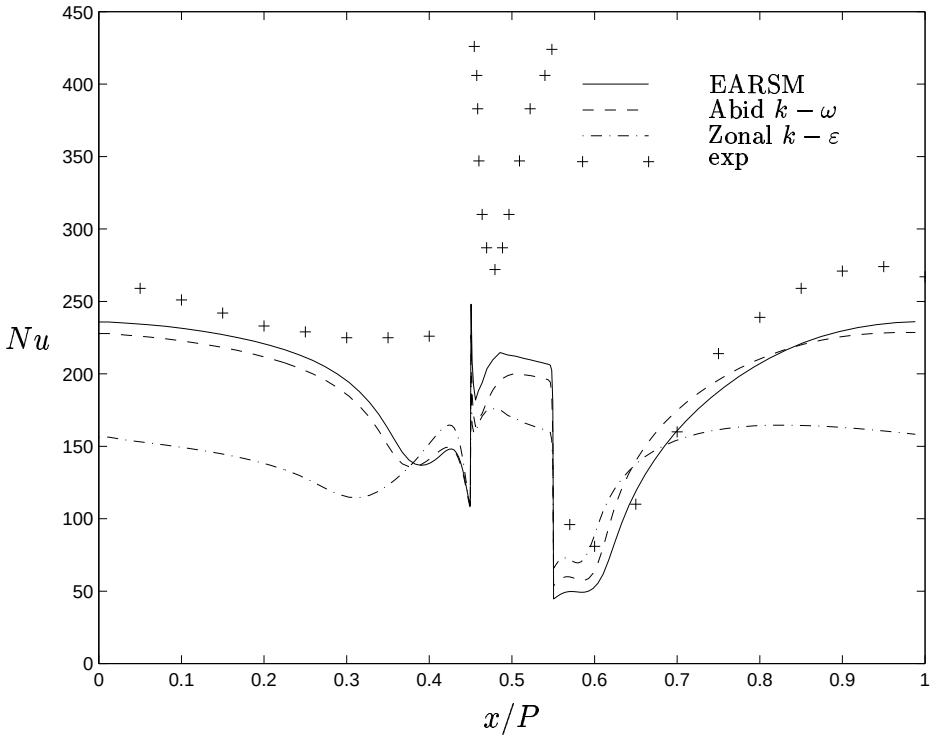

Figure 10.17: Nusselt Number, Baughn and Yan 2D Ribbed Channel

the measured Nusselt number – it should extend over the whole rib top, with a maximum heat transfer at the re-attachment point close to the downstream corner of the rib top. The predicted re-attachment point is roughly located at midway on the rib top, see Fig. 10.16(b). The high heat transfer level on the upstream corner of the rib top is a result of the separation and is captured in most test cases with the turbulence model, although it is generally over-predicted, and not under-predicted as in this case. Regardless of the results over the rib top can be trusted, the $k-\omega$ based model behaves rather well, with the EARSM achieving the best agreement with the measurements.

10.3.4 Drain and Martin Test Cases, $Re_D = 37\,200$ and $Re_D = 12\,600$

Drain and Martin [12] carried out two experiments, one in which they measured velocity profiles and the other where they measured the Nusselt number. The predictions from the different turbulence models are compared with the results of the former experiment in the section below, while the comparison with the latter experiment is made in the next section. The Reynolds number for the flowfield is $Re_D = 37\,200$, based on the hydraulic diameter[30], while the Reynolds number for the Nusselt number measurements is $Re_D = 12\,600$. The predictions were made with four different turbulence models: two $k-\omega$ models, one by Abid *et al.* [2], and the other one by Peng *et al.* [43], the EARSM by Gatski and Speziale [13] based on the above EVM and the zonal $k-\varepsilon$ of Chen and Patel [7]. Three different meshes were used, coarse: 84×72, medium: 84×122, and fine: 166×162. Only the medium mesh is used in the comparisons displayed below. A mesh-independent check with the Peng *et al.* $k-\omega$ model can be found in the paper by Bredberg and Davidson [6].

[30] Hydraulic diameter is twice the channel height for a 2D case.

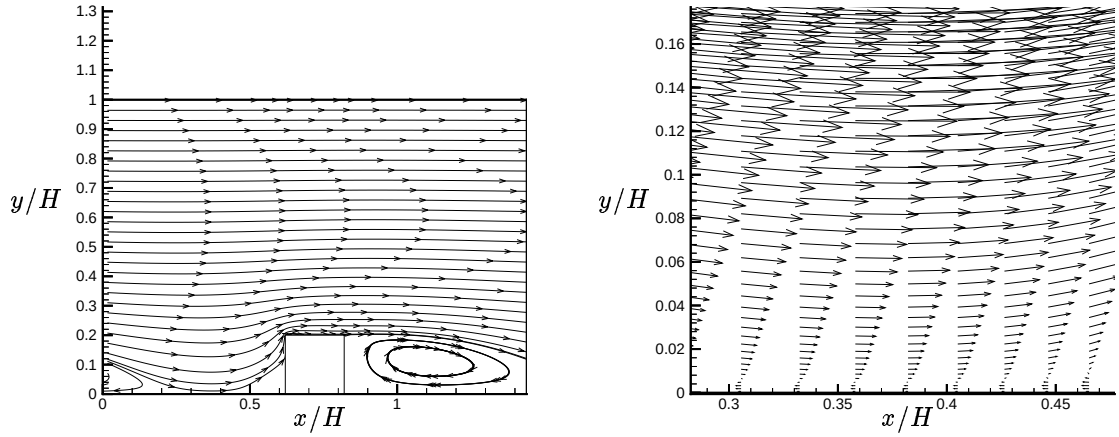

(a) Streamlines

(b) Detail of inter-rib region

Figure 10.18: Flowfield, Dean and Martin (D&M) 2D Ribbed Channel

The Drain and Martin experiments have very different geometric parameters, as compared to the above test case. The height-to-height ratio is $e/H = 0.2$, and the pitch-to-height ratio is $P/e = 7.2$. The ribs are thus much larger than in the above test cases – with a blockage effect of 20% – and hence the flowfield is changed as compared to those above. In addition to the rib being larger, the distance between the ribs is smaller, both conditions making it difficult for the flow to re-attach between the ribs. The flowfield for the $Re_D = 37\,600$ case, computed with the Peng *et al.* $k-\omega$ model, is displayed in Fig. 10.18, where a close-up around the expected re-attachment point is also included. The range of the abscissa in these figures originates from a scaling process where the channel height was fixed to 1 with a pitch of: $P/e \cdot e/H = 7.2 \cdot 0.2 = 1.44$. This ratio is later used as a positional indicator in Figs 10.19 and 10.20. In Fig. 10.18(a), it may seem that the re-attachment point is located around $x/H = 0.3$. However the enlargement of this area in Fig. 10.18(b) reveals that there is in fact no proper re-attachment point along the lower wall. Although only the flowfield from the Peng *et al.* $k-\omega$ model is displayed, none of the turbulence models used predict a re-attachment point located in the inter-rib region. According to the experiment, however, the the re-attachment length is $x/e = 4.32$, with x measured from the downstream upper corner of the rib. The velocity profiles at this specific point are displayed in Fig. 10.19(d).

Flowfield, $Re_D = 37\,200$: The quantities measured in this experiment were streamwise velocity, U, and the Reynolds stresses, $\overline{u'u'}$, $\overline{v'v'}$, $\overline{u'v'}$. Here, only the streamwise velocity together with the shear stress is displayed, since these are the most relevant parameters. Fig. 10.19 shows the normalized velocity profiles at selected points. The normalization is made with the bulk velocity. If the extracted points (x/H values, see Fig. 10.18 for the location of these points) are changed to values normalized with the rib height and x measured from the upper downstream corner of the rib, then the profiles are extracted at, Fig. 10.19(a), $x/H = 0.64 \rightarrow x/e = -0.9$, which is close to the upstream upper corner of the rib, where separation occurs, Fig. 10.19(b), $x/H = 0.72 \rightarrow x/e = -0.5$, which

is centered on the ribtop, Fig. 10.19(c), $x/H = 0.02 \rightarrow x/e = 3.18$, somewhere in the re-circulation bubble behind the rib, and Fig. 10.19(d), at $x/H = 0.24 \rightarrow x/e = 4.32$, which is the re-attachment point found in the experiment.

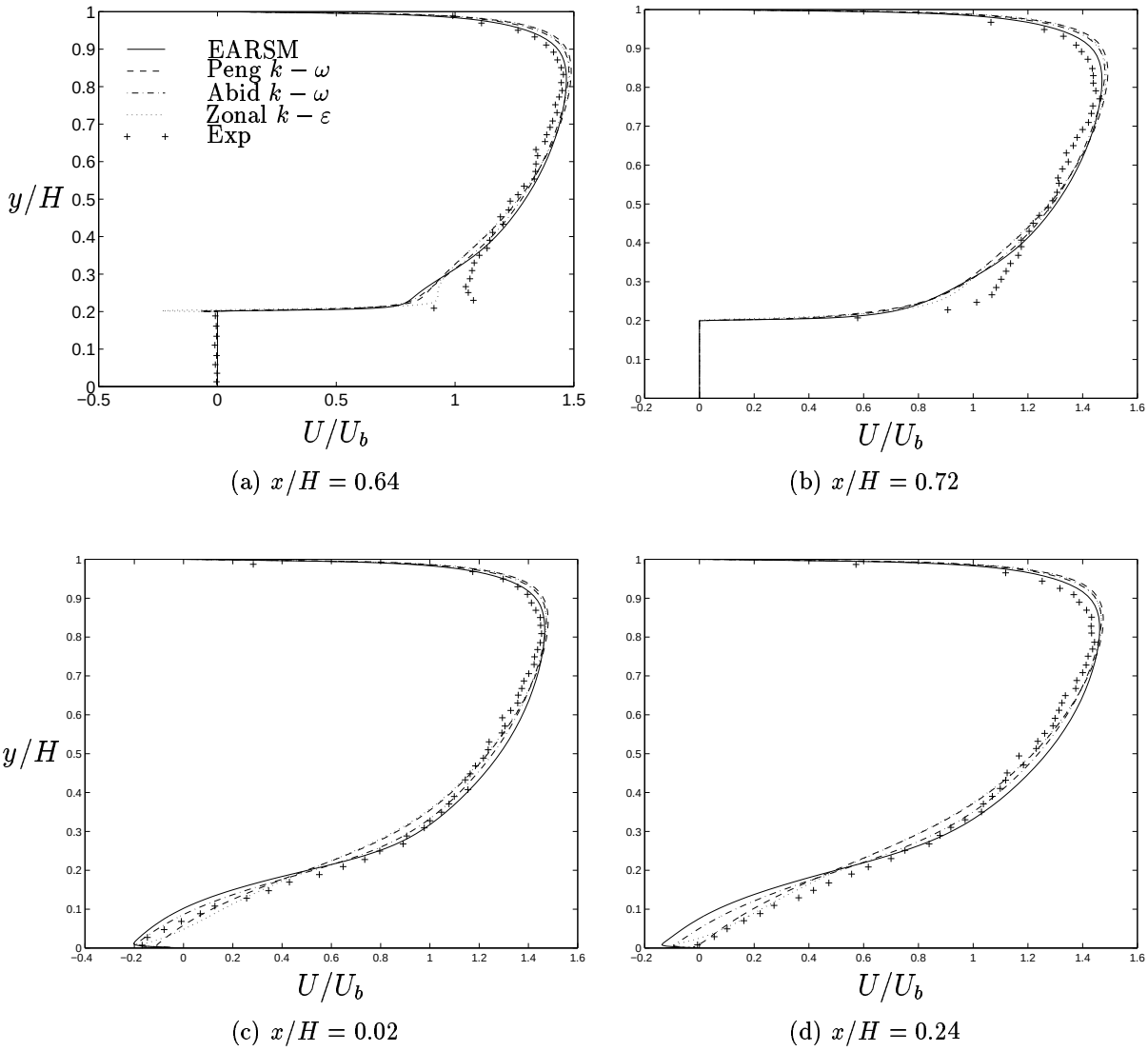

(a) $x/H = 0.64$ (b) $x/H = 0.72$

(c) $x/H = 0.02$ (d) $x/H = 0.24$

Figure 10.19: Velocity Profiles, D&M 2D Ribbed Channel

Overall, the different turbulence models predict the same velocity profiles and rather close to those measured. This is also in agreement with the previous statement that the flowfield from any model can be used.

Focusing on the rib top, Figs. 10.19(a) and 10.19(b), it can be seen that all models under-predict the near-wall velocity, out to $y/H = 0.4$. Close to the upstream corner of the rib, Fig. 10.19(a), the zonal model differs from the other models, with a higher near-wall velocity – in better agreement with the experimental data. Otherwise, the models behave equally. There is a small question regarding the measured data however, since the velocity profile around the upstream corner of the rib, see Fig. 10.19(a), is rather strange. The increase in the measured near-wall velocity – at $y/H = 0.25$ – is quite difficult to comprehend, and the only reasonable explanation is an error in the measured data. Note also that there is a slight over-estimation of the velocities on the opposite wall, which is

less obvious for the EARSM.

In the re-circulation region, Fig. 10.19(c) the EARSM and Abid *et al.* models predict too large a back flow, the largest being for the EARSM. Both the zonal and the Peng *et al.* are in closer agreement with the measurements, although the deviations are generally rather small.

At the re-attachment point, Fig. 10.19(d), the EARSM still predicts a rather large back flow, indicating too large a predicted re-circulation bubble. The zonal model gives the closest agreement with the experiment, whereas the two $k-\omega$ models return velocity profiles between those of the EARSM and the zonal. Note however that none of the models capture the re-attachment point correctly, all predicting back flow along the wall. This is probably because this rib configuration is on the limit of yielding a re-attachment point at all. The lack of any re-attachment point in the prediction would then simply be a result of the behavior of the models.

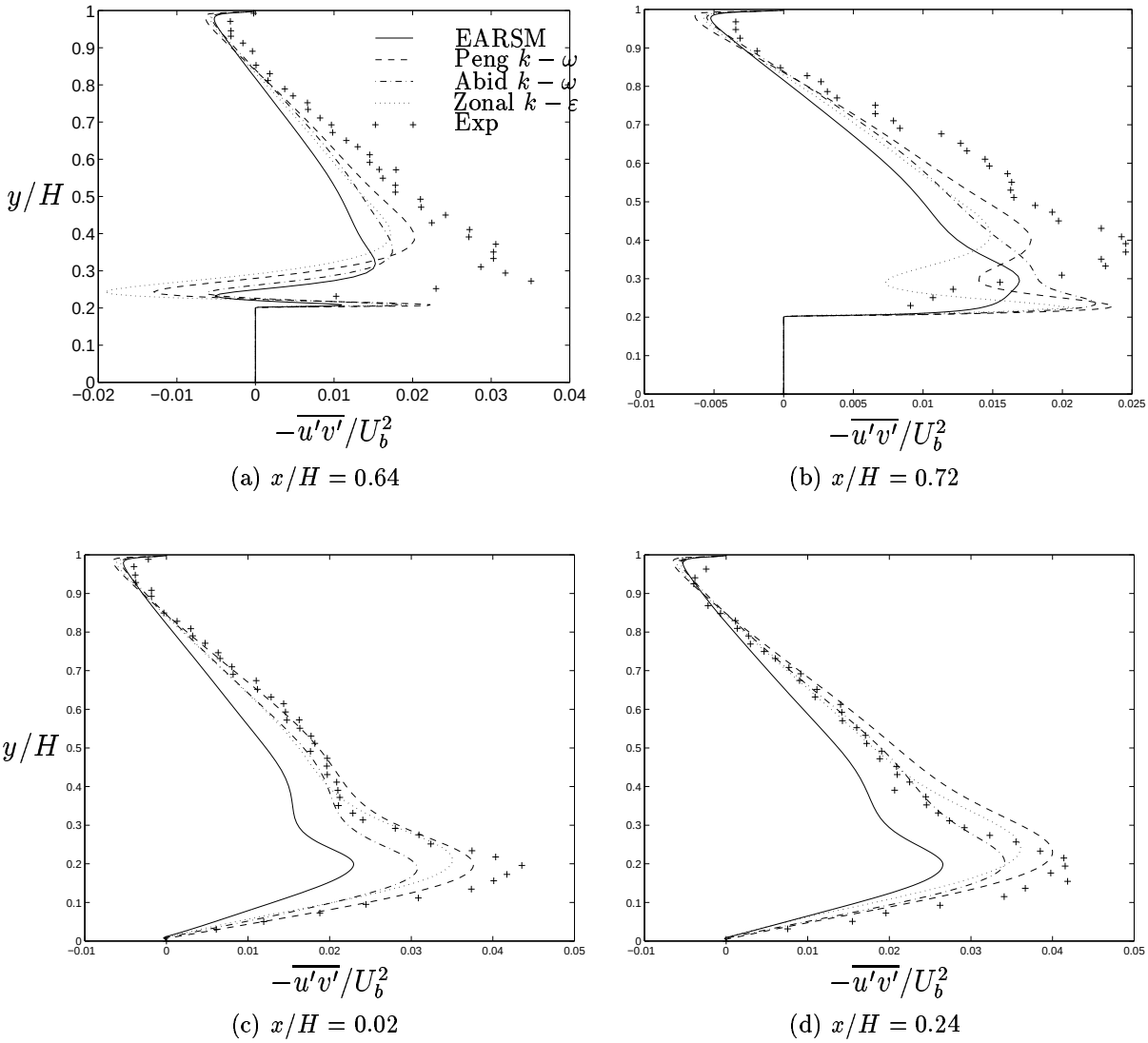

Figure 10.20: Shear Stress Profiles, D&M 2D Ribbed Channel

In Fig. 10.20, the shear stresses $\overline{u'v'}$ are plotted at the same selected points. The shear stresses are normalized with the square of the bulk velocity.

The turbulence models have most difficulties atop the rib, especially at the upstream corner, see Fig. 20(a). None of the models predict the near-wall shear stress to be as large as is given by the measurements but, close to the rib top, instead predict large shear stresses of the opposite sign. The models are based on the Boussinesq hypothesis (the EARSM is essentially an extended EVM) and would yield large negative shear stress where there are large positive velocity gradients. The shear stresses are modeled, according to Boussinesq, see Eq. 6.1, as:

$$\overline{u'v'} = -\nu_t \left(\frac{\partial U}{\partial y} + \frac{\partial V}{\partial x} \right) \tag{10.2}$$

The positive gradient of the velocity profiles on the rib top, see Fig. 19(a) would give a large negative shear stress. The results found in the predictions are however the opposite, close to the wall! The reason for this is the second term in the Boussinesq expression, $\partial V/\partial x$, which is usually neglected with a good approximation in boundary layer flows. In separated flows, as found around the rib, this can not be done.

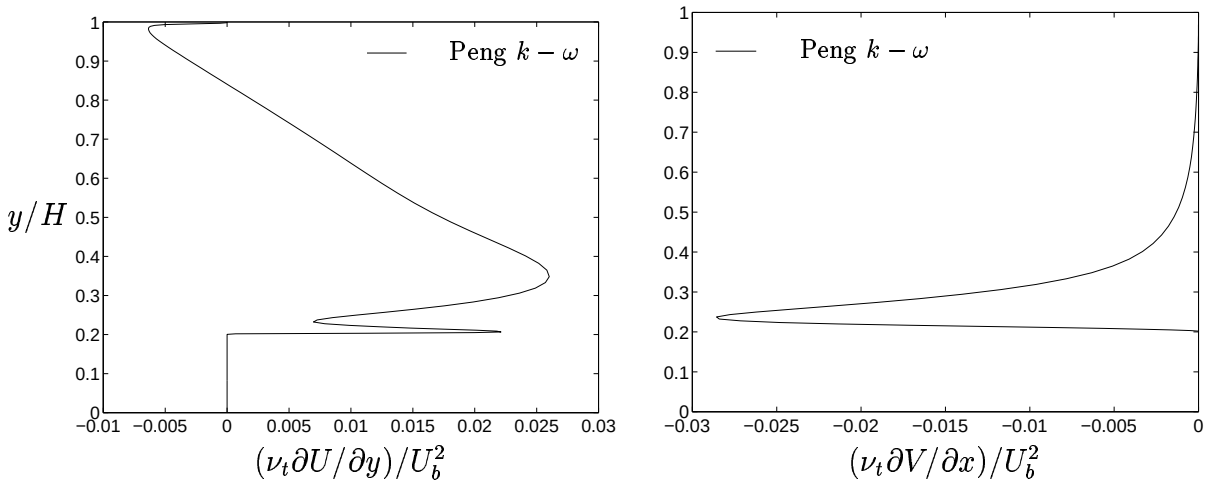

(a) Streamwise (b) Cross-stream

Figure 10.21: Velocity Gradients at $x/H = 0.64$, D&M 2D Ribbed Channel

In Fig. 10.21, the two parts of the shear stresses are shown individually for the Peng *et al.* $k-\omega$ model. As can be seen in this figure, there is a very strong $\partial V/\partial x$ close to the rib top, which is greater than the positive streamwise velocity gradient. The dip at $y/H = 0.25$ in Fig. 10.21(a) is the result of the re-circulation bubble. Owing to the circulating velocity field of the vortex, the streamwise velocity gradient is smallest for wall coordinates equal to the location of its center, which thus in this case is found at roughly $y/H = 0.25$.

Returning to Fig. 10.20, the model that behaves most closely to the measurements is not surprisingly the EARSM, which adds some anisotropy description to the shear stress predictions. Equally reasonable is that the zonal model gives the worst results, since that model includes only a length scale correction in the near-wall region.

Further downstream on the rib top the predictions improve, and especially the EARSM and the Abid *et al.* $k-\omega$ model yield a similar profile as the measurement data. The zonal model once more predicts a rather large deviation in the shear stress.

In the re-circulation region, see Fig. 10.20(c), the Peng *et al.* $k-\omega$ model achieves rather close agreement with the experiment and the EARSM deviates more. This latter is most likely a subsequent effect of the larger re-circulation bubble predicted by the EARSM.

At the re-attachment point, Fig. 10.20(d), the same results can be observed. It is interesting to compare the similarity in agreement between the prediction of a certain model and the experiment with respect to the velocity profiles and the shear stress. The Peng *et al.* model yields the closest velocity profile for the velocity profile and, as can be seen in Fig. 10.20(d), for the shear stress also. In the case of the EARSM, the reverse is true; it deviates most of the models for both the velocity profiles and the shear stress. This finding is a direct consequence of the strong coupling between the velocity profile/gradients and the shear stress, as indicated through the Boussinesq equation.

Heat Transfer, $Re_D = 12\,600$: The heat transfer measurements were made at a different Reynolds number than were the flowfield measurements. Although there is a ratio of almost three between the two Reynolds numbers, the two flowfields have the same characteristics, and hence there is no need of any additional streamline plot. The heat was introduced through a heater along the lower wall. The rib was made of highly conductive material, thus transmitting the heat-flux to the flow without any resistance. The predictions were made with the same turbulence models as for the flowfield and with the same mesh. The measured and predicted Nusselt number is plotted in Fig. 10.22. The Nusselt number measurements were made on all sides of the rib, including the east and west side. This makes the plotting axis slightly different than in the other cases. Since all three faces were included, the proper parameter would be the surface parameter, s, which includes all wetted areas. The abscissa in this case is thus the pitch length, P, plus two rib heights, e. The pitch-to-height ratio was $P/e = 7.2$, and adding two rib heights yields a total length of $P/e = 9.2$. The abscissa in Fig. 10.22 is however normalized with the height-to-height ratio, $e/H = 0.2$, giving a normalized surface coordinate ranging from 0 to $P/H = 1.84$, where the rib top is located from $P/H = 0.82$ to $P/H = 1.02$. The vertical broken lines are where the rib top corners are located, i.e. at $P/H = 0.82$ and $P/H = 1.02$.

The Nusselt number profiles for the models are reasonable accurate, apart from the zonal model. The levels are generally under-predicted, especially at the rib top and the east side (downstream side). The Peng *et al.* $k-\omega$ model yields the largest values, while the zonal model the lowest – much as has been previously observed. The bump in front of the rib, which has been seen before, has almost disappeared, apart from the predictions by the zonal model. Since the Nusselt number is an indicator of the turbulent viscosity – through the heat transfer model applied in this thesis – it can be concluded that there is either less turbulent production or larger destruction in this region compared to earlier test cases. As there is no reason to believe that there is a higher value of ω or ε, there must be less k in this area. The production of k originates from velocity gradients through the Boussinesq hypothesis, and large velocity gradients are found in strong vortices. Hence the smaller predicted Nusselt number for this case is a result of a weaker vortex formed in front of the rib. One interesting new aspect in this test case is how well (or poorly) the models predict the west and east side of the rib. On the west side (upstream of the rib), all models behave equally well, or poorly – with the, Nusselt number under-predicted by as much as 50% close to the upper corner. The models differ on the east side, although all of them under-predict the Nusselt number.

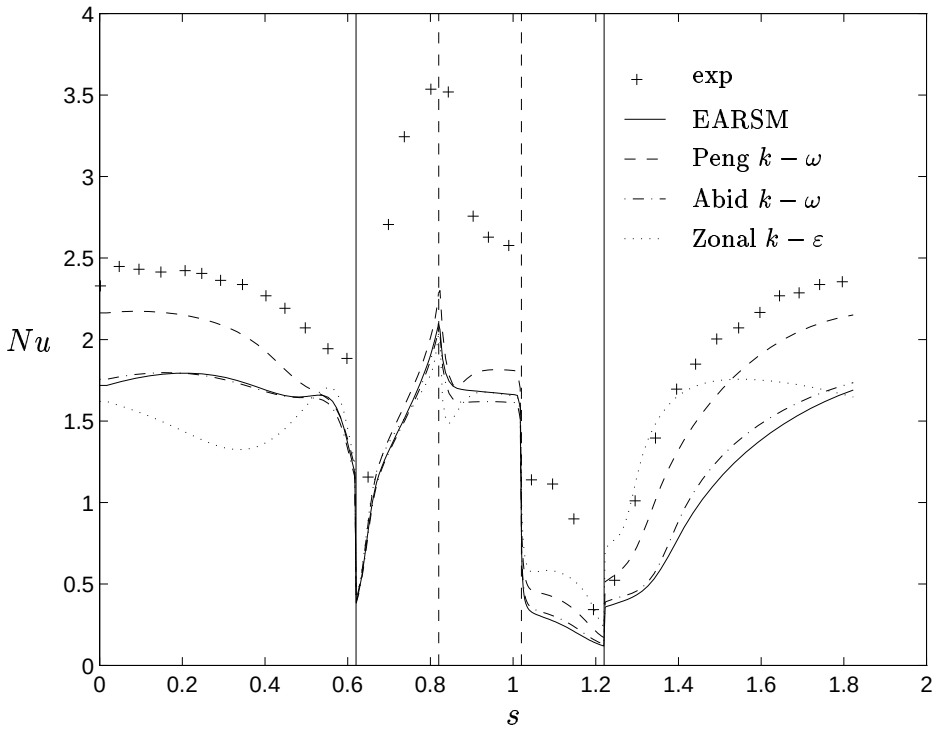

Figure 10.22: Nusselt Number, D&M 2D Ribbed Channel

10.4 3D Rotating Channel

The results of the computations of a smooth 3D rotating channel were used mainly to compare the performance of different turbulence models with each other and a Large-Eddy-Simulation (LES). It is very valuable to compare the results with the basis of vorticity. However, before using the vorticity equation, 5.74, it may be reduced to simplify an understanding. The streamwise vorticity can be found from either taking the x-component of the Reynolds average vorticity equation, Eq. 5.74, or, more simply, making an operation on the the Reynolds average momentum equation, Eq. 5.7. If the latter approach is used, then the Reynolds average momentum equation is derivatived with respect to $\partial/\partial x_q$ and multiplied by the Levi-Cevita tensor, ϵ_{1qi}, to yield:

$$\epsilon_{123}\frac{\partial}{\partial x_2}\overline{\mathcal{N}(u_3)} + \epsilon_{132}\frac{\partial}{\partial x_3}\overline{\mathcal{N}(u_2)} \tag{10.3}$$

where the first index ($1 = x$) of the Levi-Cevita tensor gives the streamwise component. The same operations were made with the rotational vorticity, equation Eq. 4.41, starting from the rotational momentum, equation Eq. 4.24. Below the streamwise component of Eq. 4.41 is written:

$$\rho\frac{\partial \omega_1}{\partial t} + \rho u_j\frac{\partial \omega_1}{\partial x_j} + 2\rho u_j\frac{\partial \Omega_1}{\partial x_j} = \rho\omega_j\frac{\partial u_1}{\partial x_j} + 2\rho\Omega_j\frac{\partial u_1}{\partial x_j} + \mu\frac{\partial^2\omega_1}{\partial x_j^2} \tag{10.4}$$

This is identical to the mean part of the Reynolds averaged vorticity equation, without any terms owing to the fluctuating part of velocities – i.e. the Reynolds stresses in the Reynolds averaged Navier-Stokes equation. In the case of constant angular velocity around the z-axis, $\Omega_i = (0, 0, \Omega_3)$, and when only stationary flowfield ($\partial/\partial t = 0$) is considered,

this is reduced to:

$$\rho u_j \frac{\partial \omega_1}{\partial x_j} = \rho \omega_j \frac{\partial u_1}{\partial x_j} + 2\rho\Omega_3 \frac{\partial u_1}{\partial x_3} + \mu \frac{\partial^2 \omega_1}{\partial x_j^2} \tag{10.5}$$

The difference between the momentum equation and the Reynolds average equation is the term including the Reynolds stresses, $\overline{u_i' u_j'}$. Taking the above equation as the foundation and adding the result of the Reynolds stresses would yield the time-averaged streamwise vorticity equation. Eq. 10.3, applied to the Reynolds stress term gives:

$$\epsilon_{123} \frac{\partial}{\partial x_2} \left[\frac{\partial}{\partial x_j} \left(\overline{u_3' u_j'} \right) \right] + \epsilon_{132} \frac{\partial}{\partial x_3} \left[\frac{\partial}{\partial x_j} \left(\overline{u_2' u_j'} \right) \right] \tag{10.6}$$

expanding the j-index yields:

$$\frac{\partial}{\partial x_2} \left[\frac{\partial}{\partial x_1} \left(\overline{u_3' u_1'} \right) + \frac{\partial}{\partial x_2} \left(\overline{u_3' u_2'} \right) + \frac{\partial}{\partial x_3} \left(\overline{u_3'^2} \right) \right] - \frac{\partial}{\partial x_3} \left[\frac{\partial}{\partial x_1} \left(\overline{u_2' u_1'} \right) + \frac{\partial}{\partial x_2} \left(\overline{u_2'^2} \right) + \frac{\partial}{\partial x_3} \left(\overline{u_2' u_3'} \right) \right] \tag{10.7}$$

Adding together the mean part, Eq. 10.5, and the Reynolds stress part, Eq. 10.7[31], and dropping the streamwise derivation components[32] thus yields:

$$\rho u_j \frac{\partial \omega_1}{\partial x_j} = \rho \omega_j \frac{\partial u_1}{\partial x_j} + 2\rho\Omega_3 \frac{\partial u_1}{\partial x_3} + \frac{\partial^2}{\partial x_2 x_3} \left(\overline{u_2'^2} - \overline{u_3'^2} \right) + \left(\frac{\partial^2}{\partial x_3^2} - \frac{\partial^2}{\partial x_2^2} \right) \overline{u_2' u_3'} + \mu \frac{\partial^2 \omega_1}{\partial x_j^2} \tag{10.8}$$

This equation forms the basis for later discussions, especially the impact of the Coriolis force on the streamwise vorticity. In the case of a non-rotating duct, the Coriolis force production of the above equation is of course dropped, and thus only Reynolds stress interactions can produce any streamwise vorticity. For a square duct, these interactions produce, in a rather complex way, eight corner vortices [21], two in each corner of the duct. These eight vortices are fully symmetric, with symmetry lines along the diagonals and the centerlines, making a total of eight identical vortices, although with alternating signs. Fig. 10.23 shows the secondary flows in the cross-section. This result is taken from a LES (Large-Eddy-Simulation) computation [40] and is depicted for the lower left hand corner. Note however that the computation was made on a whole duct and – purely for clarity – only one of the corners is shown.

As can be seen in Fig. 10.23, the two vortices are symmetrical along the diagonal. A positive vortex is created on the LHS of the diagonal with inflow towards the corner along the diagonal symmetry and outflow along the left sidewall. This vortex has its counterpart on the other side of the diagonal with inflow along the diagonal and outflow along the lower sidewall.

In the case of rotation, the Coriolis force adds a production term in the streamwise vorticity equation, $2\rho\Omega_z \partial u/\partial z$, see Eq. 10.8. This term will increase the vorticity wherever the cross-stream gradient of the streamwise velocity gradient is positive and likewise decrease where it is negative. For a rotation around the z-axis, it is thus the z-wall normal which is important. Hence, along the walls at $z/H = 0$ and $z/H = 1$, an increase or decrease of vorticity will occur.

[31] Changing signs since the Reynolds stresses are moved from the LHS to the RHS of the equation.

[32] This can be done, since the flow is fully developed, and any streamwise derivate is negligible, see Perkins, [44]

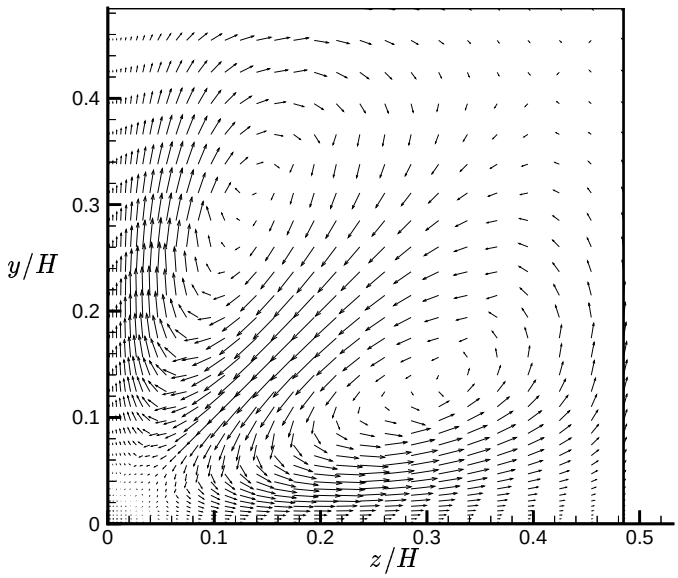

Figure 10.23: Corner Vortices in a Square Duct, [40]

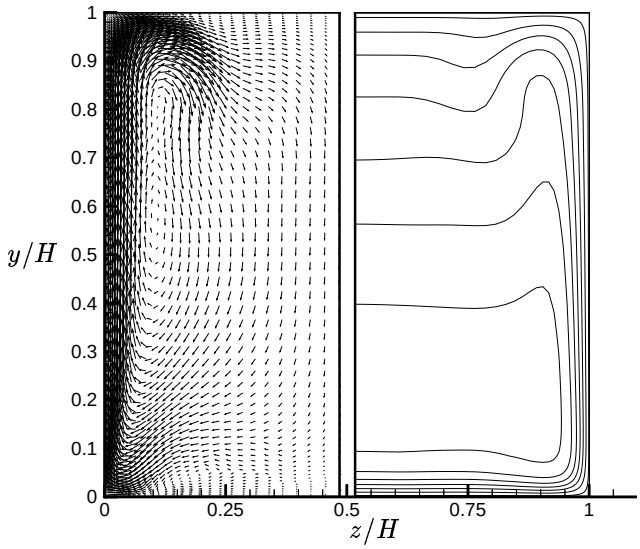

Figure 10.24: Cross-stream Velocity Vectors, and Streamwise Contours, $Ro_H = 0.1$, [40]

Fig. 10.24 is taken from the LES by Pallares and Davidson [40], with a positive rotation around the z-axis. The rotational number was set to: $Ro_H = \Omega H/U_m = 0.1$. The LHS of the figure shows the cross-stream velocity, and the streamwise velocity contours are shown on the RHS. Due to the non-slip condition at the walls, the streamwise velocity is zero at $z/H = 0$ and $z/H = 1$ and increases toward the center. The gradient is thus positive on the LHS and negative on the RHS of the duct, producing a strong positive vortex on the LHS and an equally strong negative vortex on the RHS, as is clearly indicated on the LHS of Fig. 10.24. Depending on the rotational number, these larger rotationally

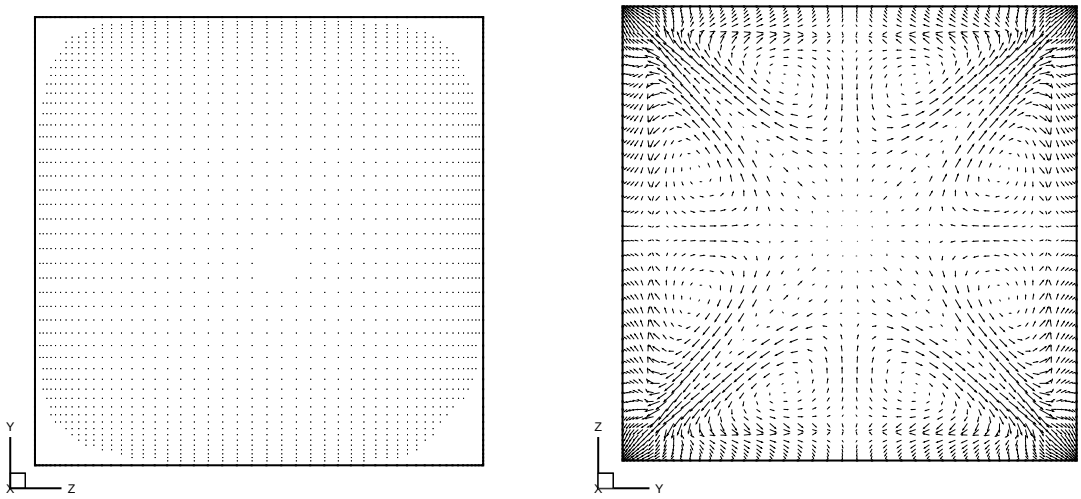

(a) $k-\omega$ (b) EARSM

Figure 10.25: Cross-stream Velocities, Stationary 3D duct

induced vortices will swallow the smaller Reynolds stress induced vortices. In the case of this rather high rotational number, only one additional small counter-rotating negative vortex can be seen close to the lower wall, as seen on the LHS of Fig. 10.24.

Comparing this with the stationary case, a number of symmetry lines are destroyed and in fact the only remaining one is the vertical symmetry line in the mid-plane. On the RHS of the figure where the contour values of the streamwise velocity are shown, the asymmetric velocity profile is clearly visible.

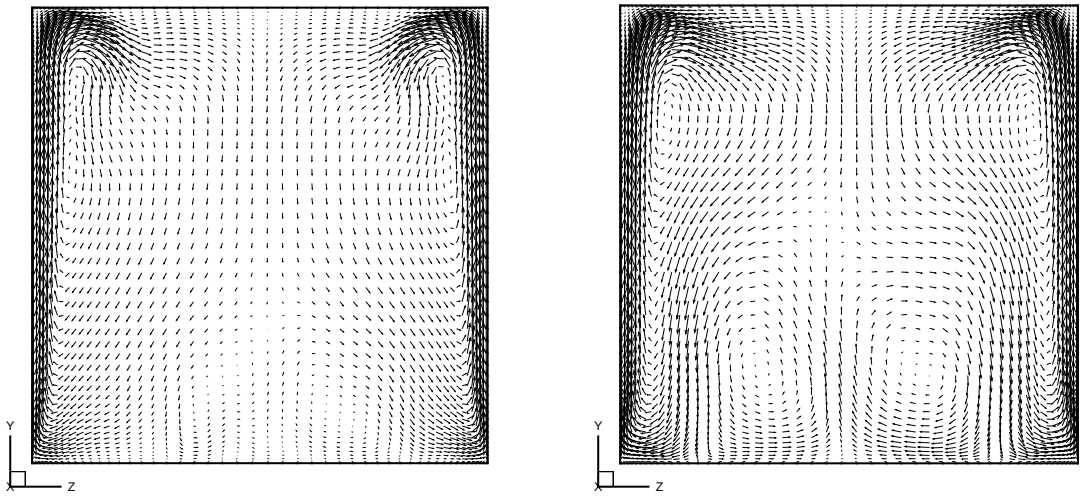

(a) $k-\omega$ (b) EARSM

Figure 10.26: Cross-stream Velocities, Rotating 3D-duct, $Ro_H = 0.1$

Taking the LES computation as a comparison several computational runs were made with different turbulence models. The main reason was to compare the effects of the

Coriolis forces and the Reynolds stresses. In order to do that, the Abid *et al.* $k-\omega$ [2] model is compared with the Gatski and Speziale EARSM [13] with the non-linear Speziale-Sarkar-Gatski (SSG) pressure-strain model [51]. It should be stressed that the EARSM is based on the same $k-\omega$ model, and thus the differences that are shown are purely a Reynolds stresses effect. The computational data were a mesh with $5 \times 50 \times 50$ nodes and a Reynolds number based on channel height $Re_H \approx 4000$ approximately equal to a Reynolds number based on the friction velocity, $Re_\tau = 300$. These values are close to those used for the large eddy simulations of above. Two sets of computations were made, one stationary and one with a rotational speed of $Ro_H = 0.1$. It was found that, using the EARSMs, the secondary flows in the cross-stream plane were in fact unstable, and the only reasonable way to achieve a trustworthy result was to make a transient calculation and time-average the results.

Fig. 10.25 shows the cross-stream velocity field for the two turbulence models, on the LHS the $k-\omega$ and on the RHS the EARSM. Fig. 10.25(a) is a rather dull picture, although it is included to clarify that the EVMs are useless in computing the secondary flows in a 3D duct of a square cross-section. For the EARSM computation, the Reynolds stress induced secondary flow can clearly be seen, and it is interesting to observe the similarities with the LES above, see Fig. 10.23.

Fig. 10.26 shows the cross-stream velocities for the rotating case. For the $k-\omega$, the results have improved very much, which may be explained by the Coriolis induced term in the vorticity equation, Eq. 10.8, $2\rho\Omega_z \partial u/\partial z$. This term, which is the dominating vorticity producing term, is not a part of the turbulence model. Hence, even with a laminar case, these two large vortices will appear in a rotating duct. In Fig. 10.26, the small contributions of the Reynolds stresses are difficult to see in this higher rotational number case. It is thus not surprising that both the $k-\omega$ and the EARSM yield reasonable results compared to the large eddy simulations [40], see Fig. 10.24.

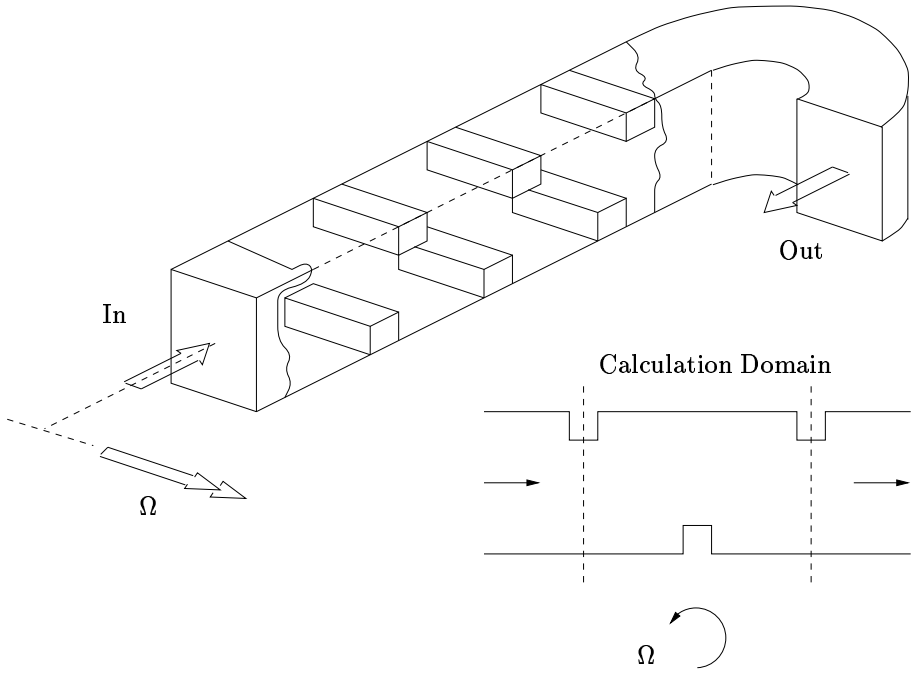

Figure 10.27: Geometry of the UMIST 3D Ribbed Channel Test Case

10.5 3D Ribbed Channel

The first of the three test cases in this section was also predicted in the 2D ribbed channel test case, where the flow was assumed to be two-dimensional. The experiments are all obviously done in 3D, although in certain cases it can be assumed that there exist good approximate 2D measurement points in the channel. For example, in a channel with a large aspect width-to-height aspect ratio it can be assumed that there is approximately a 2D flow on the centerline. In such cases, it is indeed a great benefit to make a 2D computation instead of a 3D one. The major difference between the predicted 2D and the 3D ribbed channel cases is the large increase in computer resources, which necessitates the 3D meshes to be much coarser than for a 2D calculation, which will thus result in less accurate predictions. Even though there is a suitable channel configuration which could be simplified to a 2D predictions, there exists other reasons for performing a 3D computation. In the case that the channel is rotating around one of its axes, the rotational forces induce secondary flows which affect the flowfield to such that it loses its 2D characteristics, making a 3D computation the only possible solution.

The geometric configuration of the Baughn and Yan [3] test case can even for the 3D computation below be represented by the figure in the 2D ribbed channel section, Fig. 10.5, although the extent in the z-direction is not included. However, the two UMIST [22] cases (stationary and rotating), which are – note – not the same experiment as the 2D case, are less well represented by the same picture. Instead the geometry of the UMIST experiments is depicted in Fig. 10.27, with the appropriate calculation domain shown as well.

10.5.1 Baughn and Yan, $Re_H = 50\,000$, $Ro_H = 0$

This test case is a repeat of the Baughn and Yan 2D ribbed channel. But with the calculation extended into the third, z-dimension. The geometry condition for this case is a pitch-to-height ratio of $P/e = 10$ and a height-to-height ratio of $e/H = 0.0625$, with a Reynolds number based on the channel height of $Re_H = 50\,000$.

As previously stated, this case has ribs on both sides, opposite to each other, making possible a calculation on only half the channel, see section of Baughn and Yan in 2D ribbed channel. The top wall in Fig. 10.5 is thus a symmetry wall in this test case. Furthermore, for the 3D computation, the channel is symmetric in the z-direction as well, and hence the computation need only be extended to half the width of the channel. In total, it is necessary to compute only one-fourth of the channel, using a symmetry condition on the other sides. The mesh used in this prediction measures: $66 \times 50 \times 20$ which, due to the symmetry conditions, is a relative fine mesh, and hence reasonable results are expected.

The turbulence models used for this case are the Abid *et al.* $k - \omega$ model [2], the Gatski and Speziale [13] EARSM based on the Abid *et al.* $k - \omega$ model with the LRR pressure-strain model, and the Chen and Patel zonal $k - \varepsilon$ [7].

The flowfield for this test case is well represented by the 2D case, see Fig. 10.16.

The data measured in the experiment is the Nusselt number on the centerline, which is depicted in Fig. 10.28 along with the predictions of the three turbulence models. The predicted Nusselt number has essentially the same characteristics as for the 2D case, with the zonal model severely under-predict along the whole channel, while the two $k - \omega$ based models are closer in agreement with the measured data. As for the 2D case, the models predict a bump upstream of the rib, which is larger in the case of the zonal model, and is not found in the measurements. Downstream of the rib, the zonal increases the

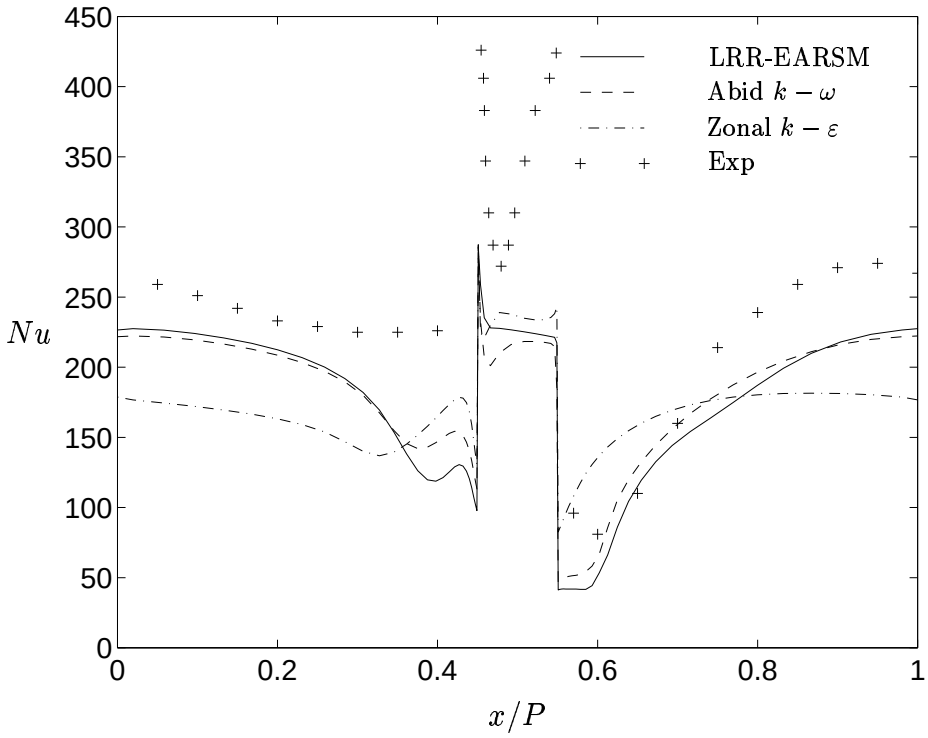

Figure 10.28: Nusselt Number, Baughn 3D Ribbed Channel

Nusselt number too quickly, while both the EARSM and the $k-\omega$ predict a similar slower increase, more as was found in the experiment. There are some small jerks in the Nusselt number profile for the EARSM, which is most likely a result of the not fully converged solution[33]. The inter-rib peak magnitude in Nusselt number is not captured by any of the models, although the $k-\omega$ based models yield the maximum Nusselt number at the correct location, which the zonal model misses quite dramatically at approximate one rib-height downstream the rib (excluding the bump in-front of the rib). The same discrepancy as for the 2D case is found on the rib top, and it is clear that a more refined mesh is necessary in this area to capture the large gradients found in the measurement.

Since this case was also computed in the asymptotic 2D case, a comparison between the two predictions can be fruitful. Fig. 10.29 shows the comparisons between the 2D calculations and the 3D calculation for the Abid *et al.* and EARSM models. There is only a minor difference in the predicted Nusselt number between the two cases for both the depicted turbulence models. There is a slight under prediction, of the 3D case as compared with the 2D case, which agrees with the previously seen phenomena in the $k-\omega$ based models, which predict a lower Nusselt number with a coarser mesh. On the rib top, the 3D computations return a higher Nusselt number than the 2D computations. The reason for this is not as obvious, although it is most certainly related to the rather coarse mesh in this area.

[33]This test case converged very slowly, especially for the EARSM predictions. The residuals for the EARSM predictions shown in the graphs, are not below 1% - which is otherwise the minimum demand in this report. In most cases the residuals were below 0.001.

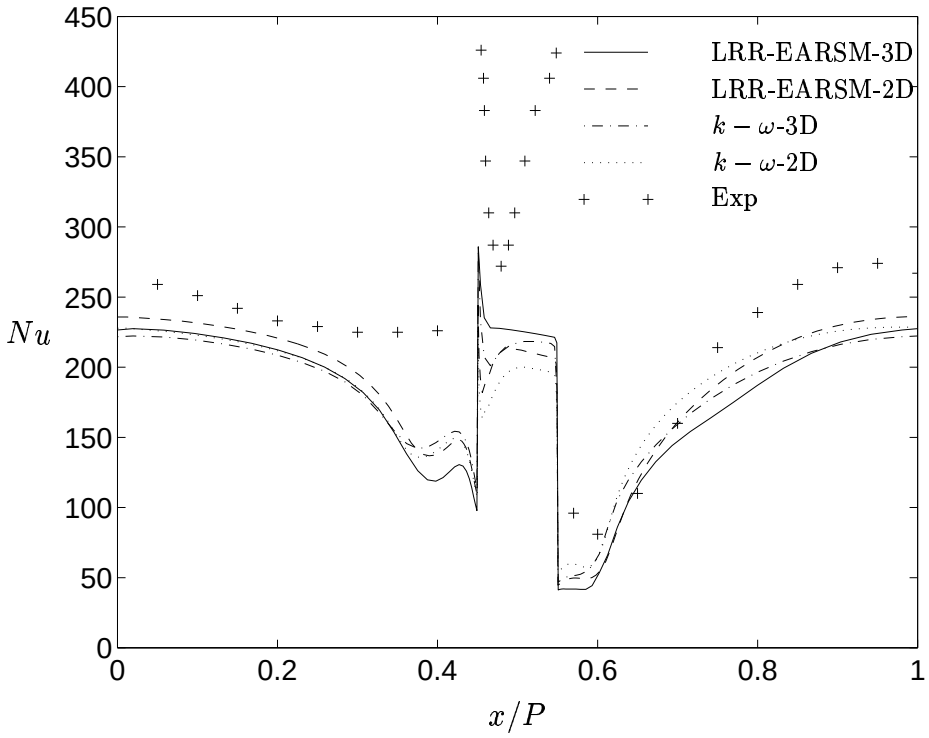

Figure 10.29: Nusselt Number, Baughn 3D/2D Ribbed Channel

10.5.2 UMIST, $Re_H = 100\,000$, $Ro_H = 0.2$ and $Ro_H = 0$

This and the following test case have exactly the same properties apart from that one is stationary and the other is rotating. For a general overview of the geometric conditions, Fig. 10.27 is of help. As indicated in that figure, these test cases have ribs on both walls, which however are staggered in relation to each other, opposed to what was the case for the Baughn and Yan, where the ribs were in line. For a staggered configuration, the calculation domain is increased because the symmetry condition on the centerline can not be applied and hence both the upper and lower wall with the ribs must be included in the computation. However there exists a symmetry line in the third z-direction, which thus enables the calculation domain to be reduced to half – even for the latter rotating case[34] – although it still represents a fairly large part of the duct and quite a large mesh is necessary. For these two cases, there were two different computation meshes, the medium mesh which measured $60 \times 60 \times 25$ and the fine mesh of $96 \times 96 \times 40$. For the stationary case, a grid-independence check is graphically shown for two of the turbulence models in Fig. 10.30.

The data are extracted at $x/P = 0$, which is at the inlet of the duct, and the profiles shown are for the streamwise velocity, U, the shear stress, $\overline{u'v'}$, and the two normal stresses, $\overline{u'u'}$ and $\overline{v'v'}$. The results are very encouraging, and it seems likely that the medium mesh is comfortingly fine and is thus used in the forthcoming presentation.

The measured data [22] – which are not the same as in the 2D UMIST ribbed channel test case – are: the streamwise velocity, U, the cross-stream velocity, V, the shear stress $\overline{u'v'}$, the normal stresses, $\overline{u'u'}$ and $\overline{v'v'}$, and the Nusselt number along the lower wall[35],

[34] Although there are rotating induced secondary flows in the rotating channel, they are symmetric through the centerline plane ($y-z$-plane), see also the schematic Fig. 2.2

[35] Not for the case of the rotating channel.

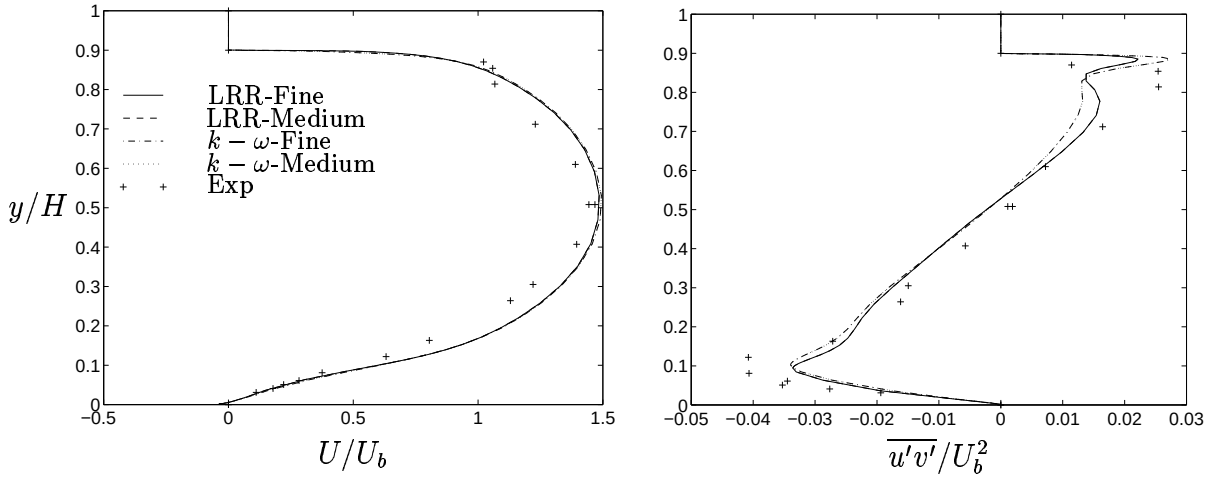

(a) U-Velocity

(b) $\overline{u'v'}$-Shear stress

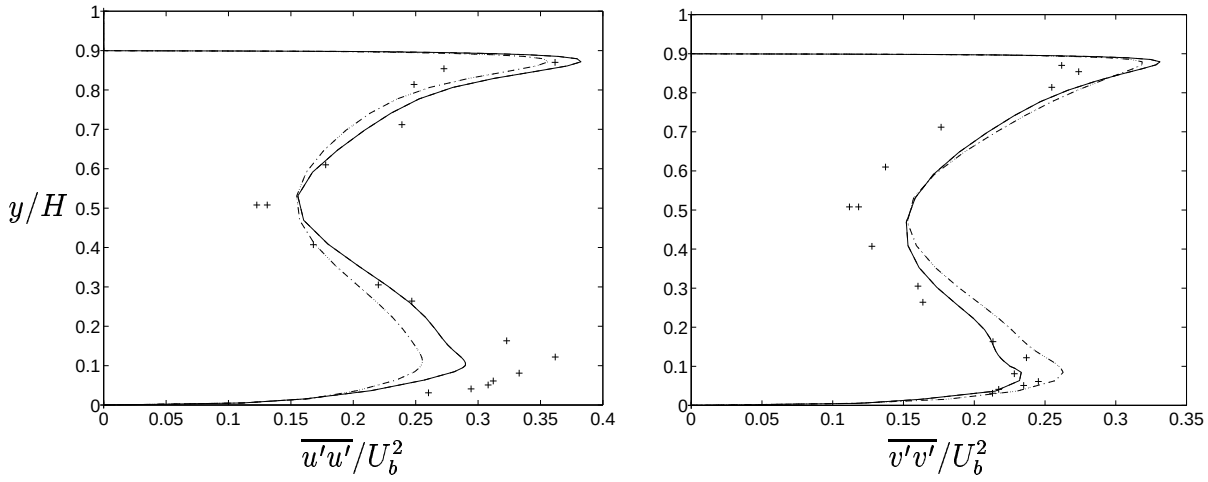

(c) $\overline{u'u'}$-Normal stress

(d) $\overline{v'v'}$-Normal stress

Figure 10.30: Medium-Fine Mesh Comparison at $x/P = 0$, UMIST 3D Ribbed Channel

in Fig. 10.27. The Reynolds number based on the channel height for both test cases is $Re_H = 100\,000$, and the rotating number also based on the channel height for the rotating case is $Ro_H = 0.2$. In the case of the velocity field the data are taken from four selected points, at the rib tops and in between the ribs. These four points are equivalent to x/P ratios of $x/P = 0$ (at the inlet, centered on the first rib on the upper wall), $x/P = 0.25$ (in the middle between the first upper rib and the lower rib), $x/P = 0.5$ (at the ribtop of the rib on the lower wall) and, finally, at $x/P = 0.75$ (in the middle between the rib on the lower wall and the second rib on the upper wall). The Nusselt number was measured along the lower wall excluding the rib. The heat-flux is transmitted through an electrical heater fixed at both the upper and lower walls. This enables a constant heat-flux at the walls to be achieved, which is also the boundary condition used in the computations.

The geometric condition for these test cases is the same as for the 2D UMIST case and the Rolls-Royce case. Thus there are a pitch-to-height ratio of $P/e = 10$ and a height-to-height ratio of $e/H = 0.1$. The blockage effect is a bit tricky to estimate, however, since these test cases have staggered ribs on the upper and lower walls. Taking the mid-rib

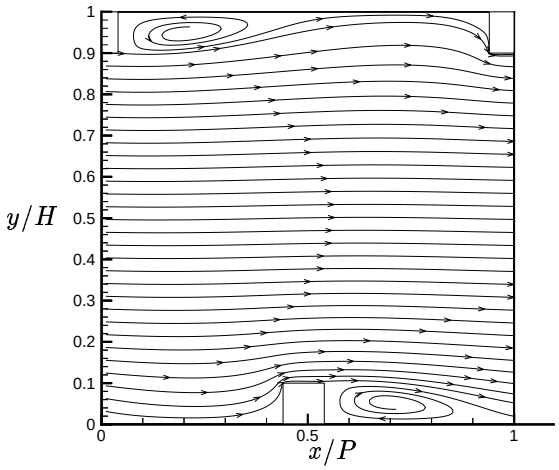

Figure 10.31: Streamlines, UMIST 3D Stationary Ribbed Channel

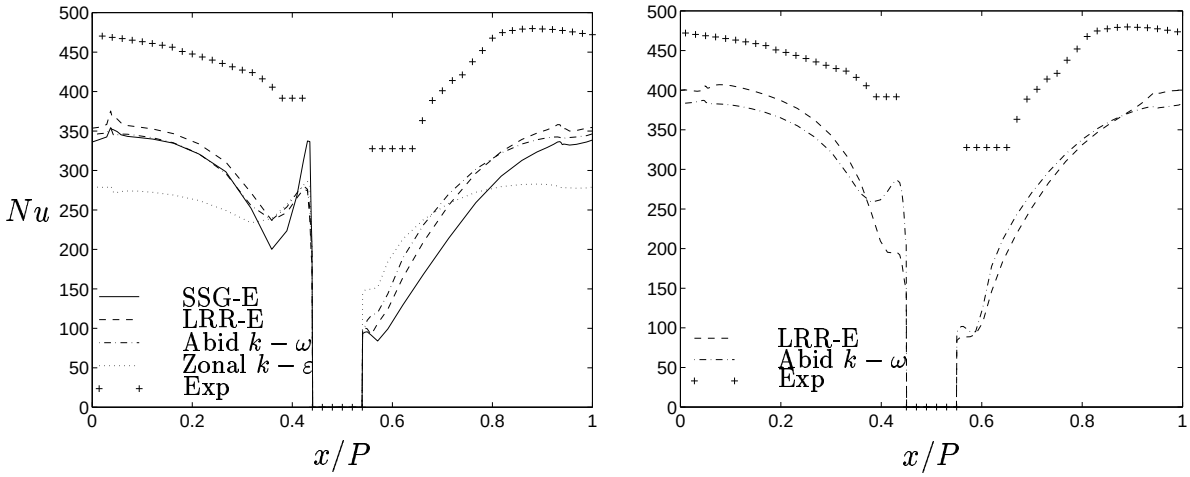

(a) Medium mesh

(b) Fine mesh

Figure 10.32: Nusselt Number, UMIST 3D Stationary Ribbed Channel

on the lower wall as the point of reference in the channel, the blockage would be 10%. However, due to the intervening upstream and downstream ribs at the opposite wall – the upper wall – the actually blockage effect is higher.

The turbulence models used are: the Abid *et al.* $k-\omega$ model, the Gatski and Speziale EARSM [13] based on the Abid *et al.* $k-\omega$ with either a SSG or a LRR pressure-strain model and, finally, the Chen and Patel zonal $k-\varepsilon$ model [7].

The stationary and rotating cases are presented separately below, starting with the stationary case.

Stationary: The experimental and predicted Nusselt numbers with the four turbulence models for the stationary case are depicted in Fig. 10.32. Fig. 10.32(a) shows the Nusselt number with the medium mesh, and Fig. 10.32(b) for the fine mesh. In the latter case, only the Abid *et al.* and the EARSM based on the LRR pressure-strain model

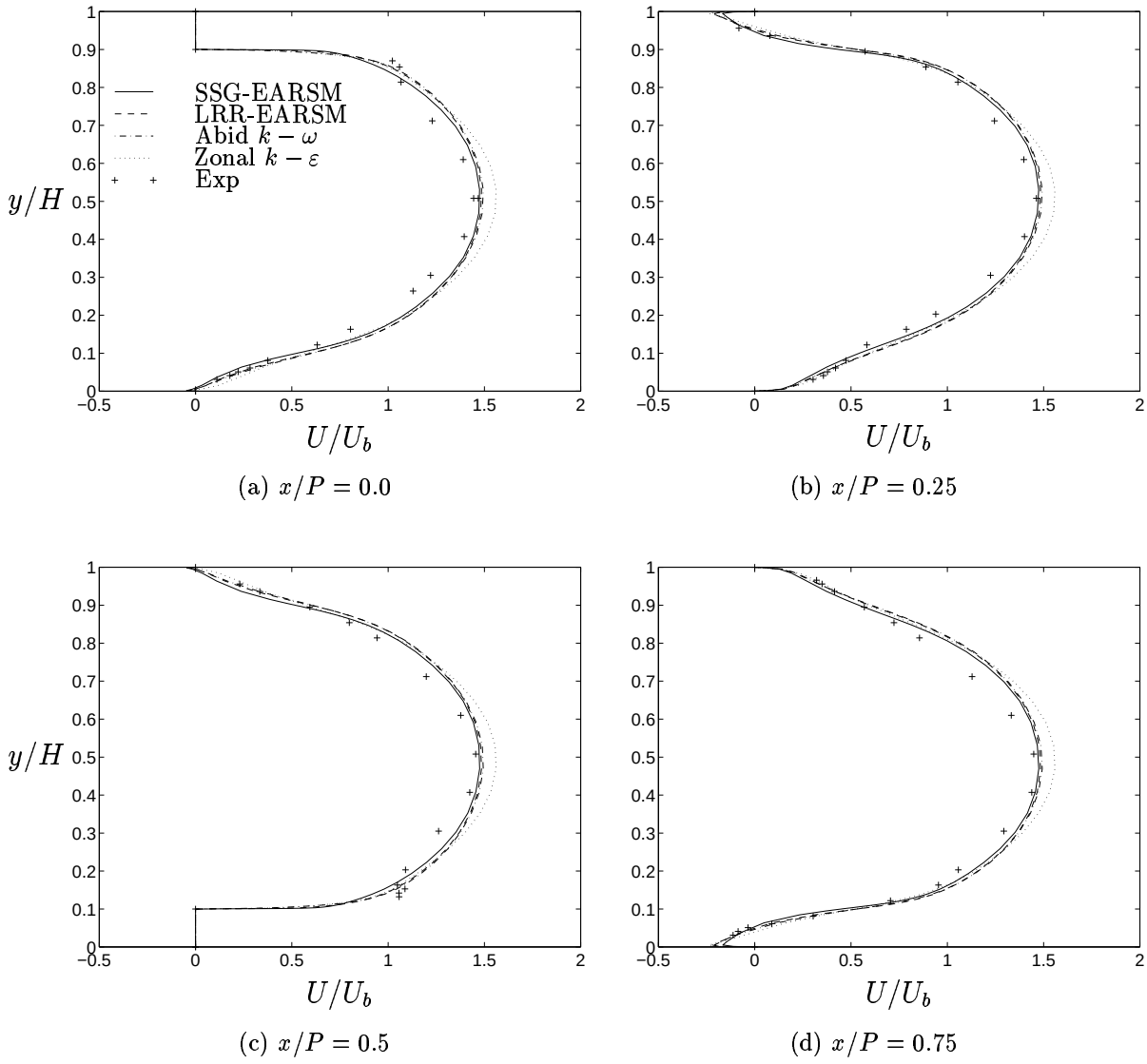

(a) $x/P = 0.0$ (b) $x/P = 0.25$

(c) $x/P = 0.5$ (d) $x/P = 0.75$

Figure 10.33: U-Velocity Profiles, UMIST 3D Stationary Ribbed Channel

are computed. Starting by comparing the returned Nusselt number for the medium and fine mesh, it can easily be seen that the medium mesh can not be considered mesh-independent. The conclusion drawn from the velocity field is thus not valid in the case of a heat transfer prediction, where a finer mesh is needed to resolve the important near-wall characteristics for heat transfer predictions. This was somewhat discomforting, especially considering an even finer mesh than the $96 \times 96 \times 40$. Using the fine grid, the computation time needed for each iteration was approximately one minute. The number of iterations needed for a converged solution, depended on the initial flowfield and turbulence model, and was close to 10 000, i.e. one week's computation for each model! Progressing to a finer grid would mean a month of computation – not an interesting perspective.

Despite this rather discouraging result, the first observation of the velocity field is still valid, and even though the levels for the Nusselt number prediction usually change with mesh refinement, the profiles are more or less similar. In this case, the Nusselt number increases by about 50 units from the medium to the fine mesh, and – although this is just speculation – the levels achieved with a even finer mesh would not change as much,

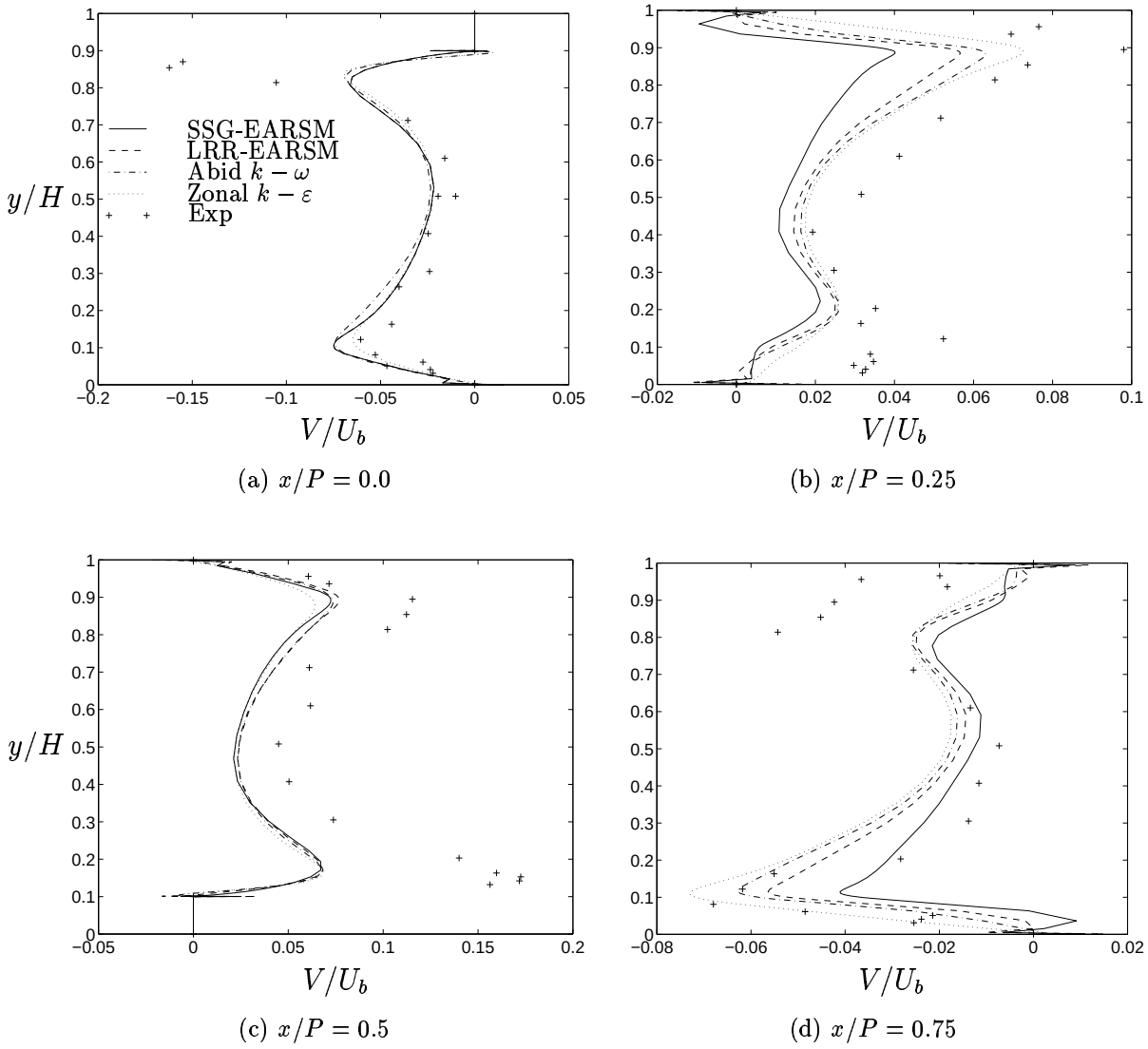

Figure 10.34: V-Velocity Profiles, UMIST 3D Stationary Ribbed Channel

although a slight increase might be expected, see also the grid independence check for the 2D ribbed channels, where a mesh of 110×120 was sufficient for the Rolls-Royce case[36]. Without making any conclusion regarding the predicted Nusselt number levels, the profiles are generally reasonable. The same conclusion as for the 2D ribbed channels could be drawn here, that the zonal model under-predicts more than the $k-\omega$ based models. The bump upstream the rib is still present, with the zonal model predicting a larger one. The three $k-\omega$ models return similar profiles from $x/P = 0$ to the rib, but deviate somewhat on the downstream side. The LRR-EARSM[37] and the Abid *et al.* $k-\omega$ predict much the same profiles, with the LRR-EARSM recovering the Nusselt number more slowly. Switching to the SSG-EARSM, the recovery is much slower than in the other two $k-\omega$ based models, in agreement with the measurements. The peak is predicted at the same point however, which is roughly in the middle between the ribs. However the increased performance on the downstream side of the rib of the SSG-EARSM

[36]Which is – agreeably – a slightly simpler test case even for an asymptotic 2D case.

[37]This is the EARSM used in most cases and for all 2D ribbed channels.

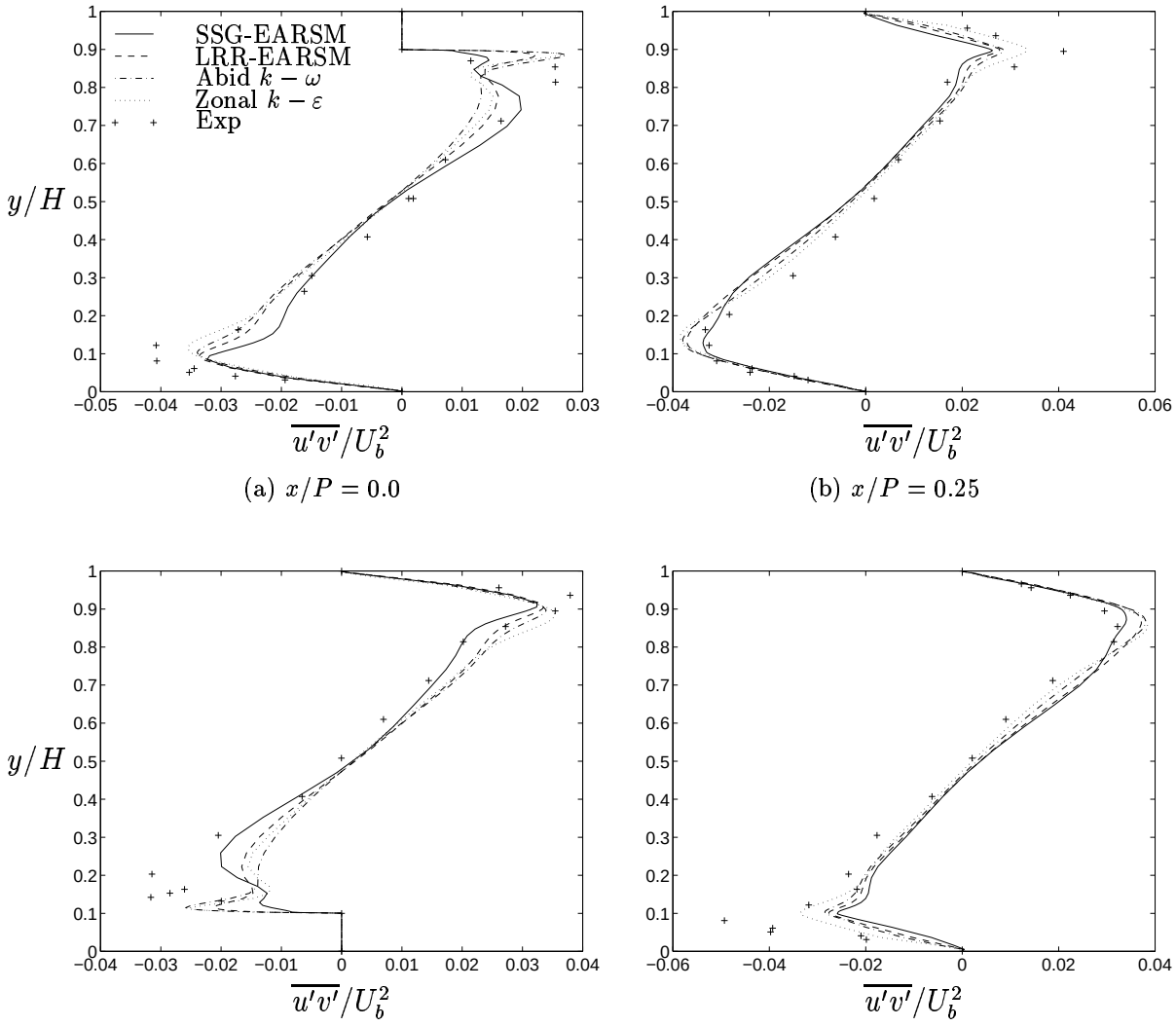

Figure 10.35: $\overline{u'v'}$-Shear Stress, UMIST 3D Stationary Ribbed Channel

is compensated by a rather large predicted bump in front of the rib. This is in fact even larger than the zonal model – and is a severe discrepancy as compared to the measured data. For the EARSM models, there are some distinct fluctuations around the mid-range interval between the ribs. These are most likely a result of the rather stretched mesh in this area and, in the case of the fine mesh, see Fig. 10.32(b), these fluctuations have decreased notably.

Moving on to the velocity field comparisons, there is great amount of data, that it is possible to point to only certain more interesting figures. There are in total 20 figures with five different velocity variables, at four different locations along the channel. For a general view of the velocity field in this test case, see the streamline plot in Fig. 10.31. The flow is characterized by a large re-circulation behind each rib, with a smaller bubble in front of each rib, much as in the case of the 2D ribbed channel. The streamwise velocity profiles normalized with the bulk velocity are plotted in Fig. 10.33, where the most notably difference among the models is the over-prediction of centerline velocity for the zonal model. Apart from that, all models achieve similar velocity profiles as the

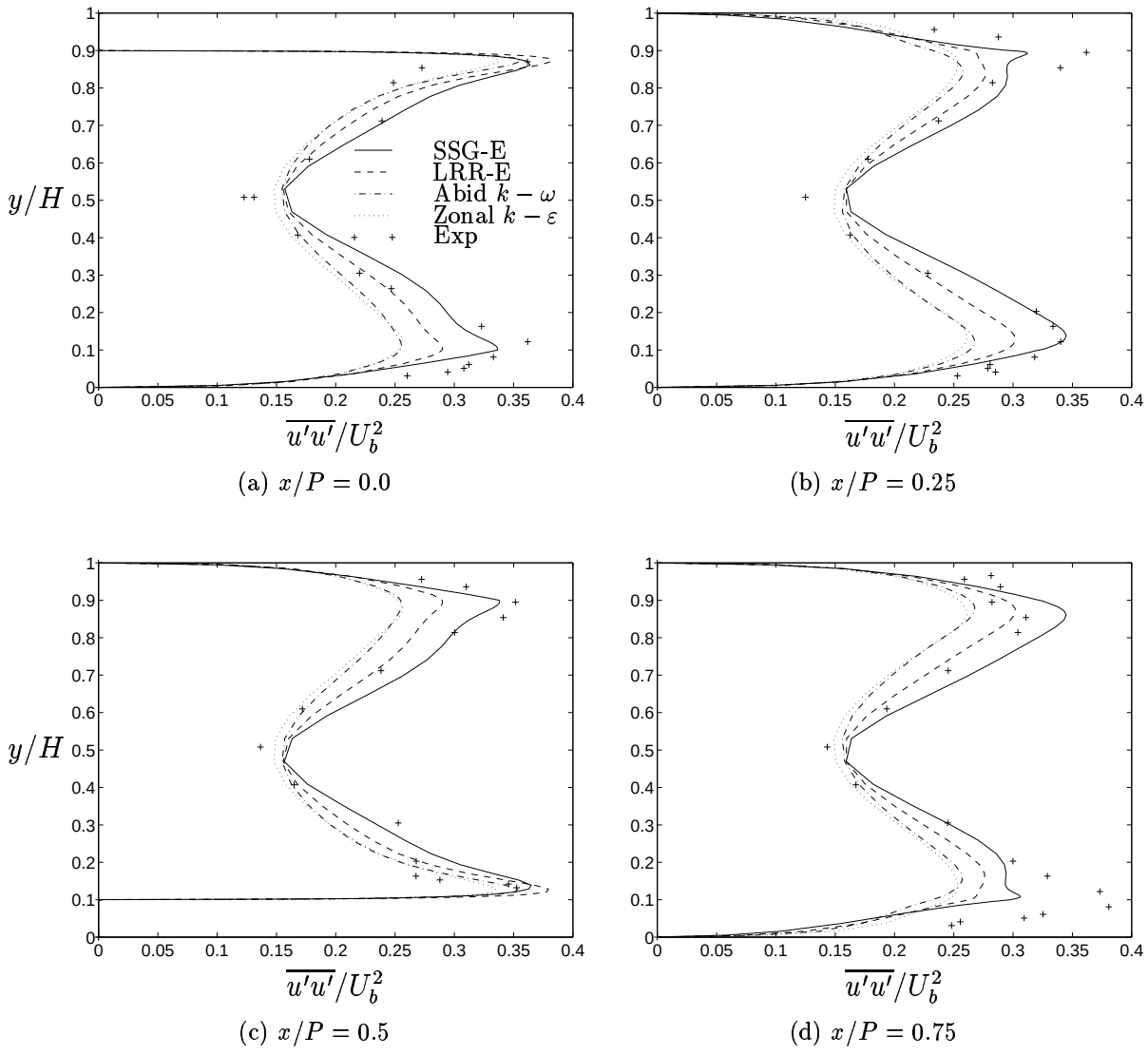

(a) $x/P = 0.0$ (b) $x/P = 0.25$

(c) $x/P = 0.5$ (d) $x/P = 0.75$

Figure 10.36: $\overline{u'u'}$-Normal Stress, UMIST 3D Stationary Ribbed Channel

experiment.

Fig. 10.34 depicts the normalized cross-stream velocity, V. In the two figures that show the V-velocity on top of the ribs, Fig. 10.34(a) and 10.34(c), the turbulence models return similar profiles, although they are not in total agreement with the experiment[38]. However, in the interval plots, Figs. 10.34(b) and 10.34(d), the difference among the models is notable. Discouragingly enough, the more advanced model, the larger the discrepancy!

The shear stresses, $\overline{u'v'}$, are depicted in Fig. 10.35. All models return a rather good result for the important shear stress, which is the main influential Reynolds stress on the mean flow.

Fig. 10.36 shows the streamwise normal stress, normalized with the squared bulk velocity. As can be seen in these figures, the EARSMs achieve the best agreement with the experimental data, which is not surprising since the two EVM do not predict any

[38]Note the scale of the abscissa and, even though the relative difference is large, the absolute is rather small.

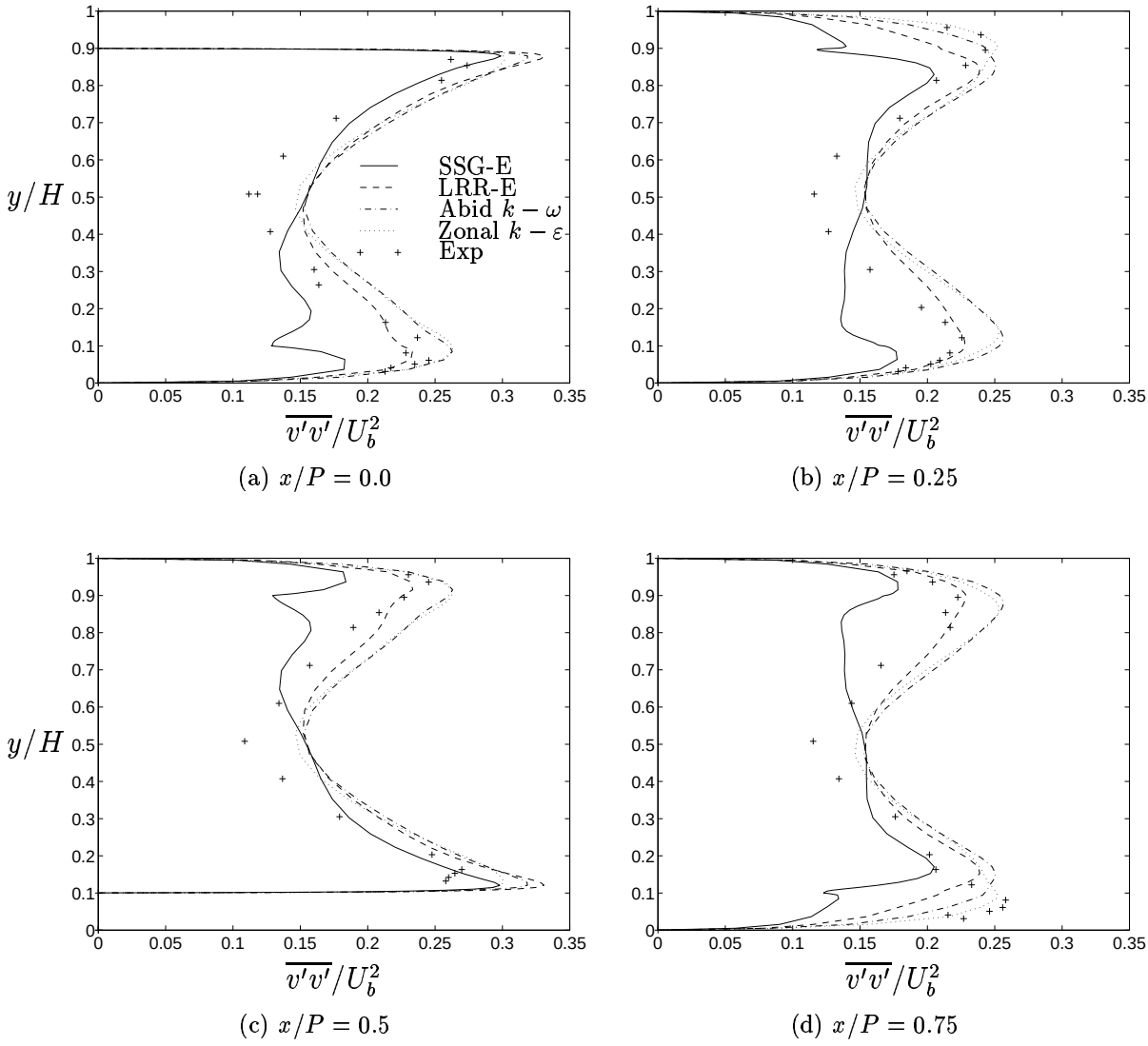

Figure 10.37: $\overline{v'v'}$-Normal Stress, UMIST 3D Stationary Ribbed Channel

anisotropy for either of the normal stresses.

The cross-stream normal stress, $\overline{v'v'}$, normalized with the bulk velocity, are seen in Fig. 10.37. The major discrepancy in these plots is the rather poor presentation of the SSG-EARSM, where the $\overline{v'v'}$ fluctuates violently behind the ribs. The reason for this behavior is most likely a mesh-dependent result. The mesh, which is orthogonal, is severely stretched at the rib top, and these stretched grid lines continue out in the flowfield, behind the rib. When the flow crosses these grid-lines transversely, as they do in the re-circulation zone behind the ribs, it results in a poor representation of the cross-stream normal stresses when predicting with the SSG-EARSM. This can be seen most clearly in Figs. 10.37(b) and 10.37(d), in the re-circulation zone behind the upper first rib and, the lower rib, respectively. In the first case the fluctuations are strongest at $y/H = 0.9$ and in the second case at $y/H = 0.1$, thus at the location of the rib tops. Further downstream, the fluctuations decrease, as does the cross-stream velocity in these areas, hence the conclusion regarding this phenomena. The reason why only the SSG pressure-strain model and not the LRR pressure-strain model behaves in this way

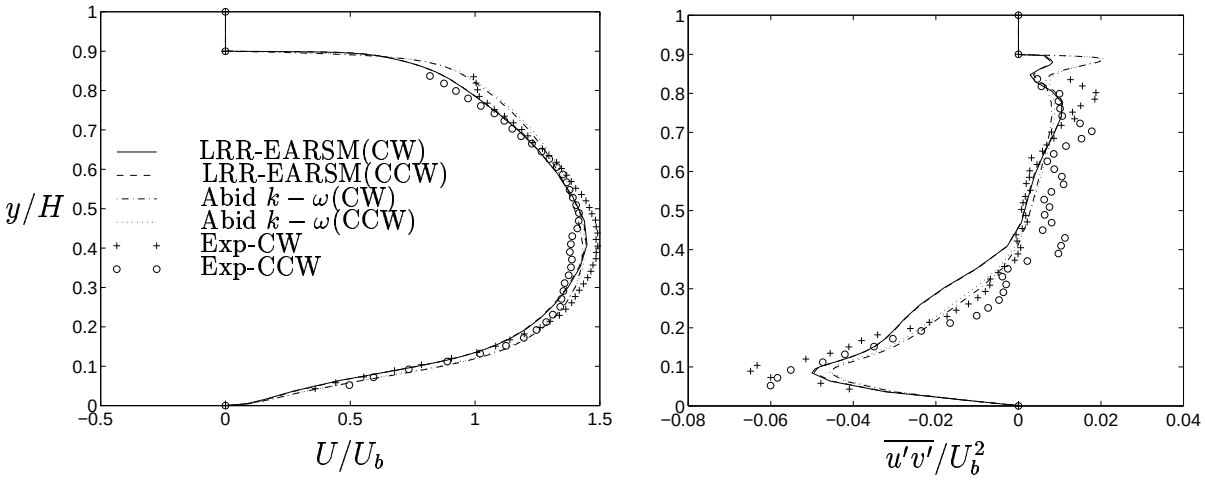

(a) U-Velocity

(b) $\overline{u'v'}$-Shear stress

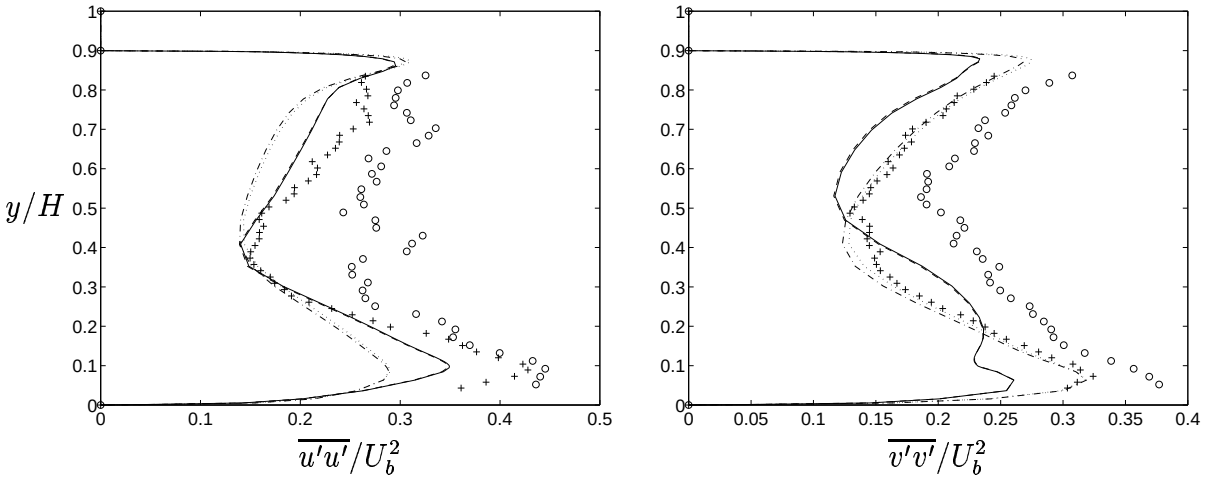

(c) $\overline{u'u'}$-Normal stress

(d) $\overline{v'v'}$-Normal stress

Figure 10.38: Velocity Profiles at $x/P = 0$, UMIST 3D Clock-wise and Counter-Clock-wise Rotating Ribbed Channel

is beyond the scope of this report. An attempt will be made to circumvent this problem by changing to a non-orthogonal grid with a more appropriate mesh disposition in the future.

Rotating: For the rotating UMIST case, there are two sets of measurement data: velocity data for either a positive rotation at $Ro_H = 0.2$ or a negative rotation of $Ro_H = -0.2$. The predictions were made in both the clock-wise and the counter-clock-wise directions of the channel, i.e. rotation around both the positive and negative z-axes. The rotationally induced forces shift the flowfield either to the upper wall (negative rotation) or the lower wall (positive rotation). Due to the staggered symmetrical arrangement of the channel, the predictions from a positive and negative calculation can easily be compared. Since the rotation shifts the flowfield, the prediction of either the positive or negative rotating channel the velocity profiles can be mirrored along the centerline, and then – because of the staggered arrangement of the ribs – shifted either upstream or downstream the

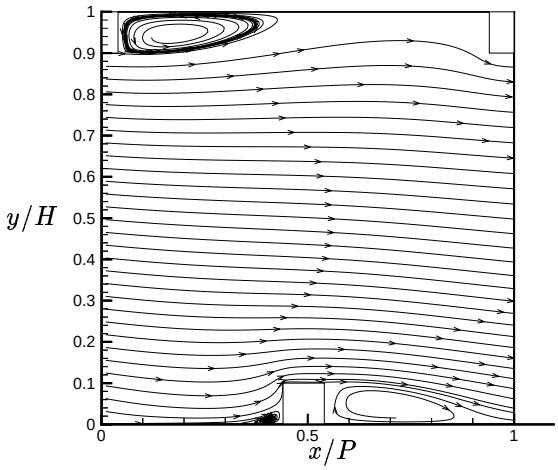

Figure 10.39: Streamlines, UMIST 3D Rotating Ribbed Channel

distance $x/P = 0.5$. Fig. 10.38 shows the predicted velocity profiles at $x/P = 0$ with the Abid *et al.* $k-\omega$ model and the EARSM with the LRR pressure strain, using either negative (CCW=counter clock-wise) or positive (CW=clock-wise) rotation. Included in the graphs are also the two measurements. As can be seen in the figures, the predicted velocity profiles from the two rotational directions overshadow each other for both models. However, depending on the rotational direction, the measurements deviate. This is not a surprising result – the opposite, would in fact be very surprising. All experiments include some errors and, for any two sets of measured data, there will always be some deviation. In addition to this, the experimental rig was not fully symmetric since the test section was part of a U-bend. The measured data were taken from an inter-rib region upstream the bend and, even though the bend is located further downstream, there is a possibility that there would be some transported effects from the bend to the test section. The differences in Fig. 10.38 can thus be seen as an error estimation for the the experimental data. This section was included simply to clarify any doubts regarding the implementation of the models for rotating structures. Some mistake during the implementation may have resulted in a model dependent on the direction of the angular velocity – especially the case for the EARSMs, where Ω_i is included in the description of the Reynolds stresses. The results shown are very satisfying, see also the predicted symmetry of the velocity field in the cross-stream plane in Fig. 10.25.

Although there are several measured velocity profiles available, there are unfortunately no measured Nusselt numbers, although the Nusselt number was nevertheless predicted, as can be seen in Fig. 10.40. In this picture, the comparison between the medium and fine mesh is shown, Figs 10.40(a) and 10.40(b). Fig. 10.40(c) together with 10.40(a) can be used to compare the difference between the upper wall – which in the case of positive rotation is the stable side – and the lower wall – the unstable side. The Abid *et al.* model is used to visualize the main difference between a rotating and a stationary case in the predicted Nusselt number, as seen in 10.40(d). The Nusselt number for the upper wall in the stationary case would simply be a half inter-rib shift of the lower wall and was excluded in the figure. The predicted Nusselt number for the Rotating case is abbreviated R and for the Stationary case as S in this latter figure.

Similar to the stationary case – evident by comparing the graphs for the medium mesh

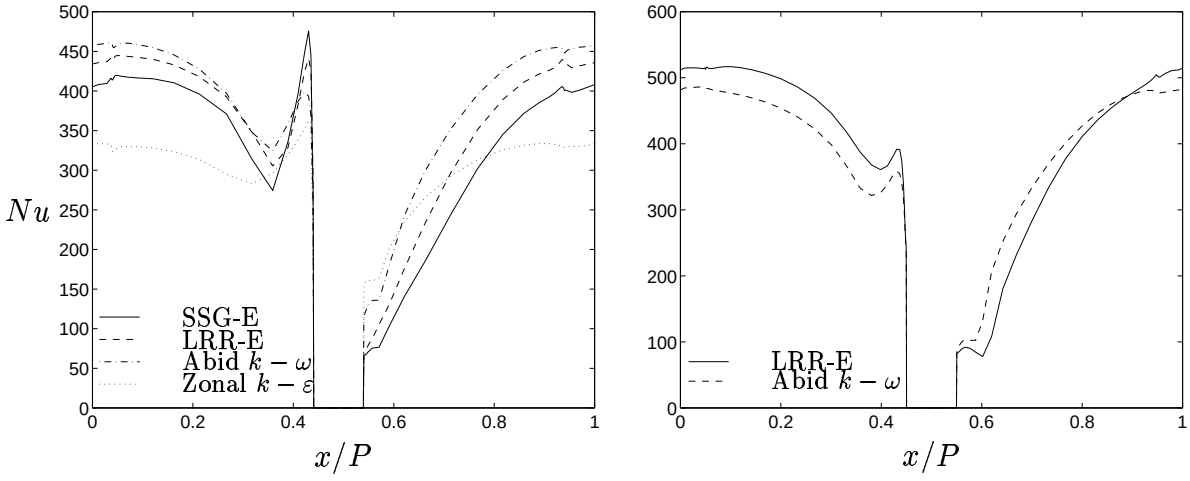

(a) Medium mesh, lower wall

(b) Fine mesh, lower wall

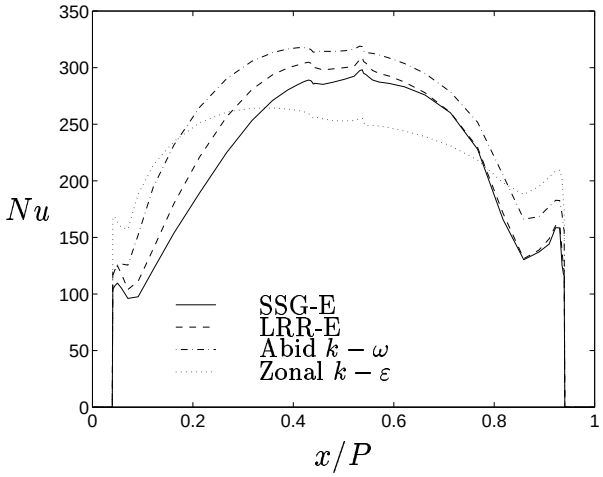

(c) Medium mesh, upper wall

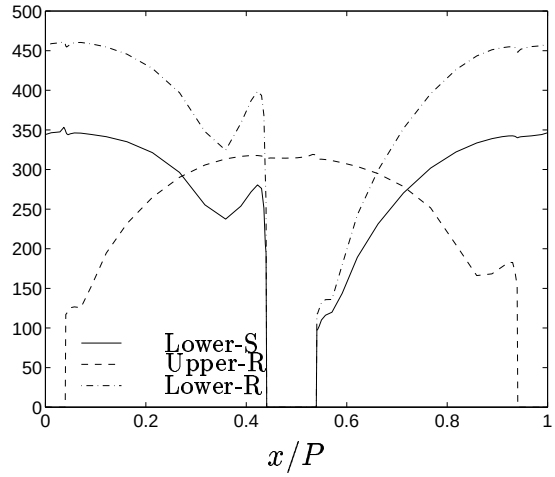

(d) Stationary-rotating Abid *et al.*

Figure 10.40: Nusselt Number, UMIST 3D Rotating Ribbed Channel

Fig. 10.40(a) with that for the fine mesh Fig. 10.40(b) – the medium mesh is not grid-independent. Whether or not the results can be trusted is hard to say – since there is no experimental material to compare with – but it is reasonable to believe an accuracy on the level of that found in the stationary case. Maybe the discrepancy might be somewhat higher for this rotating case, owing to the increased complexity of the flowfield. The main difference between the predicted Nusselt number for the rotating case as compared with the stationary case is the shift of the Nusselt number on the lower wall (increased) and upper wall (decreased), as can be seen in Fig. 10.40(d). The decrease on the upper wall is very slight, however, especially in middle part between the ribs, where the decrease is less than 10%. On the lower wall the increase is much more dominant and amounts to roughly 30%, which is surely a desired affect. From this it can be concluded that the rotation increases the general level of heat transfer in ribbed channels. The relative change of the heat transfer is of course associated with the increase in turbulent kinetic energy on the unstable side (lower) and a similar decrease in the turbulent kinetic energy on the stable side (upper). Through the heat transfer model used in this report, equation Eq. 8.5, the

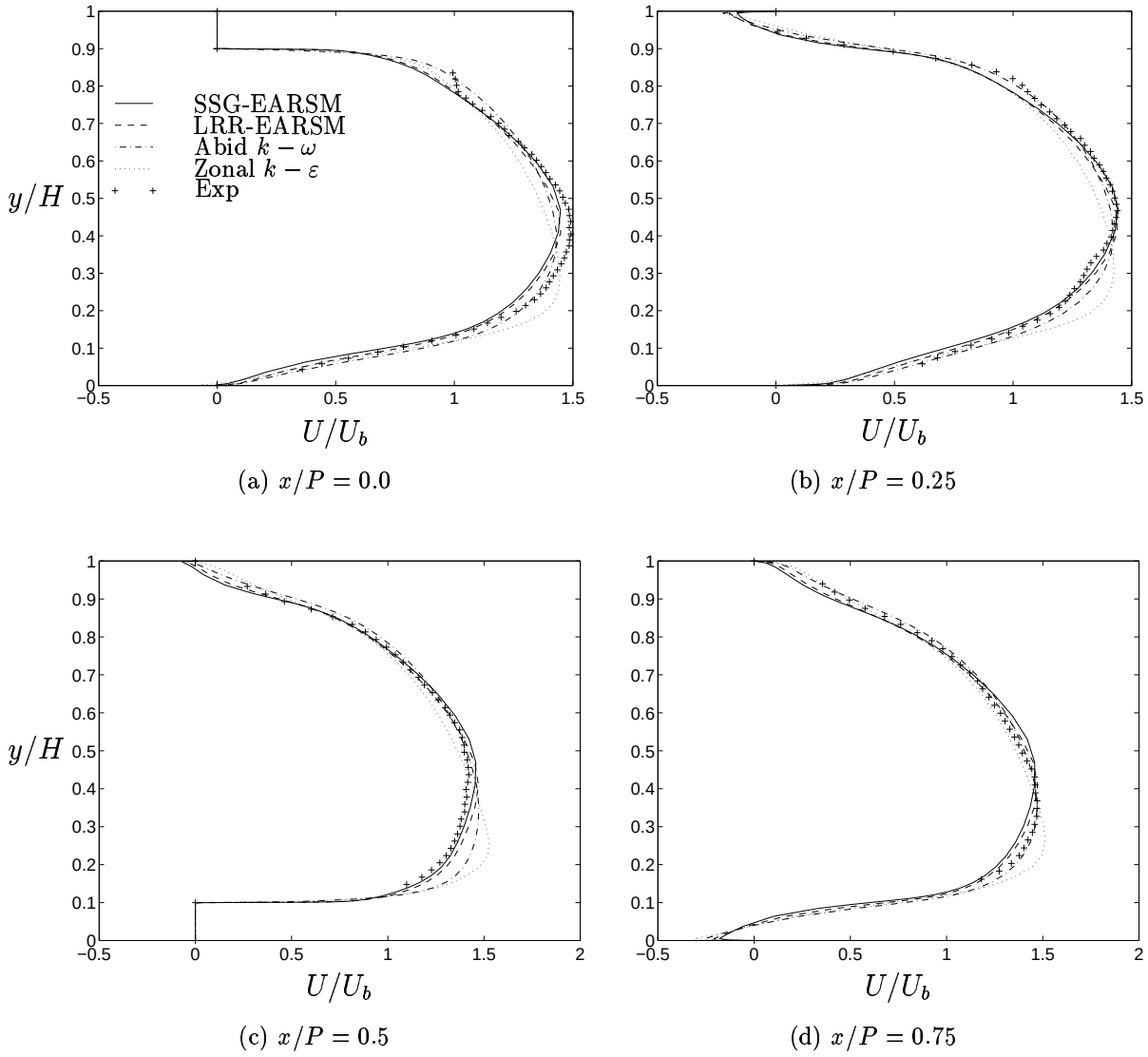

(a) $x/P = 0.0$ (b) $x/P = 0.25$

(c) $x/P = 0.5$ (d) $x/P = 0.75$

Figure 10.41: U-Velocity Profiles, UMIST 3D Rotating Ribbed Channel

eddy viscosity is directly related to the heat transfer, and thus an increase in turbulent kinetic energy would yield a higher Nusselt number and vice versa, see Fig. 10.40(d).

Apart from the change in the magnitude of the Nusselt number, the profiles are essentially the same, and the same conclusion as was made for the stationary case can be drawn regarding the performance in front of the rib and behind the rib. However, in this case, there are of course no experimental data to compare with, and hence no true conclusion can be made about the performance of the models.

Moving on to the velocity field, the streamlines for the Abid *et al.* turbulence model are shown in Fig. 10.39. Comparing the rotating case, Fig. 10.39, with the stationary case, Fig. 10.31, the latter has a repeatedly symmetric behavior, where the flowfields on the upper wall and the lower wall are essential the same, although shifted half a pitch. However, the rotating case loses this symmetry, and the rotationally induced Coriolis force $(-2\Omega_z u)$ shifts the velocity field downwards, as can be seen from the streamlines in Fig. 10.39. For this reason the re-circulation region behind the upper first rib is much larger than that behind the lower rib. See also later figures. As in the earlier cases, there is a

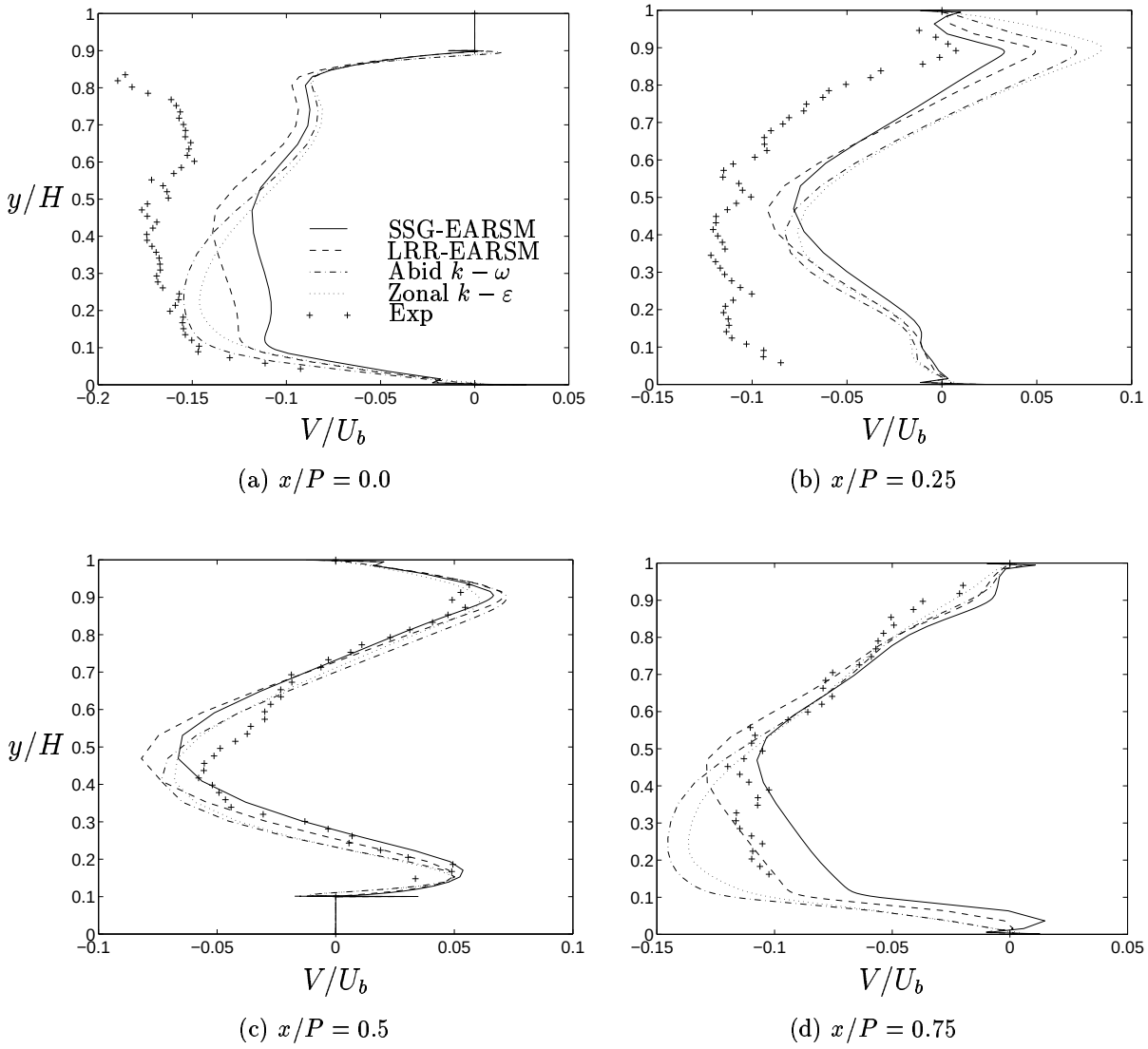

(a) $x/P = 0.0$ (b) $x/P = 0.25$

(c) $x/P = 0.5$ (d) $x/P = 0.75$

Figure 10.42: V-Velocity Profiles, UMIST 3D Rotating Ribbed Channel

re-circulation bubble in front of the ribs as well, although this is very much suppressed on the lower wall toward the wall, while it is increased on the upper wall.

The normalized streamwise velocity profiles are depicted in Fig. 10.41. The described differences in the re-attachment point behind the upper and lower rib is shown in this figure, although it is perhaps graphically more clear in the streamline plot of Fig. 10.39. Compare the differences in Fig. 10.41(b) and 10.41(c) where the flow is still flowing backwards along the upper wall five step heights downstream of the upper rib (see Fig. 10.41(c)), slightly dependent on the turbulence model, where the zonal model predicts almost zero back-flow. Along the lower wall, however, the flow is attached five step heights downstream of the rib (see Fig. 10.41(a)). In Fig. 10.41(d), it can be seen that, despite the downward shift of the flowfield, the flow still re-attaches along the upper wall and thus the pitch in this ribbed channel is sufficiently large to enable increased heat transfer – through higher turbulence levels – even in this rotating case. The smaller re-circulation bubble in front of the upper and lower ribs is evident in Figs 10.41(b) and 10.41(d), where the near-wall velocity is much higher 2.5 step heights upstream of the lower rib (former

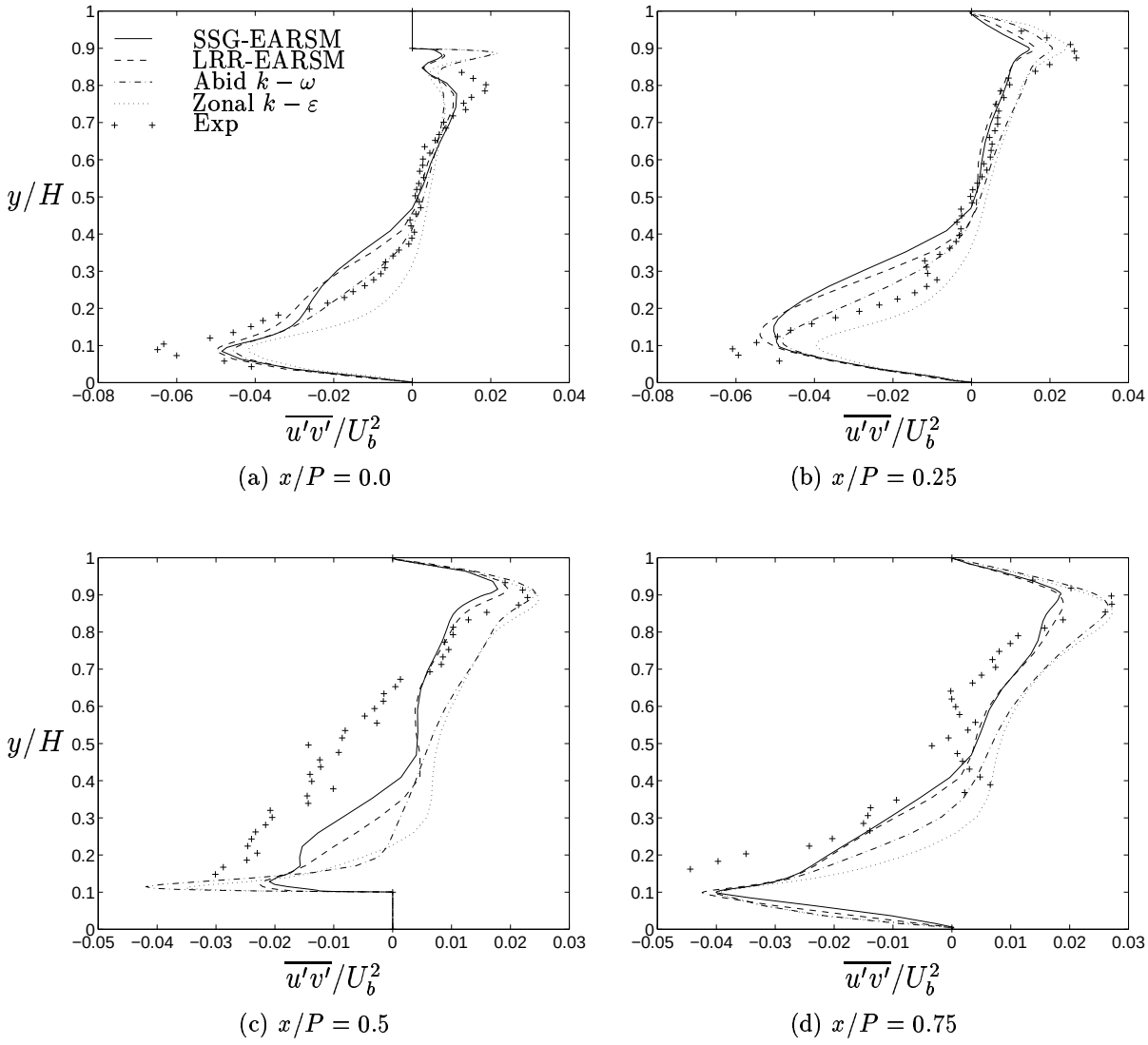

Figure 10.43: $\overline{u'v'}$-Shear Stress, UMIST 3D Rotating Ribbed Channel

figure) than at the same distance upstream of the upper rib (latter figure).

The largest deviation in the predictions is the relatively large over-prediction by the zonal model around $y/H = 0.2$ at all positions. This is associated with an under-prediction in other areas, since the mass flow is the same for all models. The other models however predict the downward shift of the velocity field accurately, with a maximum velocity around $y/H = 0.4$ slightly changing from one part of the channel to another owing, to the alternating blockage effect of the ribs. Despite the deviation of the zonal, the overall behavior of the models is satisfying. In the case of the $k-\omega$ based model, they all performed well none being able to be considered as the most prominent.

Fig. 10.42 depicts the cross-stream velocity, normalized with the bulk velocity. Generally, the EARSM models capture the measured profile more closely. The predictions deviate most at the two first figures, where all models under-predict the velocity profiles by up to 50%. Although the magnitude of the EARSMs is as badly as the EVMs, the profiles of the EARSMs are much better. This is also evident in Fig. 10.42(d). Comparing the two EARSMs, seems as though the LRR pressure-strain based model agrees better

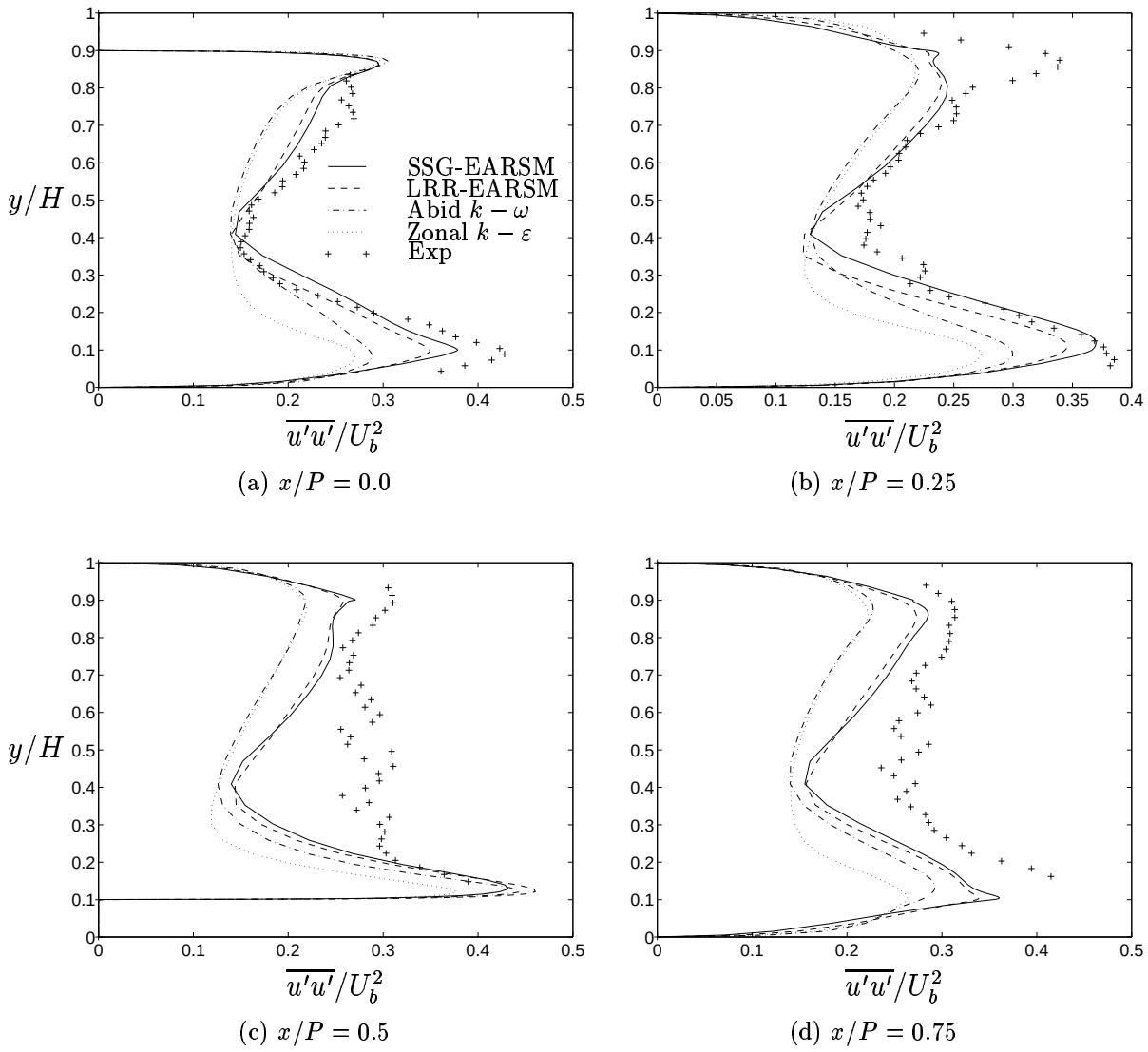

(a) $x/P = 0.0$ (b) $x/P = 0.25$

(c) $x/P = 0.5$ (d) $x/P = 0.75$

Figure 10.44: $\overline{u'u'}$-Normal Stress, UMIST 3D Rotating Ribbed Channel

than the SSG pressure-strain based model.

The normalized shear stress, $\overline{u'v'}$, is shown in Fig. 10.43. The agreement between the predictions and the measurements have decreased as compared with the stationary case, see Fig. 10.35, and there is also a larger difference among the turbulence models. The most notable problematic area is atop the lower rib, in Fig. 10.43(c), where none of the models capture either the correct profile or the correct level. Moving further up in the channel at this position, the experiment shows almost a linear relation of the shear stress between the lower and upper wall, which none of the models captures. The deviation is larger for the EVMs, although the profiles of the EARSMs act rather strangely – in the center part of the channel, the EARSMs predict zero shear stress, which is not found in the measurements.

Fig. 10.44 shows the wall normal stress, normalized with the square of the bulk velocity. As for the stationary case, the EARSMs return the best agreement, which reflects the increased physics involved in these models, enabling the models to deviate from the isotropic relation of the Boussinesq hypothesis.

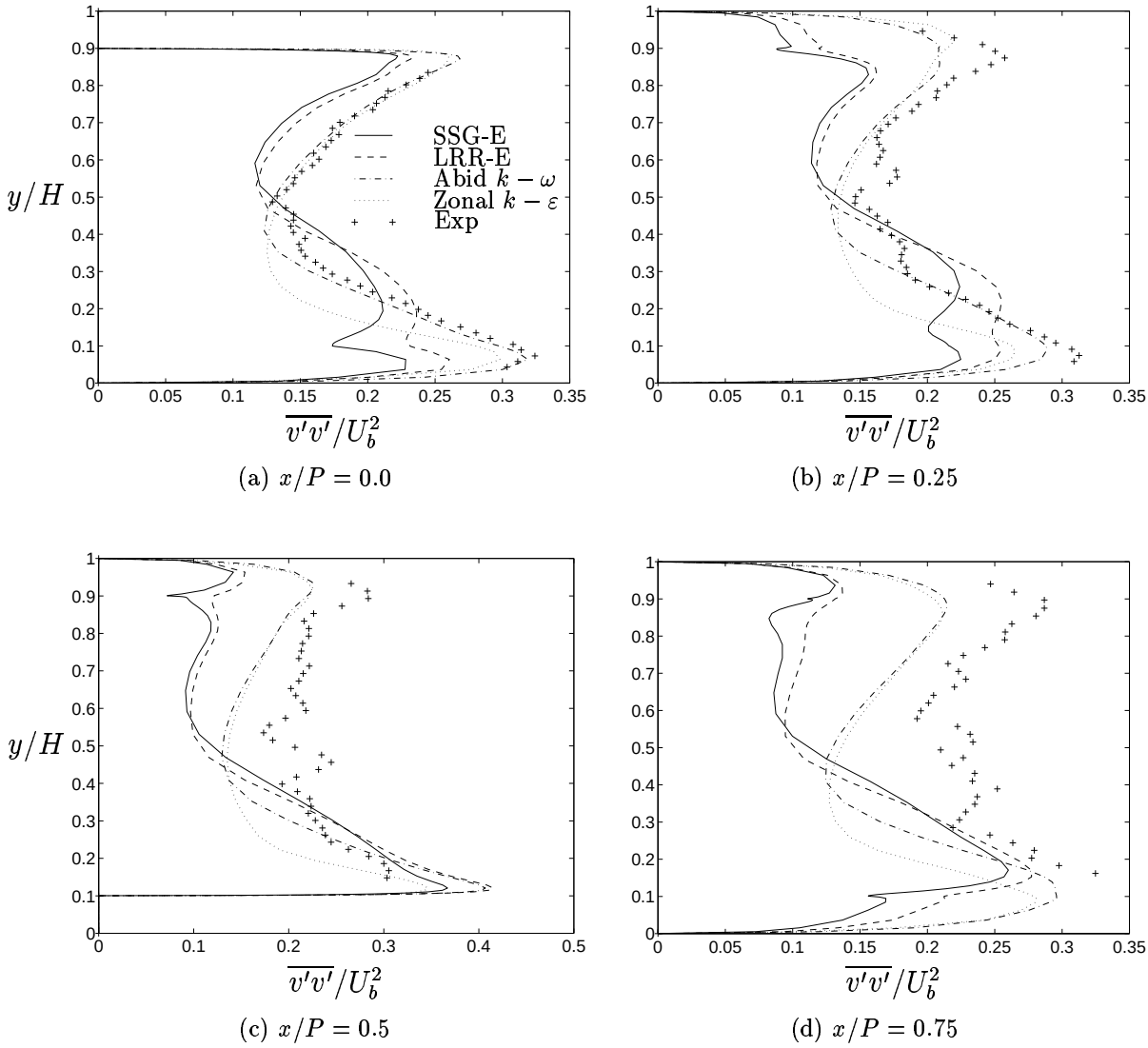

(a) $x/P = 0.0$ (b) $x/P = 0.25$

(c) $x/P = 0.5$ (d) $x/P = 0.75$

Figure 10.45: $\overline{v'v'}$-Normal Stress, UMIST 3D Rotating Ribbed Channel

The cross-stream normal stress is shown in Fig. 10.45. The same results as for the stationary case can be seen, with severe fluctuations in the predictions by the SSG-EARSM. However, in this rotating case, the LRR-EARSM also starts to behave badly, with fairly large dips around the area of grid stretches. The conclusions from this are the same as in the stationary case. The remedy may be a more evenly distributed mesh, and this will be tested in the future. Owing to this effect, the EVMs perform better in this case, although there is no reason to believe that the EARSMs would deviate very much from the profiles predicted by the EVMs, as can be seen in Fig. 10.45. The results atop the ribs support this conclusion, where the flowfield does not cross the mesh transversely, and hence the grid stretch does not effect the predictions of the EARSM in any negative way. As can be seen in the upper part of Fig. 10.45(a) and the lower part of Fig. 10.45(c) the predictions of the EARSMs and the EVMs are similar.

11 Conclusions

- In the case of rotating 2D channels, the standard two-equation models (such as $k-\varepsilon$ and $k-\omega$) do not alter the symmetrical velocity profiles found in a non-rotating case. The most prominent modification found was the Richardson number modification. The EARSM also improves the prediction in these cases. However, without the Richardson modification, the prediction by EARSM can not be considered adequate.

- The most promising turbulence model for the 2D ribbed channel was the $k-\omega$ model. The EARSM extension to this model can also be considered. However, if only mean parameters such as heat transfer and velocity profiles are included, the extra computational resources needed with the EARSM do not seem worthwhile. In the case of specific details of the Reynolds stresses (especially normal Reynolds stresses), the EARSMs improve the predictions.

- EARSMs are needed when the Reynolds stress induced secondary motions are important, such as in stationary 3D ducts – where nothing simpler than a second-moment closure model can be used. The EARSMs are however notably more unstable than the two equation models and, in the case of the 3D ducts, a transient prediction was necessary to be able to converge the solution. It should also be noted that, to reach convergence with the EARSM, an initial converged solution of the two-equation $k-\omega$ is normally used, and hence the computational time for an EARSM is at least twice that of an EVM.

- Reynolds dependency of the Nusselt number was found to be incorrect for all models, with a tendency to over-estimate the Nusselt number at high Reynolds numbers. In the case of the $k-\omega$ based models, the best agreement was achieved around $Re_H = 100\,000$.

- In the case of heat transfer prediction in ribbed channels, it was found that it is sufficient to fix only two to three nodes for the boundary condition for the ω equation in $k-\omega$ based models. This is in contrast with the severely more restricted criteria of Wilcox [58], which state that ω should be fixed for 7 to 10 nodes.

In summary, the $k-\omega$ model will be used in the future to predict heat transfer and flowfield inside turbine blades. An attempt will be made to correct the faulty Reynolds dependency for this model and some other versions of the low Reynolds number based $k-\omega$ will also be evaluated.

References

[1] R. Abid, J.H. Morrison, T.B. Gatski, and C.G. Speziale. Prediction of aerodynamic flows with a new explicit algebraic stress model. *AIAA Journal*, 34:2632–2635, 1996.

[2] R. Abid, C. Rumsey, and T. Gatski. Prediction of nonequilibrium turbulent flows with explicit algebraic stress models. *AIAA Journal*, 33:2026–2031, 1995.

[3] J.W. Baughn and X. Yan. Local heat transfer measurements in square ducts with transverse ribs. In *National Heat Transfer Conference*, 1992.

[4] T.V. Boussinesq. Mém. pres Acad. Sci.,3rd ed Paris XXIII p. 46, 1877.

[5] P. Bradshaw. The analogy between streamline curvature and buoyancy in turbulent shear flow. *J. Fluid Mechanics*, 36:177–191, 1969.

[6] J. Bredberg and L. Davidson. Prediction of flow and heat transfer in a stationary 2-D rib roughened passage using low-Re turbulent models. In *3:rd European Conference on Turbomachinery*, 1999.

[7] H.C. Chen and V.C. Patel. Near-wall turbulence models for complex flows including separation. *AIAA Journal*, 26:641–649, 1988.

[8] P.Y. Chou. On velocity correlations and the solutions of the equations of turbulent fluctuations. *Quart. of Appl. Math.*, 3:38–54, 1945.

[9] S. Dahlström. Implementation of an explicit algebraic Reynolds stress model to account for curvature effects. Report, Department of Thermo and Fluid Dynamics, Chalmers University of Technology, Gothenburg, 1997.

[10] B.J. Daly and F.H. Harlow. Transport equation in turbulence. *Phys. Fluids*, 13:2634–2649, 1970.

[11] L. Davidson and B. Farhanieh. CALC-BFC. Report 95/11, Department of Thermo and Fluid Dynamics, Chalmers University of Technology, Gothenburg, 1995.

[12] L.D. Drain and S. Martin. Two-component velocity measurements of turbulent flow in a ribbed-wall flow channel. In *Int. Conf. on Laser Anenometry - Advances and Application*, 1985.

[13] T.B. Gatski and C.G. Speziale. On explicit algebraic stress models for complex turbulent flows. *J. Fluid Mechanics*, 254:59–78, 1993.

[14] S.S. Girimaji. Fully-explicit and self-consistent algebraic Reynolds stress model. Report, ICASE Report No. 95-82, 1995.

[15] H.P. Greenspan. *The Theory of Rotating Fluids*. Cambridge University Press, Cambridge, 1968.

[16] J.C. Han. Heat transfer and friction characteristics in rectangular channels with rib turbulators. *J. Heat Transfer*, 110:321–328, 1988.

[17] K. Hanjalić and B.E. Launder. A Reynolds stress model of turbulence and its application to thin shear flows. *J. Fluid Mechanics*, 52:609–638, 1972.

[18] A. Hellsten. Some improvements in Menters $k-\omega$ SST turbulence model. 29th AIAA Fluid Dynamics Conference, AIAA 98-2554, 1998.

[19] J.O. Hinze. *Turbulence*. McGraw-Hill, Inc, 1975.

[20] J.H.G. Howard, S.V. Patankar, and R.M. Bordynuik. Flow prediction in rotating ducts using Coriolis modified turbulence models. *J. Fluids Engineering*, 102:456–461, 1980.

[21] A. Huser and S. Biringen. Direct numerical simulation of turbulent flow in a square duct. *J. Fluid Mechanics*, 257:65–95, 1993.

[22] H. Iacovides, D.C. Jackson, H. Ji, G. Kelemenis, and B.E. Launder. LDA study of flow development through an orthogonally rotating U-bend of strong curvature and rib-roughened walls. Paper no ASME-96-GT-476, Int. Gas-Turbine and Aero Congress, Birmingham, UK, 1996.

[23] H. Iacovides and B.E Launder. Computational fluid dynamics applied to internal gas-turbine blade cooling: a review. *Int. J. Heat and Fluid Flow*, 16:454–470, 1995.

[24] H. Iacovides and M. Raisee. Computation of flow and heat transfer in 2-D rib roughened passages. In K. Hanjalić and T.W.J. Peeters, editors, *2nd Int. Symp. on Turbulence Heat and Mass Transfer (Addendum)*, pages 21–30, Delft, 1997. Delft University Press.

[25] A.V. Johansson and S. Wallin. A new explicit algebraic Reynolds stress model. In *Advances in Turbulence VI*, 1996.

[26] J.P. Johnston, R.M. Halleen, and D.K. Lezius. Effects of spanwise rotation on the structure of two-dimensional fully developed turbulent channel flow. *J. Fluid Mechanics*, 56:533–557, 1972.

[27] W.P. Jones and B.E. Launder. The prediction of laminarization with a two-equation model of turbulence. *Int. J. Heat and Mass Transfer*, 15:301–314, 1972.

[28] W.M. Kays. Turbulent Prandtl number - where are we? *J. Heat Transfer*, 116:284–295, 1994.

[29] A. Khodak and C. Hirsch. Second order non-linear $k-\varepsilon$ models with explicit effect of curvature and rotation. In *Proceedings of the Third ECCO-MAS Computational Fluid Dynamics Conference*, 1996.

[30] A.N. Kolomogorov. Equations of turbulent motion in incompressible viscous fluids for very large Reynolds numbers. *Izvestia Academy of Sciences, USSR, Physics*, 6:56–58, 1942.

[31] R. Kristoffersen and H.I. Andersson. Direct simulation of low-Reynolds-number turbulent flow in a rotating channel. *J. Fluid Mechanics*, 256:163–197, 1993.

[32] B. Lakshminarayana. *Fluid Dynamics and Heat Transfer of Turbomachinery*. John Wiley & Sons, Inc, 1996.

[33] B.E. Launder, C.H. Priddin, and B.I. Sharma. The calculation of turbulent boundary layers on spinning and curved surfaces. *J. Fluids Engineering*, 99:231–239, 1977.

[34] B.E. Launder, G.J. Reece, and W. Rodi. Progress in the development of a Reynolds-stress turbulence closure. *J. Fluid Mechanics*, 68:537–566, 1975.

[35] B.E. Launder, D.P. Tselepidakis, and B.A. Younis. A second-moment closure study of rotating channel flow. *J. Fluid Mechanics*, 183:63–75, 1987.

[36] L.H. McAdams. *Heat Transmission.* McGraw-Hill, Inc, 1954.

[37] F.R. Menter. Influence of freestream values on $k - \omega$ turbulence model prediction. *AIAA Journal*, 30:1657–1659, 1992.

[38] F.R. Menter. Two-equation eddy-viscosity turbulence models for engineering applications. *AIAA Journal*, 32:1598–1605, 1994.

[39] G. J. E. Nicklin. Augmented heat transfer in a square channel with asymmetrical turbulence promotion. Final year project report, Department of Mechanical Engineering, UMIST, Manchester, 1998.

[40] J. Pallares and L. Davidson. Large eddy simulation of a rotating 3D duct. Private communication, Dept. of Thermo and Fluid Dynamics, Chalmers, 1999.

[41] R.L. Panton. *Incompressible flow.* John Wiley and Sons, Inc, 1995.

[42] S.V. Patankar, C.H. Liu, and E.M. Sparrow. Fully developed flow and heat transfer in ducts having streamwise-periodic variations of cross-sectional area. *J. Heat Transfer*, 99:180–186, 1977.

[43] S-H. Peng, L. Davidson, and S. Holmberg. A modified low-Reynolds-number $k - \omega$ model for recirculating flows. *J. Fluid Engineering*, 119:867–875, 1997.

[44] H.J. Perkins. The formation of streamwise vorticity in turbulent flow. *J. Fluid Mechanics*, 44:721–740, 1970.

[45] L. Prandtl. Über ein neues formelsystem für die ausgebildete turbulenz. *Akad. Wiss. Göttingen*, Math-Phys. Kl.:6–19, 1945.

[46] M. Raisee. Heat transfer models in rib roughened passages. Private communication Dept. of Mechanical Engineering, UMIST, 1998.

[47] P.D. Richardson. Heat and mass transfer in turbulent separated flows. *Chemical Eng. Sci,*, 18:149–155, 1963.

[48] W. Rodi. A new algebraic relation for calculating the Reynolds stresses. *Z. angew. Math. Mech.*, 56:T219–T221, 1976.

[49] J.C. Rotta. Statistische theori nichthomogener turbulenz. *Z. Phys.*, 129:547–572, 1951.

[50] H. Schlichting. *Boundary-Layer Theory.* McGraw-Hill, Inc, 1968.

[51] C.G. Speziale, S. Sarkar, and T.B. Gatski. Modeling the pressure-strain correlation of turbulence: an invariant dynamical systems approach. *J. Fluid Mechanics*, 227:245–472, 1991.

[52] H. Tennekes and J.L. Lumley. *A First Course in Turbulence*. Massachusetts Institute of Technology, Cambridge, 1972.

[53] D.J. Tritton. Stabilization and destabilization of turbulent shear flow in a rotating fluid. *J. Fluid Mechanics*, 241:503–523, 1992.

[54] S. Wallin and A.V. Johansson. A new explicit algebraic Reynolds stress model including an improved near-wall treatment. In *Flow Modeling and Turbulence measurements VI*, 1996.

[55] S. Wallin and A.V. Johansson. A new explicit algebraic Reynolds stress model for incompressible and compressible turbulent flow. *J. Fluid Mechanics (submitted)*, 1997.

[56] D.C. Wilcox. Reassessment of the scale-determining equation for advanced turbulence models. *AIAA Journal*, 26:1299–1310, 1988.

[57] D.C. Wilcox. Comparison of two-equation turbulence models for boundary layers with pressure gradient. *AIAA Journal*, 31:1414–1421, 1993.

[58] D.C. Wilcox. *Turbulence Modeling for CFD*. DCW Industries, Inc., 1993.

[59] D.C. Wilcox and T.L. Chambers. Streamline curvature effects on turbulent boundary layers. *AIAA Journal*, 15:574–580, 1977.

[60] M. Wolfshtein. The velocity and temperature distribution in one-dimensional flow with turbulence augmentation and pressure gradient. *Int. J. Heat and Mass Transfer*, 12:301–318, 1969.

Appendix A - Paper 1

Case 7.2: Two-dimensional flow and heat transfer over a smooth wall roughened with squared ribs

By

Jonas Bredberg and Lars Davidson

In proceedings from 7th ERCOFTAC/IAHR workshop on
refined turbulence modeling,
UMIST, Manchester, UK, May 28/29th, 1998

Appendix B - Paper 2

Prediction of flow and heat transfer in a stationary 2-D rib roughened passage using low-Re turbulent models

By

Jonas Bredberg and Lars Davidson

In proceedings of the 3:rd European Conference on Turbomachinery,
London, UK, March 2/5th, 1999